

AD-771 781

COOLDOWN AND MOTOR FIRING THERMO-  
STRUCTURAL ANALYSIS OF A 7.0 INCH  
DIAMETER PYROLYTIC GRAPHITE INSERT

Duane L. Baker, et al

Aerotherm Corporation

Prepared for:

Air Force Rocket Propulsion Laboratory

July 1973

DISTRIBUTED BY:

**NTIS**

National Technical Information Service  
U. S. DEPARTMENT OF COMMERCE  
5285 Port Royal Road, Springfield Va. 22151

## NOTICES

For the Commander: Charles R. Cooke, Chief, Solid Rocket Division

"When U.S. Government drawings, specifications, or other data are used for any purpose other than a definitely related government procurement operation, the Government thereby incurs no responsibility nor any obligation whatsoever, and the fact that the Government may have formulated, furnished, or in any way supplied the drawings, specifications or other data, is not to be regarded by implication or otherwise, or in any manner licensing the holder or any person or corporation, or conveying any rights or permission to manufacture use, or sell any patented invention that may in any way be related thereto."

RECEIVED BY		
BY	White Section <input checked="" type="checkbox"/>	
C. S.	Self Section <input type="checkbox"/>	
UNCL. DATED	<input type="checkbox"/>	
JUSTIFICATION		
BY		
DISTRIBUTION/AVAILABILITY CODES		
Dist.	AVAIL. AND/OR SPECIAL	
A		

AD 771 781

REPORT DOCUMENTATION PAGE		READ INSTRUCTIONS BEFORE COMPLETING FORM
1. REPORT NUMBER AFRPL-TR-73-72	2. GOVT ACCESSION NO.	3. RECIPIENT'S CATALOG NUMBER <b>UNCLASSIFIED</b>
4. TITLE (and Subtitle) COOLDOWN AND MOTOR FIRING THERMOSTRUCTURAL ANALYSIS OF A 7.0 INCH DIAMETER PYROLYTIC GRAPHITE INSERT		5. TYPE OF REPORT & PERIOD COVERED FINAL JANUARY 1971 - FEBRUARY 1972
7. AUTHOR(s) D. L. BAKER J. E. DAVIS W. S. BONNETT		6. PERFORMING ORG. REPORT NUMBER AEROTHERM REPT. NO. 73-74
9. PERFORMING ORGANIZATION NAME AND ADDRESS Aerotherm Division of Acurex Corporation 485 Clyde Avenue Mountain View, California		8. CONTRACT OR GRANT NUMBER(s) F04611-71-C-0023
11. CONTROLLING OFFICE NAME AND ADDRESS Air Force Rocket Propulsion Laboratory Edwards Air Force Base California 93523		10. PROGRAM ELEMENT, PROJECT, TASK AREA & WORK UNIT NUMBERS 6 2302 F PROGRAM ELEMENT PROJECT 3059 TASK 09
14. MONITORING AGENCY NAME & ADDRESS (if different from Controlling Office)		12. REPORT DATE JULY 1973
		13. NUMBER OF PAGES 147
		15. SECURITY CLASS. (of this report) <b>UNCLASSIFIED</b>
		15a. DECLASSIFICATION/DOWNGRADING SCHEDULE
16. DISTRIBUTION STATEMENT (of this Report)  Approved for public release - Distribution Unlimited		
17. DISTRIBUTION STATEMENT (of the abstract entered in Block 20, if different from Report)		
18. SUPPLEMENTARY NOTES  Reproduced by NATIONAL TECHNICAL INFORMATION SERVICE U S Department of Commerce Springfield VA 22151		
19. KEY WORDS (Continue on reverse side if necessary and identify by block number)		
Ablation Computer Codes      Pyrolytic Graphite      Thermal Properties Ablative Material      Rocket Nozzle Thermal Response      Mechanical Properties Heat Conduction Analyses      Surface Thermochemistry      Structural Analyses Heterogeneous Chemical Kinetics      Thermal Analysis      Elasticity Plasticity		
20. ABSTRACT (Continue on reverse side if necessary and identify by block number)		
<p>A detailed thermochemical and thermostructural analysis was performed on a seven inch diameter nozzle throat insert composed of a pyrolytic graphite coating on an AGSR substrate. The analysis considered an environment produced by a solid rocket propellant at a chamber pressure of 1000 psia for a duration of sixty seconds.</p> <p>The analysis showed the effect on the thermostructural predictions, including plasticity effects, of including grooves in the substrate, and of</p>		

(Continued from Block 20)

the sensitivity of the stresses on the backside constraint. In addition, the predictions were made for both the cooldown during the manufacturing process and for various times during the solid rocket motor firing.

An extensive literature search in preparation for performing the analysis indicated that the thermal and mechanical properties which are reported for pyrolytic graphite were not obtained from a consistent grade of the material. In addition, property data obtained after the analysis was performed showed a significant departure from the values used in the analysis. The effect of the new property data would be to increase the stresses predicted during the motor firing.

ia 1

UNCLASSIFIED



## FOREWORD

This report was prepared by the Aerotherm Division of Acurex Corporation under USAF Contract F04611-71-C-0023 and describes an extensive analytical study of the thermostructural analysis of a seven inch diameter pyrolytic graphite coated nozzle throat insert. This work was sponsored by the Air Force Rocket Propulsion Laboratory (AFRPL) with Capt. John Ellison and Mr. William Payne as the Project Officers.

Mr. Duane L. Baker was the Aerotherm Program Manager and principal investigator. Mr. Joe E. Davis and Mr. William S. Bonnett provided technical support in performing the thermostructural analyses.

## TABLE OF CONTENTS

<u>Section</u>	<u>Page</u>
1 INTRODUCTION	1-1
2 SUMMARY OF RESULTS AND CONCLUSIONS	2-1
3 NOZZLE CONFIGURATION	3-1
3.1 Nozzle Geometry	3-1
3.2 Material Properties	3-2
3.2.1 Material Thermal Properties	3-2
3.2.2 Structural Material Properties	3-3
4 THERMOCHEMICAL ANALYSIS	4-1
4.1 Analytical Techniques	4-1
4.2 Nozzle Environment	4-2
4.2.1 Motor Ballistics and Propellant	4-3
4.2.2 Boundary Layer Edge Environment	4-3
4.2.3 Wall Surface Energy Balance	4-3
4.3 Nozzle Wall Material Thermochemical Performance	4-7
5 STRUCTURAL ANALYSIS	5-1
5.1 Analytical Techniques	5-2
5.2 Geometric Representation of Rocket Nozzle Insert	5-4
5.2.1 Insert Without Stress Relieving Grooves	5-4
5.2.2 Insert with Stress Relieving Grooves	5-4
5.3 Modeling of the Insert Fabrication Process	5-5
5.4 Definition of Insert Boundary Conditions for Motor Firing	5-5
5.4.1 Inner Surface Boundary Condition	5-6
5.4.2 Outer Surface Boundary Condition	5-6
5.4.3 Upstream Surface Boundary Condition	5-6
5.4.4 Downstream Surface Boundary Condition	5-6
5.5 Definition of Insert Internal Loading Conditions	5-7
5.6 Predicted Structural Response	5-8
5.6.1 Fabrication Process	5-8
5.6.2 Motor Firing	5-10
5.6.3 Comparison of Present Technique with Superposition Principle	5-14
6 EVALUATION OF THERMOSTRUCTURAL RESULTS	6-1
REFERENCES	R-1

## LIST OF TABLES

<u>Table</u>	<u>Page</u>
3-1 Specific Heat as a Function of Temperature for Speer 8882, Speer 9139, and AGSR Bulk Graphites, for PG Coating and for MX 2600 Silica Cloth and MX 4926 Carbon Cloth Phenolics	3-11
3-2 Material Densities	3-12
3-3 Poisson's Ratio for Pyrolytic Graphite Coating and the AGSR Graphite Substrate	3-12
3-4 Estimated Grafoil Mechanical Properties	3-13
3-5 Room Temperature Yield Stresses for AGSR and PG	3-13
3-6 Strength Data for AGSR Graphite	3-14
4-1 Kinetically Controlled Reaction Rate Expressions Used for PG Layer and Speer Bulk Graphite Surface Thermochemistry Solutions <sup>a</sup>	4-10
4-2 Summary of Edge Conditions for Surface Thermochemistry Maps	4-11
5-1 Structural Analysis Plan	5-16
5-2 Summary of Structural Analyses Performed Using DOASIS Computer Program	5-17
5-3 Rocket Nozzle Insert Surface Boundary Conditions	5-18

## LIST OF FIGURES

<u>Figure</u>		<u>Page</u>
2-1	Plan for Thermostructural Analysis of 7 Inch Diameter PG Coated Insert	
3-1	Large PG Coated Nozzle	3-15
3-2	Definition of Nozzle Throat Assembly	3-16
3-3	PG Coated Throat Insert	3-17
3-4	Pyrolytic Graphite Thermal Conductivity	3-18
3-5	Thermal Conductivity for Speer 8882, Speer 9139, and AGSR Bulk Graphites	3-19
3-6	Combined Virgin and Char Thermal Conductivity for MX 2600 Silica Cloth Phenolic and MX 4926 Carbon Cloth Phenolic	3-20
3-7A	Definition of Grain Direction	3-21
3-7B	Coordinate System for Nozzle Throat Insert	3-22
3-8	Thermal Expansion Properties of Pyrolytic Coating and AGSR Graphite	3-23
3-9	Young's Modulus for Pyrolytic Graphite	3-24
3-10	Young's Modulus for AGSR Graphite	3-25
3-11	Bilinear Curve Fit of Stress Strain Curve	3-26
3-12	Measured Bi-Linear Curve Fit Uniaxial Stress-Strain Curves for AGSR Graphite.	3-27
3-13	Measured and Bi-Linear Curve Fit Uniaxial Stress-Strain Curves for AGSR Graphite	3-28
3-14	Measured and Bi-Lateral Curve Fit Uniaxial Stress-Strain Curves for AGSR Graphite	3-29
3-15	Course Grain AGSR Bi-Liner Moduli	3-30
3-16	Bi-linear Tensile Stress-Strain Curves for Pyrolytic Graphite, "a" Direct	3-31
3-17	Bi-linear Compressive Stress-Strain Curve for Pyrolytic Graphite, "a" Direction	3-32
3-18	Pyrolytic Graphite Bi-Linear Moduli	3-33

# LIST OF FIGURES (Continued)

<u>Figure</u>		<u>Page</u>
3-19	Comparison of "a" Direction Pyrolytic Graphite Thermal Expansion	3-34
3-20	Comparison of "c" Direction Pyrolytic Graphite Thermal Expansion	3-35
3-21	Comparison of "a" Direction Pyrolytic Graphite Young's Modulus	3-36
3-22	Comparison of Tensile Stress-Strain Data for AGSR Graphite	3-37
3-23	Compressive Properties versus Temperature for Pyrolytic Graphite In "a" Direction	3-38
3-24	Interlaminar Shear Strength vs. Temperature for Pyrolytic Graphite	3-39
4-1	Flow Chart for Aerothermodynamic Analysis	4-12
4-2	Assumed Chamber Pressure Histories	4-13
4-3	Flow Field Parameters for Subsonic and Transonic Non-Dimensional Flow Rates - Test Weight Nozzle	4-14
4-4	Flow Field Parameters for Supersonic Non-Dimensional Flow Rates - Test Weight Nozzle	4-15
4-5	Nondimensional Mass Flux as a Function of $D^*/D$	4-16
4-6	Non-Blowing Convective Heat Transfer Coefficients for 7 Inch Throat Diameter Submerged Nozzle	4-17
4-7	Kinetically Controlled Thermochemistry Maps for Bulk Graphite and PG Coating	4-18
4-8	Steady State Diffusion Controlled Surface Thermochemistry Map for MX 4926 Carbon Cloth Phenolic	4-19
4-9	Nozzle Insert Nodal Grid	4-20
4-10	Nozzle Assembly Nodal Grid	4-21
4-11	Surface Temperature Histories for PG Coating Using Nozzle Insert Nodal Grid	4-22
4-12	Surface Recession Rate Histories for PG Coating Using Nozzle Insert Nodal Grid.	4-23
4-13	Surface Recession Histories for PG Coating Using Nozzle Insert Nodal Grid	4-24
4-14	Surface Temperatures Histories for Bulk Graphite, PG Coating, and MX 4926 Carbon Cloth Phenolic Using Nozzle Assembly Nodal Grid	4-25

# LIST OF FIGURES (Continued)

<u>Figure</u>		<u>Page</u>
4-15	Surface Recession Rate Histories for Bulk Graphite, PG Coating, and MX 4926 Carbon Cloth Phenolic Using Nozzle Assembly Nodal Grid	4-26
4-16	Surface Recession Histories for Bulk Graphite, PG Coating, and MX 4926 Carbon Cloth Phenolic Using Nozzle Assembly Nodal Grid	4-27
4-17	Isotherm Temperature Profiles for Nozzle Insert Nodal Grid - $t = 1.5$ seconds	4-28
4-18	Isotherm Temperature Profiles for Nozzle Insert Nodal Grid - $t = 5.0$ seconds	4-29
4-19	Isotherm Temperature Profiles for Nozzle Insert Nodal Grid - $t = 10.0$	4-30
4-20	Isotherm Temperature Profiles for Nozzle Insert Nodal Grid - $t = 30.0$ seconds	4-31
4-21	Isotherm Temperature Profiles for Nozzle Insert Nodal Grid - $t = 60.0$	4-32
4-22	Isotherm Temperature Profiles for Nozzle Assembly Nodal Grid - $t = 1.5$ seconds	4-33
4-23	Isotherm Temperature Profiles for Nozzle Assembly Nodal Grid - $t = 5.0$ seconds	4-34
4-24	Isotherm Temperature Profiles for Nozzle Assembly Nodal Grid - $t = 10.0$ seconds	4-35
4-25	Isotherm Temperature Profiles for Nozzle Assembly Nodal Grid - $t = 30.0$ seconds	4-36
4-26	Representative Temperature Profiles Through the Pyrolytic Graphite Throat Insert	4-37
4-27	Isotherm Temperature Profiles for Nozzle Nodal Grid (Revised Pyrolytic Graphite Thermal Properties) - $t = 1.5$ seconds	4-38
4-28	Isotherm Temperature Profiles for Nozzle Insert Nodal Grid (Revised Pyrolytic Graphite Thermal Properties) - $t = 5.0$ seconds	4-39
4-29	Isotherm Temperature Profiles for Nozzle Insert Nodal Grid (Revised Pyrolytic Graphite Thermal Properties) - $t = 10.0$ seconds	4-40
4-30	Isotherm Temperature Profiles for Nozzle Insert Nodal Grid (Revised Pyrolytic Graphite Thermal Properties) - $t = 30.0$ seconds	4-41
4-31	Isotherm Temperature Profiles for Nozzle Insert Nodal Grid (Revised Pyrolytic Graphite Thermal Properties) - $t = 60.0$ seconds	4-42

# LIST OF FIGURES (Continued)

<u>Figure</u>		<u>Page</u>
5-1	Structural Grid for Non-Grooved Nozzle Insert	5-19
5-2	Structural Grid for Grooved Nozzle Insert	5-20
5-3	Rocket Nozzle Insert Fabrication Process Model	5-21
5-4	Rocket Nozzle Insert Boundary Conditions for Motor Firing	5-22
5-5	Interlaminar Shear Stress in Pyrolytic Graphite Coating Near AGSR Interface-Cooldown	5-23
5-6	Pyrolytic Graphite Hoop Stress at Nozzle Entrance for Grooved and Non-Grooved Substrates - 0 Backside Displacement	5-24
5-7	Pyrolytic Graphite Hoop Stress at Nozzle Exit for Grooved and Non-Grooved Substrates - 0 Backside Displacement	5-25
5-8	Comparison Cooldown Hoop Strains for the Grooved Substrate at the Entrance Plane Based on Elastic and Plastic DOASIS Analyses	5-26
5-9	Comparison of Cooldown Hoop Strains for the Grooved Substrate at the Nozzle Throat Plane Based on Elastic and Plastic DOASIS Analysis	5-27
5-10	Comparison of Cooldown Hoop Strains for the Grooved Substrate at the Exit Plane Based on Elastic and Plastic DOASIS Analysis	5-28
5-11	Regions of Failures in Non-Grooved Insert Due to Cooldown Elastic Analysis	5-29
5-12	Region of Failures in Grooved Insert Due to Cooldown Elastic Analysis	5-30
5-13	Comparison of Cooldown Hoop Stress for the Grooved Substrate at the Nozzle Throat Plane Based On Plastic and Elastic DOASIS Analysis	5-31
5-14	Regions of Failures in Grooved Insert Due to Cooldown Plastic Analysis	5-32
5-15	Deformations of AGSR Grooved Substrate During PG Coating Fabrication Cycle	5-33
5-16	Interlaminar Shear Stress in Pyrolytic Graphite Coating Near AGSR Interface - Motor Firing 0-Displacement Outer Surface	5-34
5-17	Hoop Stress in Pyrolytic Graphite Coating at the Nozzle Entrance Grooved Nozzle Insert	5-35
5-18	Hoop Stress in Pyrolytic Graphite Coating at the Nozzle Throat Grooved Nozzle Throat	5-36

# LIST OF FIGURES (Continued)

<u>Figure</u>		<u>Page</u>
5-19	Hoop Stress in Pyrolytic Graphite Coating at the Nozzle Exit Grooved Nozzle Insert	5-37
5-20	Radial Stress in Grooved Substrate at the Nozzle Throat Plane-0 Backside Displacement for Motor Firing Stresses	5-38
5-21	Hoop Stress in Grooved Substrate at the Nozzle Throat Plane-0 Backside Displacement for Motor Firing Stress	5-39
5-22	Hoop Stress in Grooved Substrate at the Nozzle Throat Plane for Various Backside Gaps, $t = 30$ secs	5-40
5-23	Effect of Gap on the Hoop Stress in the Pyrolytic Graphite Coating at the Nozzle Throat for the Grooved Substrate - $t = 30$ sec	5-41
5-24	Hoop Stress in Grooved Substrate at the Nozzle Throat Plane for Various Backside Constraints - 60 sec	5-42
5-25	Effect of Gap on the Hoop Stress in the Pyrolytic Graphite Coating at the Nozzle Throat for the Grooved Substrate	5-43
5-26	Evaluation of Error in Using Superposition Principle to Calculate Total Motor Firing Stresses in Pyrolytic Graphite Coating at the Nozzle Throat - $t = 1.5$ sec	5-44
6-1	Comparison of "a" Direction Pyrolytic Graphite Thermal Expansion	6-3
6-2	Comparison of "c" Direction Pyrolytic Graphite Thermal Expansion	6-4



# LIST OF SYMOBLS

$B_1, B_2$	constants in rate equations
$B'_C$	non-dimensional char removal parameter
$B'_G$	non-dimensional pyrolysis off gas parameter
$C$	constant defined in Eq. (4-6)
$D$	local diameter
$D^*$	nozzle throat diameter
$E_1, E_2$	activation energy
$E$	Young's modulus
$F$	view factor
$G$	shear modulus
$h$	enthalpy
$h_i$	enthalpy of specie "i" evaluated at the wall temperature
$H_R$	recovery enthalpy
$k$	thermal conductivity
$K_i$	equilibrium constant for "i" reaction
$Le$	Lewis number
$n$	percentage mass fraction of aluminum in the propellant
$P_i$	partial pressure of specie "i"
$\dot{q}$	heat flux
$\dot{q}_{cond}$	conduction heat flux
$\dot{q}_{inc rad}$	radiative heat flux incident to the surface

# LIST OF SYMBOLS (Continued)

$\dot{q}_{\text{rad in}}$	radiative heat flux into the material
$r$	radial coordinate
$R$	universal gas constant
$T$	temperature
$u$	velocity
$X$	moles of reaction per unit area per unit time
$z$	axial coordinate
$Z_i^*$	chemical potential of specie "i"
<u>Greek</u>	
$\alpha$	absorptivity on coefficient of thermal expansion
$\gamma$	shear strain
$\epsilon$	longitudinal strain
$\epsilon_s$	stream emissivity
$\epsilon_{\text{eff}}$	effective stream emissivity
$\theta$	circumferential coordinate
$\lambda$	boundary layer running length
$\nu$	Poisson's ratio
$\rho$	density
$\rho_{eU}^C H$	convective heat transfer coefficient
$\rho_{eU}^C M$	mass transfer coefficient
$\dot{m}$	mass flux at the nozzle throat
$\sigma$	stress
$\bar{\sigma}$	effective stress
$\phi$	angle between the material principal direction and the $v$ coordinate direction

## LIST OF SYMBOLS (Continued)

### subscripts

r	evaluated in radial direction
y	evaluated at yield condition
z	evaluated in axial direction
$\theta$	evaluated in circumferential direction
w	evaluated at the wall
s	local state condition

### superscripts

E	elastic component
P	plastic component
T	tension component
C	compression component

## SECTION 1

### INTRODUCTION

The design of components such as nozzles and reentry nosetips which are subjected to a high pressure and severe thermochemical environment requires a knowledge of the environment and the properties of the materials to be used. In addition, it requires a set of tools which can use this information to predict the thermochemical and thermostructural performance of the particular component. From a technical standpoint, the sophistication which is required in the design and, in particular, in the capabilities of the thermochemical and thermostructural design tools depends on the performance requirements of the component in relation to the capabilities of the available materials. If a simplified analysis shows large margins of safety, then a more sophisticated approach is not warranted. On the other hand, if small or negative margins of safety are predicted by the simplified approach, a more detailed investigation is warranted. Since sophisticated analyses are generally time consuming and expensive, the cost of the analysis must be weighed against the hardware and test costs. If these costs are cheap relative to the analysis costs and if the schedule allows a cut and try approach, then performing a sophisticated analysis often times can not be justified. However, if the reverse is true, then the more sophisticated approach to the design problem requires a detailed analysis.

One of the more difficult design problems which requires this more sophisticated approach is the use of pyrolytic graphite (PG) coatings in the throat region of either large diameter solid rocket nozzles which are intended to operate at moderate chamber pressures or small diameter nozzles which are intended to operate at high chamber pressures. Existing analytical tools in the form of computer programs have been validated for predicting the thermochemical performance of these inserts. These predictions include the definition of the surface recession rates and the in-depth temperature distributions. However, the prediction of the thermostructural response of the material is not as far advanced. Sophisticated analysis procedures are available in the form of computer programs, but for many materials or combinations of materials, these analysis procedures have not been validated. The problem of validating the analysis procedures is generally two-fold. The first part is the lack of meaningful experimental data for comparison and the second part is the lack of accurate high temperature mechanical properties.

Even with the above mentioned difficulties, a sophisticated analysis using the best available properties can provide insight into the thermostructural problem by identifying what effects are important. In this regard, a detailed thermostructural analysis was performed for a seven inch diameter pyrolytic graphite coating on an AGSR substrate. The items investigated included the effect of grooves in the substrate on the cooldown manufacturing stresses, the effect of performing an elastic-plastic analysis versus a linear elastic analysis, and the effect of backside constraint on the stress distribution in the insert during the motor firing. Another significant result was identifying the validity of presently available property data.

The significant results and conclusion obtained from the thermochemical and thermostructural analyses are summarized in Section 2. The material property data used in the analysis are presented and discussed in Section 3. The thermochemical results presented in Section 4 are followed by the thermostructural results in Section 5. The thermostructural results are evaluated in Section 6.

## SECTION 2

### SUMMARY OF RESULTS AND CONCLUSIONS

A thermostructural analysis was performed for a 7 inch diameter PG coated nozzle throat insert. The plan for this analysis is summarized in Figure 2-1. The conclusions which resulted from the analyses outlined in this figure are

- The effect of heat conduction through the upstream and downstream bulk graphites has a significant influence on the AGSR temperature and thus on the strain distribution in the insert but a negligible effect on the PG coating surface recession rate
- The lip on the upstream bulk graphite is marginal for the protection of the leading edge of the PG coating
- The inclusion of the PG surface recession rate in the structural analysis would be expected to have a significant influence on the late time predicted insert strain distributions
- The inclusion of grooves in the substrate has a beneficial effect on the PG interlaminar shear stress but a detrimental effect on the stresses in the AGSR
- The elastic-plastic analysis showed significant regions of plastic flow in the AGSR and predicted a larger region of failure in the AGSR than the liner elastic analysis
- Predicted modes of failure
  - Tensile failure of AGSR during cooldown
  - Compressive failure of AGSR at a motor burn time of 1.5 seconds
  - Compressive failure of AGSR and PG coating at a motor burn time of 60 seconds (5 mil displacement)
- For constant backside constraint, the motor firing stresses are a maximum just prior to motor burnout
- Superposition of elastic solutions is not valid for materials which have temperature dependent properties
- It is probable that the data banks used in the analysis for both the AGSR and the PG coating are inconsistent (i.e., not based on a consistent set of material samples)

In order to improve the thermostructural analysis procedure, effort must be initiated to

- Characterize the materials being used and understand the effect of varying the primary fabrication process variables
- Perform an integrated analysis and test program to obtain experimental data which can be used to validate the design approach.

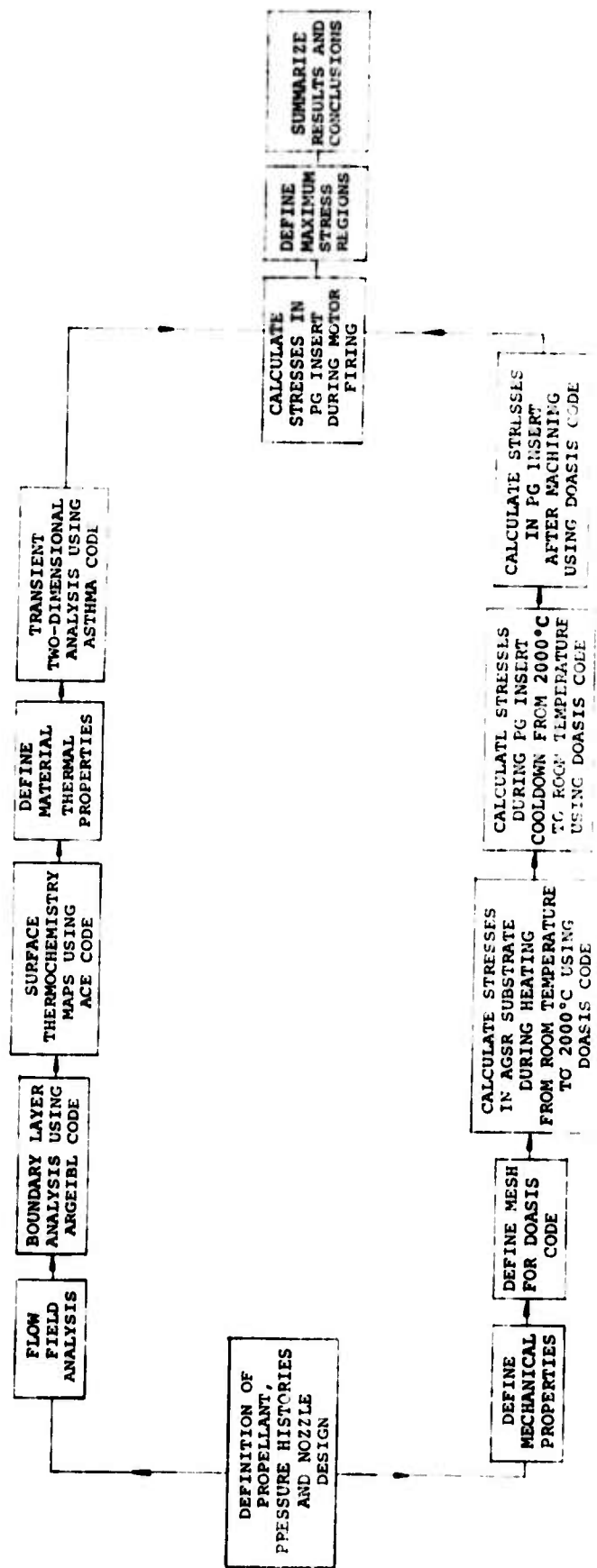


Figure 2-1. Plan for Thermostructural Analysis of 7 inch Diameter PG Coated Insert



## SECTION 3

### NOZZLE CONFIGURATION

The 7.0 inch diameter nozzle is a submerged nozzle composed of ablative materials which were selected based on both their thermal insulating and ablative characteristics. The nozzle geometry and materials are described briefly in Section 3.1, and the thermal and mechanical properties required to perform a thermostructural analysis are presented in Section 3.2.

#### 3.1 NOZZLE GEOMETRY

The geometry and materials for the 7-inch diameter submerged nozzle are shown in Figure 3-1. In this nozzle design, rubber insulation and MX 2600 silica phenolic are used on the backside of the nozzle where the gas velocities are relatively low. The nose cap is fabricated from MXCF 280 which is an elastomer modified carbon phenolic. Bulk graphite grades Speer 8882 and 9139 protect the upstream and downstream ends of the nozzle throat insert which is composed of a pyrolytic graphite coating (PG) on an AGSR substrate. The throat insert and the bulk graphites are insulated from the steel structural support by MX 2600 silica cloth phenolic. A throat exit ring of MX 4926 carbon cloth phenolic at a layup angle of  $90^\circ$  is located downstream of the Speer 9139 graphite.

The details of the nozzle throat assembly are shown in Figure 3-2 and the details of the PG coated nozzle throat insert are shown in Figure 3-3. The more important assembly details shown in Figure 3-2 are 1) the AGSR is bonded to both of the bulk graphites using Armstrong A-2 epoxy resin and using a bondline thickness from 5 to 20 mils, 2) the AGSR substrate is overwrapped with 3 layers of 2 mil thick teflon tape and 3) an 8 to 10 mil thick bondline of A-2 epoxy resin is used between the teflon overwrap and the MX 2600 silica phenolic insulation. In Figure 3-3, the details of the PG coated insert prior to final machining are shown. Grooves are located in the upstream and downstream ends of the AGSR substrate. The structural analyses presented in Section 5 investigate the effects of these grooves on the resulting stress distribution in the throat insert. As shown in Figure 3-3, the PG coating has a thickness of 60 to 65 mils upstream of the nozzle throat but this thickness decreases linearly to 45 to 50 mils between the throat and insert exit. Prior to installing the throat insert into the nozzle assembly, the final step in its fabrication is the cleanup machining on both ends of the insert.

Two items to note in Figure 3-1 relative to the flow field and boundary layer analyses are; 1) the boundary layer initiation is assumed to occur at the interface between the silica phenolic and the MXCE 280 carbon phenolic and 2) the step downstream of the bulk graphite throat insert entrance ring is modified by the dashed line shown in this figure. The effect of the boundary layer initiation location on the thermal and structural results is relatively minor. The second assumption is justifiable based on the fact that the objective of the analysis is to obtain an overall assessment of the thermal and structural capabilities of the nozzle throat insert and is not an evaluation of a particular local perturbation. This local perturbation would be of primary significance in predicting the local surface recession rate and not in predicting the in-depth transient temperatures.

### 3.2 MATERIAL PROPERTIES

The material properties required to perform both the chemical and structural analyses are presented in this section. A thermal analysis was performed for both the nozzle throat assembly (Figure 3-2) and the nozzle throat insert (Figure 3-3). Therefore, thermal properties are required for the graphitic and ablative materials shown in Figure 3-2. These properties are presented in Section 3.2.1. The structural analysis was performed only for the nozzle throat insert, and thus, mechanical and thermal expansion properties are required only for the PG coating and the AGSR substrate. These properties are presented in Section 3.2.2. One of the parameters studied in the structural analysis was the constraint on the backside of the AGSR. In this study, a thin cylindrical shell of multi-layered grafoil was considered in order to obtain a flexible backside constraint. The properties used for this material are also presented in Section 3.2.2.

#### 3.2.1 Material Thermal Properties

The materials considered in the two dimensional heat conduction thermal analysis are the Speer 8882, Speer 9139, and AGSR bulk graphites, the PG coating, and the MX 2600 silica and MX 4926 carbon cloth phenolics. The properties required in the thermal analysis are

- thermal conductivity in both directions as a function of temperature
- specific heat as a function of temperature
- density

The thermal conductivity of the PG coating as a function of temperature is shown in Figure 3-4 for both the "a" and "c" directions. Two different curves are shown in this figure for the "c" direction and the reference for each set

of data is noted. The difference between the two sets of "c" direction thermal conductivities is significant, and the effect of this difference on the predicted in-depth transient temperatures is presented in Section 4. In the text that follows, the curve designated by the solid line in Figure 3-4 is referred to as the revised "c" direction thermal conductivity, and the dashed line is referred to as the original "c" direction thermal conductivity. The thermal conductivity values of the bulk graphites and charring ablating phenolics are presented in Figures 3-5 and 3-6, respectively. The values for the Speer graphites were obtained from Reference 3 and the nominal values for the AGSR were obtained from Reference 4. For the majority of the temperature range, the with and across grain values of the AGSR thermal conductivity were obtained by applying a  $\pm 20$  percent variation to the nominal values. For the cloth phenolics, the curves in Figure 3-6 were obtained from Reference 5 and represent a combination of the virgin and char thermal conductivities.

The values used for the specific heat of these materials are presented in Table 3-1. The specific heat values for the PG coating were obtained from Reference 2; the specific heats of the AGSR and Speer graphites were assumed to be the same as ATJ; and the specific heats for cloth phenolics were obtained from Reference 5. For these latter materials, the values for specific heat include the effect of the energy absorbed by the in-depth material degradation. The reason for including this effect in the thermal properties is that the two dimensional heat conduction code used in the thermal analysis does not have the option of in-depth material degradation. As a result, effective thermal properties which include the effect of material degradation must be determined from the virgin and char thermal properties of the ablative materials. The densities for all the materials considered in the thermal analysis are presented in Table 3-2.

### 3.2.2 Structural Material Properties

The structural analyses to be described in Section 5 for the nozzle insert composed of the PG coating and the AGSR substrate were performed considering both elastic and plastic effects. The mechanical properties used in the elastic structural analysis are presented in Section 3.2.2.1, and the additional mechanical properties required for the plastic structural analysis are presented in Section 3.2.2.2. Some guidelines concerning the accuracy of the material properties used in the structural analysis are presented in Section 3.2.2.3, and information concerning the strength of the PG and AGSR is presented in Section 3.2.2.4.

### 3.2.2.1 Elastic Structural Analysis Properties

For an axisymmetric elastic structural analysis, the constitutive equations in cylindrical coordinates for orthotropic materials are

$$\begin{Bmatrix} \epsilon_r \\ \epsilon_z \\ \epsilon_\theta \\ \gamma_{rz} \end{Bmatrix} = \begin{bmatrix} \frac{1}{E_r} & \frac{-\nu_{zr}}{E_z} & \frac{-\nu_{\theta r}}{E_\theta} & . \\ \frac{-\nu_{rz}}{E_r} & \frac{1}{E_z} & \frac{-\nu_{\theta z}}{E_\theta} & . \\ \frac{-\nu_{r\theta}}{E_r} & \frac{-\nu_{z\theta}}{E_z} & \frac{1}{E_\theta} & . \\ . & . & . & G_{rz} \end{bmatrix} \begin{Bmatrix} \sigma_r \\ \sigma_z \\ \sigma_\theta \\ \tau_{rz} \end{Bmatrix} + \begin{Bmatrix} \alpha_r \\ \alpha_z \\ \alpha_\theta \\ . \end{Bmatrix} (T - T_{ref}) \quad (3-1)$$

where  $E_r, E_z, E_\theta$  - Young's modulus

$G_{rz}$  - shear modulus

$\nu_{zr}, \nu_{rz}, \nu_{\theta r}, \nu_{r\theta}, \nu_{z\theta}$  - Poisson's coefficients

$\alpha_r, \alpha_z, \alpha_\theta$  - coefficients of linear thermal expansion

If in addition to being orthotropic, the materials have a plane of isotropy then they are referred to as transversely isotropic and the following relations exist between the constants in the stress-strain constitutive relations described by Eq (3-1).

$$\begin{aligned} E_\theta &= E_r \text{ for } r, \theta \text{ plane of isotropy} & \frac{\nu_{zr}}{E_z} &= \frac{\nu_{rz}}{E_r} \\ \text{or } E_\theta &= E_z \text{ for } z, \theta \text{ plane of isotropy} & \frac{\nu_{\theta r}}{E_\theta} &= \frac{\nu_{r\theta}}{E_r} \\ \text{or } E_r &= E_z \text{ for } r, z \text{ plane of isotropy} & \frac{\nu_{\theta z}}{E_\theta} &= \frac{\nu_{z\theta}}{E_z} \end{aligned} \quad (3-2)$$

Equations (3-1) and (3-2) have five independent stress-strain constants and 3 independent coefficients of thermal expansion, and these constants are required as input to the structural analysis. For a cylindrical tube of AGSR coated with PG, (refer Figure 3-7a), the plane of isotropy for the PG is the  $z, \theta$  plane and the plane of isotropy for the AGSR substrate is the  $r, \theta$  plane. For the PG coating, the  $z$  and  $\theta$  directions are the with grain directions (often referred to as the "a" direction) and the  $r$  direction is the across grain direction (often referred to as the "c" direction). For the AGSR, the  $r$  and  $\theta$  directions are the across grain directions and the  $z$  direction is the with grain direction. For the billet size required for the 7 inch diameter insert, this material is generally considered isotropic. For the actual nozzle insert, the coordinate axes used in the analysis is shown in Figure 3-7b. The plane of isotropy for the AGSR in this configuration is the same as described above. However, the plane of isotropy for the PG coating is the  $2-\theta$  plane which is a curved surface. The 1-direction in this coordinate system corresponds to the "c" direction of the PG coating and the 2 and  $\theta$  directions correspond to the "a" direction of the coating. In using the DOASIS computer program, the "a" and "c" direction material properties are input, and the program rotates them to the  $r$  and  $z$  directions

The AGSR and PG coating thermal expansion data used in the analysis are presented in Figure 3-8 as a function of temperature for both the with and across grain directions. The PG coating data were obtained from Reference 1. However, Reference 1 obtained the data from Reference 6 and it appears as though Reference 6 obtained it from Reference 7. The AGSR data were also obtained from Reference 1. These data for the AGSR were determined based on known room temperature values and on assuming that the temperature dependency was the same as for similar grades of graphites.

Young's moduli as a function of temperature for the PG are shown in Figure 3-9 for both the with and across grain directions. In addition, this figure shows the dependence of the "a" direction Young's modulus on the direction of the applied stress. The Young's modulus values in the "c" direction and the tension Young's modulus values in the "a" direction were the same as used in Reference 1 and were obtained from Reference 8. The temperature dependency of the "c" direction modulus was based on extrapolating the measured room temperature value by the ratio  $(E_c/E_a)$ . The "a" direction compression modulus values were obtained from Reference 9 with the original source of the data being Reference 10.

Three sets of data for the Young's moduli of AGSR graphite are shown in Figure 3-10. The set shown by the solid lines were obtained from Reference 1 and reflect considerable material anisotropy. The temperature variation of this data was obtained by extrapolating room temperature values based on measurements on similar grades of graphite. The data points shown in Figure 3-10 reflect uniaxial tensile measurements on cross grain AGSR samples taken from 24 inch diameter billets. Room temperature data presented in Reference 12 indicate that the AGSR is essentially isotropic for billets in the 14 to 35 inch diameter range. The data shown in Figure 3-10 do not reflect any variation of the Young's modulus with temperature for temperatures less than 4000°F. The mechanical properties presented in Reference 11 shows this same trend with temperature. The values used in the structural analysis were obtained from the third curve presented in Figure 3-10 and were assumed to be independent of grain direction. This curve was obtained from the values represented by the dashed curve through the data by multiplying these values by a factor of 0.8. The purpose of this factor was to account for the specimens being in an unannealed state whereas the substrate used in the nozzle was annealed.

The room temperature Poisson's ratios used in the analysis for the PG and AGSR are listed in Table 3-3, and because no data were available showing the functional relationship with temperature, they were assumed to be independent of temperature. The values for the PG were obtained from Reference 10 and those for the AGSR were obtained from Reference 12.

The remaining constants to be defined are the shear modulus (or modulus of rigidity) for both the PG coating and the AGSR. Since no data were available, the shear modulus for the AGSR was evaluated from the relationship

$$G = \frac{E}{2(1+\nu)} \quad (3-2)$$

For the PG coating, a value of  $0.2 \times 10^6$  psi was obtained from Reference 13. This value is in general agreement with the one ( $0.1 \times 10^6$  psi) reported in Reference 9 which was obtained by assuming that the difference between  $E$  in pure tension and  $E$  in beam deflection is due to a shear component in the beam deflection method.

In one of the structural analyses, a thin piece of multi-layered grafoil

was placed on the outside surface of the AGSR substrate. The properties assumed for this material are presented in Table 3-4.

### 3.2.2.2 Plastic Structural Analysis Properties

The plasticity model used in the DOASIS structural analysis code is based on the total strain or deformation theory and more information concerning the theory and its implementation in the DOASIS code can be found in References 14 through 16. For this theory, the total strains are defined as

$$\epsilon = \epsilon^E + \epsilon^P \quad (3-3)$$

where

$\epsilon^E$  - total elastic strain

$\epsilon^P$  - total plastic strain

The total elastic strains are defined by the set of constitutive equations given in Eq (3-1). The equations defining the total plastic strains can be represented in matrix form by the relationship

$$\epsilon^P = \frac{\bar{\epsilon}^P}{\bar{\sigma}} [\alpha] \sigma \quad (3-4)$$

where

$\bar{\epsilon}^P$  - effective plastic strain

$\bar{\sigma}$  - effective stress

$[\alpha]$  - matrix of anisotropic parameters

$\sigma$  - stress vector

For a stress-strain curve which can be approximated by a bilinear fit such as shown in Figure 3-11, the mechanical properties in addition to those presented in Section 3.2.2 which are required to solve Eq 3-4 for the total plastic strains are the tangent moduli and yield stresses of the material. As shown in Figure 3-11, the tangent modulus is determined by the strain hardening portion of the stress strain curve and the yield stress is determined by the intersection of the linear segments of the bilinear approximation of the stress strain curve. A least squares curve fit procedure is used to obtain this bilinear approximation.

Since the plastic structural analysis is performed for only the cool down of the insert following the PG coating operation, the tangent moduli and the yield stresses are required only at room temperature. However, where



experimental stress-strain data are available at other temperatures, these data are used to define the variation of the tangent moduli with temperature.

For the AGSR graphite, the uniaxial stress-strain curves presented in Reference 11 were used as the basis for defining the bilinear curve. These data and the corresponding bilinear fits are presented in Figures 3-12, 3-13, and 3-14 for specimen temperatures corresponding to 70, 2000, and 3425°F. The Young's and tangent moduli obtained from these curve fits are summarized in Figure 3-15. No experimental data were found for defining the shear tangent modulus so this value was estimated based on the ratio of the Young's and tangent moduli.

For the PG, the uniaxial stress strain curves presented in Reference 6 were used as the basis for defining the required mechanical properties. These curves and their corresponding bilinear curve fits for the "a" direction and for various specimen temperatures are presented in Figure 3-16 for tensile stresses and in Figure 3-17 for compressive stresses. The Young's and tangent moduli obtained from these bilinear curve fits are presented in Figure 3-18. For the room temperature values of the "c" direction and shear tangent moduli, no experimental data were available so these values of the tangent moduli were obtained using the ratio of the "a" direction tensile Young's and tangent moduli.

The room temperature yield stresses used in the analysis for the AGSR and PG coating are summarized in Table 3-5. As mentioned previously, these yield stresses correspond to the intersection of the linear segments in the bilinear stress-strain curve and thus can be influenced by the method used to perform the curve fitting.

#### 3.2.2.3 Evaluation of Material Properties

It is obvious from Sections 3.2.1, 3.2.2.1, and 3.2.2.2 that the material properties for both the AGSR graphite and the PG were not obtained from a single source but rather were gathered from a number of sources. Because of this, it is pertinent to review some of the data presented in these sections and to make an evaluation of the variations that might be expected in the material properties. These variations are presented first for PG and then for the AGSR.

A review of the fabrication process of the PG coating revealed that several variables (deposition temperature and pressure, gas flow rate, type of substrate surface finish, coating thickness, deposition of soot particles, etc) are significant in determining the material properties of the end product.



However, the variation in material properties presented here is restricted primarily to the differences represented by substrate and continuously nucleated types of PG. Comparison of existing data for these two types of PG are shown in Figure 3-19 for the "a" direction thermal expansion curves and in Figure 3-20 for the "c" direction. One of the curves in each of these figures was taken from the data presented in Section 3.2.2.1, the substrate nucleated and the continuously nucleated curves were taken from Reference 17, and the data showing the variation from the top to the bottom layer in the PG coating were taken from Reference 9. These comparisons show that

- The type of coating nucleation can have a 20 percent effect on the thermal expansion of the PG
- The location of the PG (i.e., whether it is close to the mandrel or substrate or close to the surface) can have a 15 percent effect on the thermal expansion of the PG
- The reported thermal expansion data differ by as much as a factor of two for "a" direction but by only 15 percent for the "c" direction

Since the mismatch of the "a" direction thermal expansion between the coating and the substrate is the dominate cause of the hoop stress in the coating, the possible variation of this property between different types of PG is particularly significant.

Figure 3-21 shows the variation of the Young's modulus for different types of coatings. The variation in this property for just the tension values is on the order of 75 percent, and this variation occurs primarily at low and high material temperatures. In addition to the variation in material properties mentioned above, Reference 18 indicates that fabrication process variables can cause a factor of two variation in the "a" and "c" direction thermal conductivities and Reference 17 indicates fabrication process variables can cause a factor of two variation in the torsional strength of the PG coating.

After the structural analyses were well underway, the data presented in Reference 19 were obtained for AGSR. These data included stress-strain curves from shear and tensile specimens in the with and across grain direction. The with and across grain curves are compared in Figures 3-22 with the curve presented previously in Figure 3-12. The primary difference between the data presented in Reference 9 and the data used in the analysis is that the Young's modulus used in the analysis was assumed the same in the with and across grain directions whereas the data from Reference 16 shows a significant material anisotropy in the different grain directions.

#### 3.2.2.4 Mechanical Strength Properties

The mechanical property data presented in Sections 3.2.2.2 and 3.2.2.3 are sufficient for predicting the stress or strain distribution in the nozzle insert. However, except for the stress-strain curves which show specimen fracture, these data are not sufficient for predicting material failure. In reviewing the literature, the majority of the strength data for PG is presented in the form of an ultimate stress limitation based on data from uniaxial stressed specimens. Since the stress-strain curves for most graphites are nonlinear, the ultimate strain provides a more realistic basis for evaluating the structural capability of the insert. This is particularly true when evaluating the results of an elastic-plastic analysis. The following paragraphs present the ultimate stress and strain data which were found in the literature and which were used to evaluate the structural results presented in Section 5.

For the PG coating used in the 7 inch diameter nozzle insert, the most likely modes of failure are a compression failure in the "a" direction or an interlaminar shear failure. The compression strength in the "a" direction as a function of temperature (Reference 6) is shown in Figure 3-23. The interlaminar shear strength as a function of temperature (Reference 6) based on direct single shear tests is shown in Figure 3-24. Reference 9 gives room temperature shear strengths which range from 600 to 3200 psi depending on the method of measurement. In evaluating the structural analysis results, a nominal value of 1500 psi is used.

For coarse grain unannealed AGSR, ultimate tensile strengths and strains to fracture from References 11 and 19 are tabulated in Table 3-6.

TABLE 3-1

SPECIFIC HEAT AS A FUNCTION OF TEMPERATURE FOR  
SPEER 8882, SPEER 9139, AND AGSR BULK GRAPHITES, FOR PG COATING  
AND FOR MX 2600 SILICA CLOTH AND MX 4926 CARBON CLOTH PHENOLICS

PG Coating		AGSR Graphite		Speer Graphites		MX 2600 Silica Cloth Phenolic		MX 4926 Carbon Cloth Phenolic	
Temp (°R)	Specific Heat (Btu/lb°R)	Temp (°R)	Specific Heat (Btu/lb°R)	Temp (°R)	Specific Heat	Temp (°R)	Specific Heat*	Temp (°R)	Specific Heat*
525	.240	460	.130	492	.178	500	.210	500	.215
780	.276	850	.290	672	.242	1000	.362	1000	.365
1060	.313	1210	.360	850	.289	1500	.555	2000	.715
1390	.357	1930	.430	1030	.327	2000	.735	2500	.755
1850	.409	2650	.465	1390	.379	3000	.687	3000	.745
2190	.445	3370	.485	1750	.416	4000	.630	3500	.690
2650	.480	4090	.500	2290	.448	5000	.590	4000	.665
3060	.498	4810	.515	2650	.464	6000	.590	5000	.665
4460	.520	5520	.530	6000	.528			6000	.665
7460	.520								

\* Specific heat modified to account for in-depth material degradation

TABLE 3-2  
MATERIAL DENSITIES

Material	Density (lb/ft <sup>3</sup> )
PG Coating	137
AGSR	114
SPEER 8882	112
SPEER 9139	112
MX4926 Carbon Cloth Phenolic	89.4
MS2600 Silica Cloth Phenolic	108

TABLE 3-3  
POISSON'S RATIO FOR PYROLYTIC GRAPHITE COATING  
AND THE AGSR GRAPHITE SUBSTRATE

Poisson's Ratio	PG	AGSR
$\nu_{\theta r}$	0.90	--
$\nu_{\theta z}$	-0.16	0.05
$\nu_{r\theta}$	0.30	0.07
$\nu_{z\theta}$	--	0.10

**TABLE 3-4**  
**ESTIMATED GRAFOIL MECHANICAL PROPERTIES**

Property	Value
Thermal Expansion, in/in/°F	
Across Layers @ 70°F	15.0 x 10 <sup>-6</sup>
@ 4000°F	70.0 x 10 <sup>-6</sup>
With Layers	Same as PG
Elastic Modulus, psi	
With Layers	0.2 x 10 <sup>6</sup>
Across Layers	0.4 x 10 <sup>6</sup>
Poisson's Ratio	Same as PG
Compressive Strength, psi	12,000
Tensile Strength, psi	2,000

**TABLE 3-5**  
**ROOM TEMPERATURE YIELD STRESSES FOR**  
**AGSR AND PG**

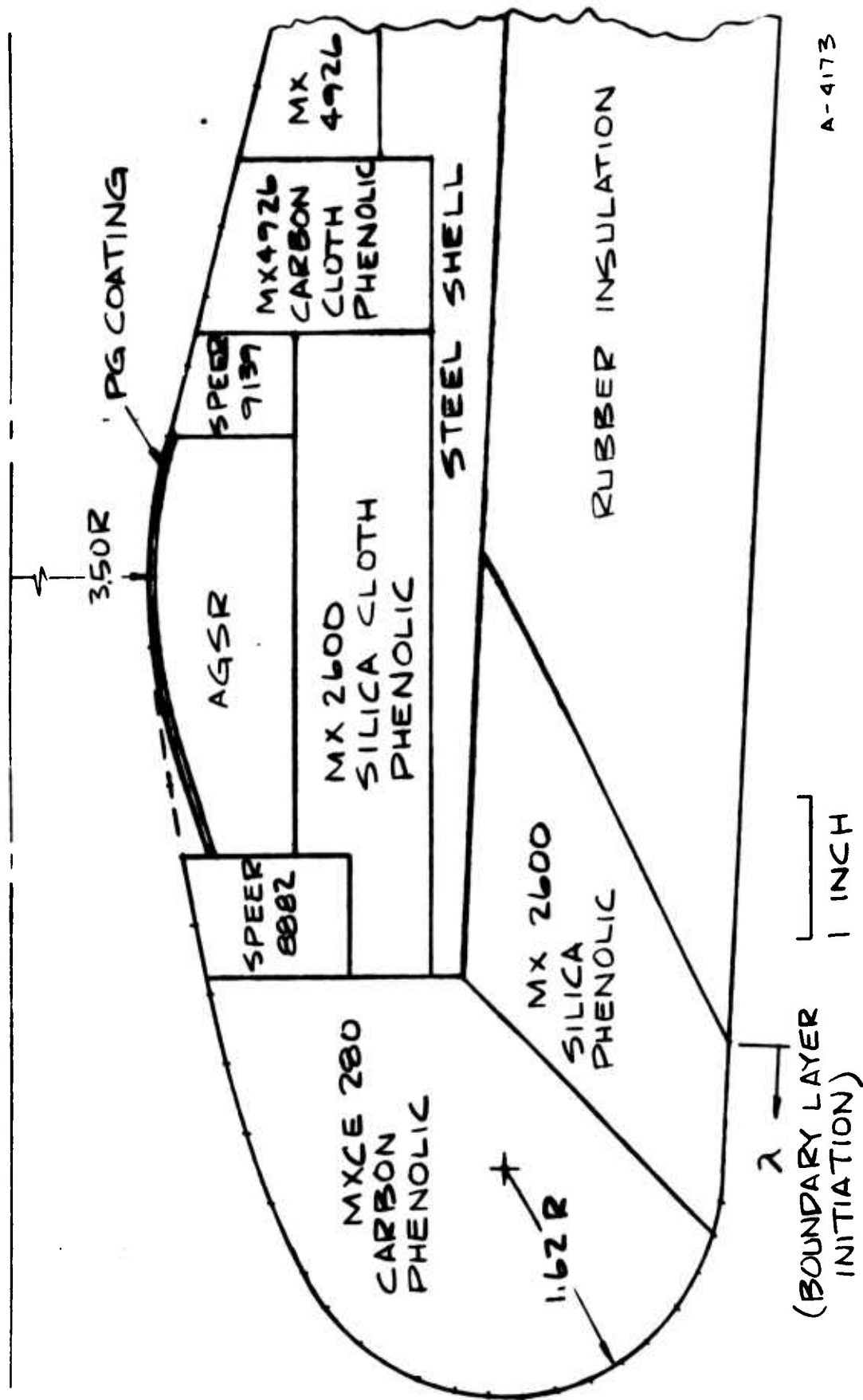
Material	Direction	Yield Stress (psi)
PG	"a" (tensile)	83,000
	"a" (compressive)	13,200
	"c" (tensile)	3,940
	"c" (compressive)	3,480
	Interlaminar Shear	300
AGSR	With & Across Grain	169
	Shear	80

TABLE 3-6

## STRENGTH DATA FOR AGSR GRAPHITE

Temperature (°F)	Ultimate Tensile Strength (psi)	Strain to Fracture (in/in)	Grain Direction	Reference
70	576	0.0015	Across	11
	378	0.0014		
	389	0.0014		
	490	0.0014		19
	800	0.0011	With	19
2000	696	0.0025	Across	11
	526	0.0017		
	482	0.0014		
3425	767	0.0022	Across	11
	676	0.0017		
70	720 <sup>a</sup>	0.0028	Radial <sup>b</sup>	19
	620 <sup>a</sup>	0.0018	Tangential <sup>b</sup>	
	790 <sup>a</sup>	0.0021	Axial <sup>b</sup>	

<sup>a</sup>Shear Strength<sup>b</sup>Torsion tests on radial, tangential, and axial specimens with the grain direction being parallel to the axis of the axial specimen



A-4173

FIGURE 3-1 LARGE PG COATED NOZZLE

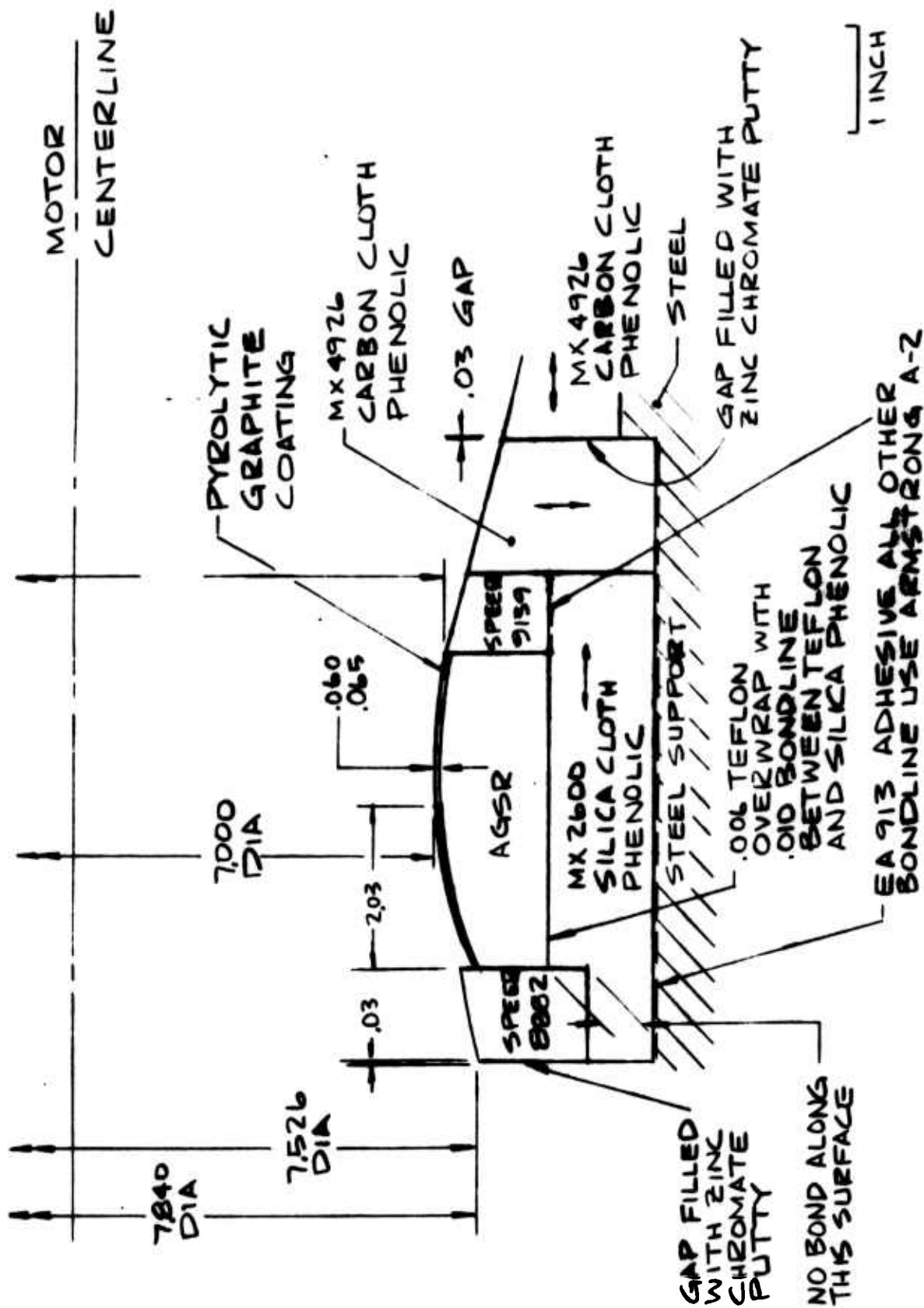
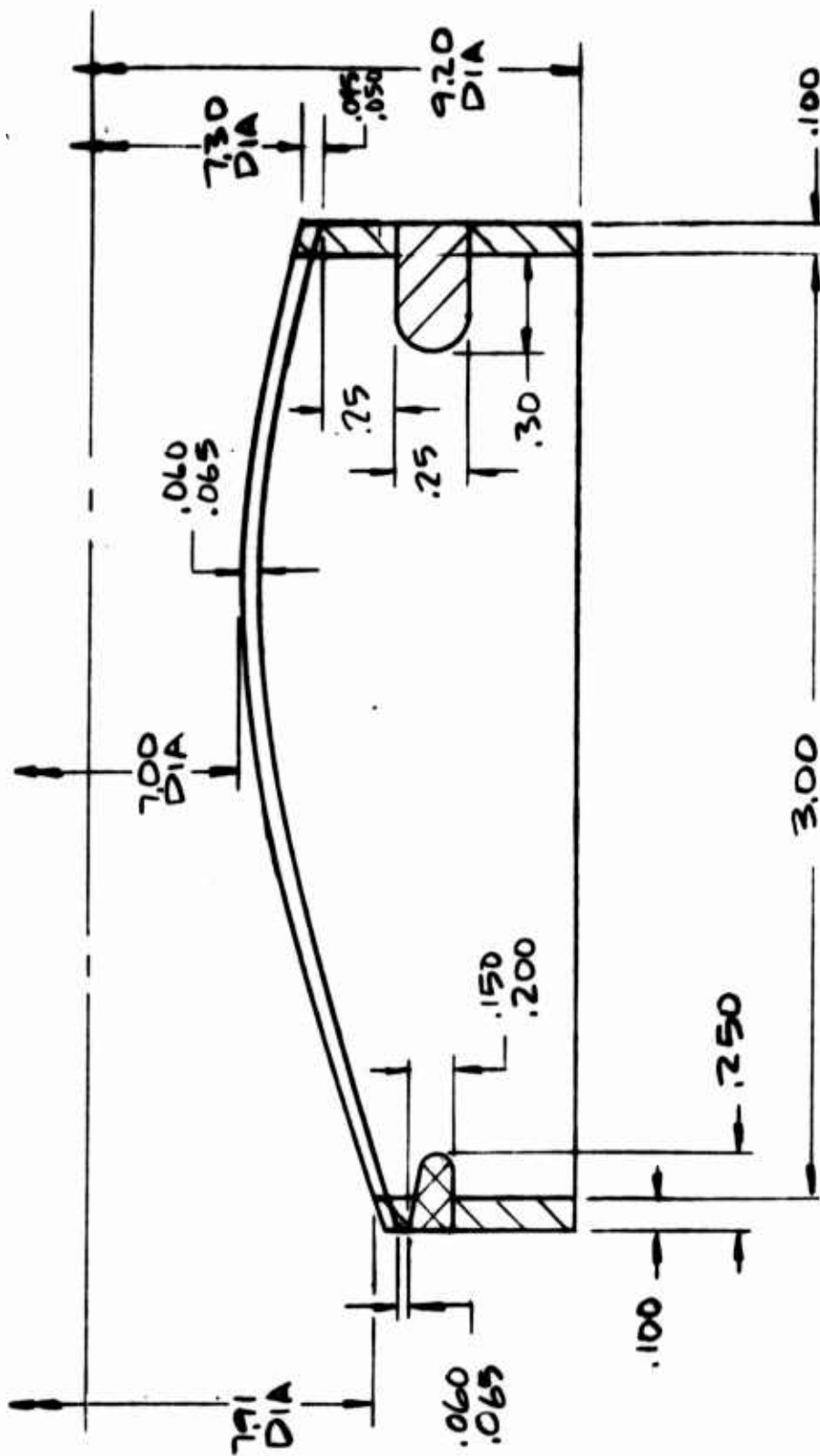


FIGURE 3-2 DEFINITION OF NOZZLE THROAT ASSEMBLY

A-4123





MACHINING OF  
PG COAT INSERT

/// MACHINE

/// STRESS RELIEVING  
GROOVE

FIGURE 3-3 PG COATED THROAT INSERT

A-4182

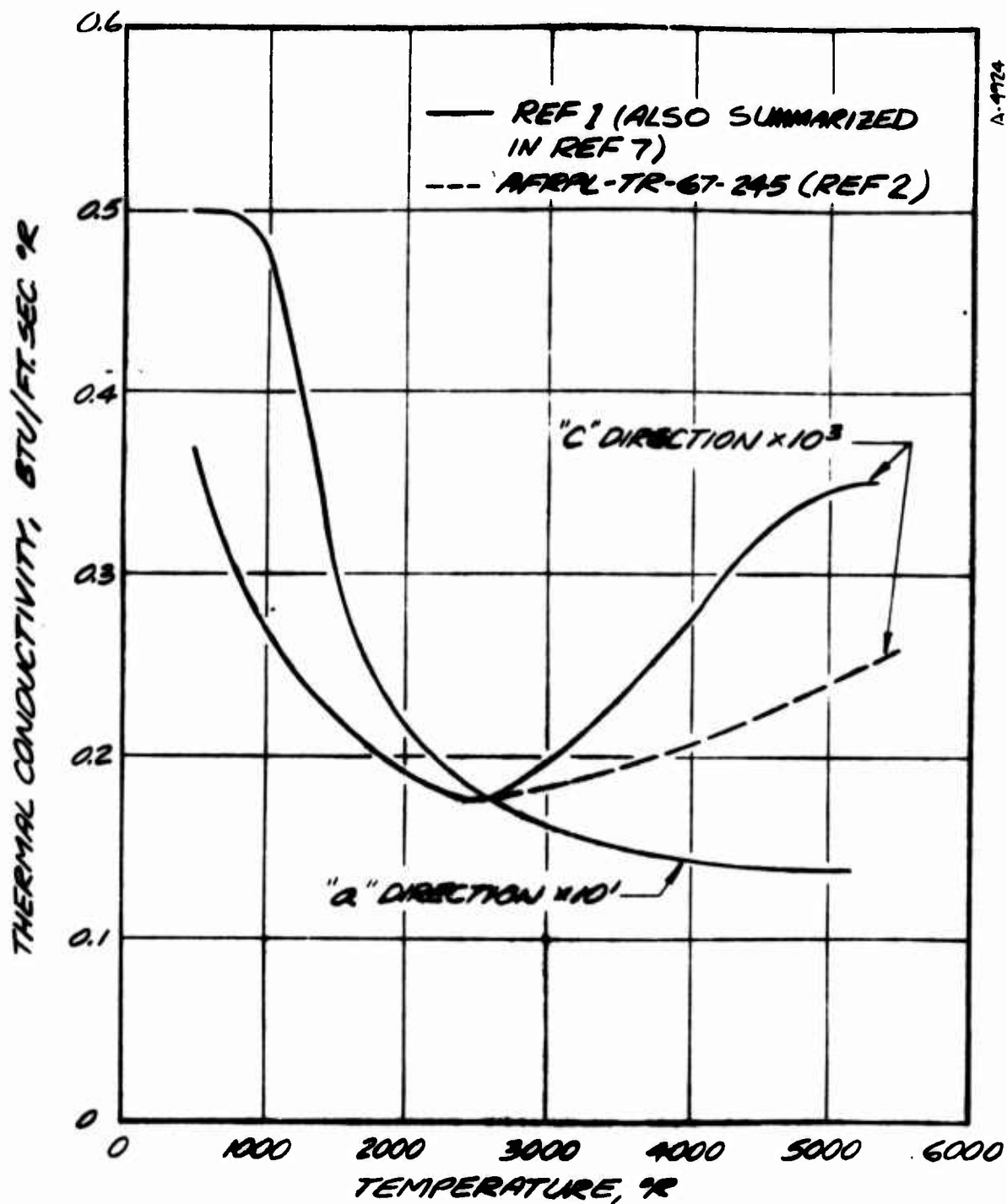


FIGURE 3-4 PYROLYTIC GRAPHITE THERMAL CONDUCTIVITY

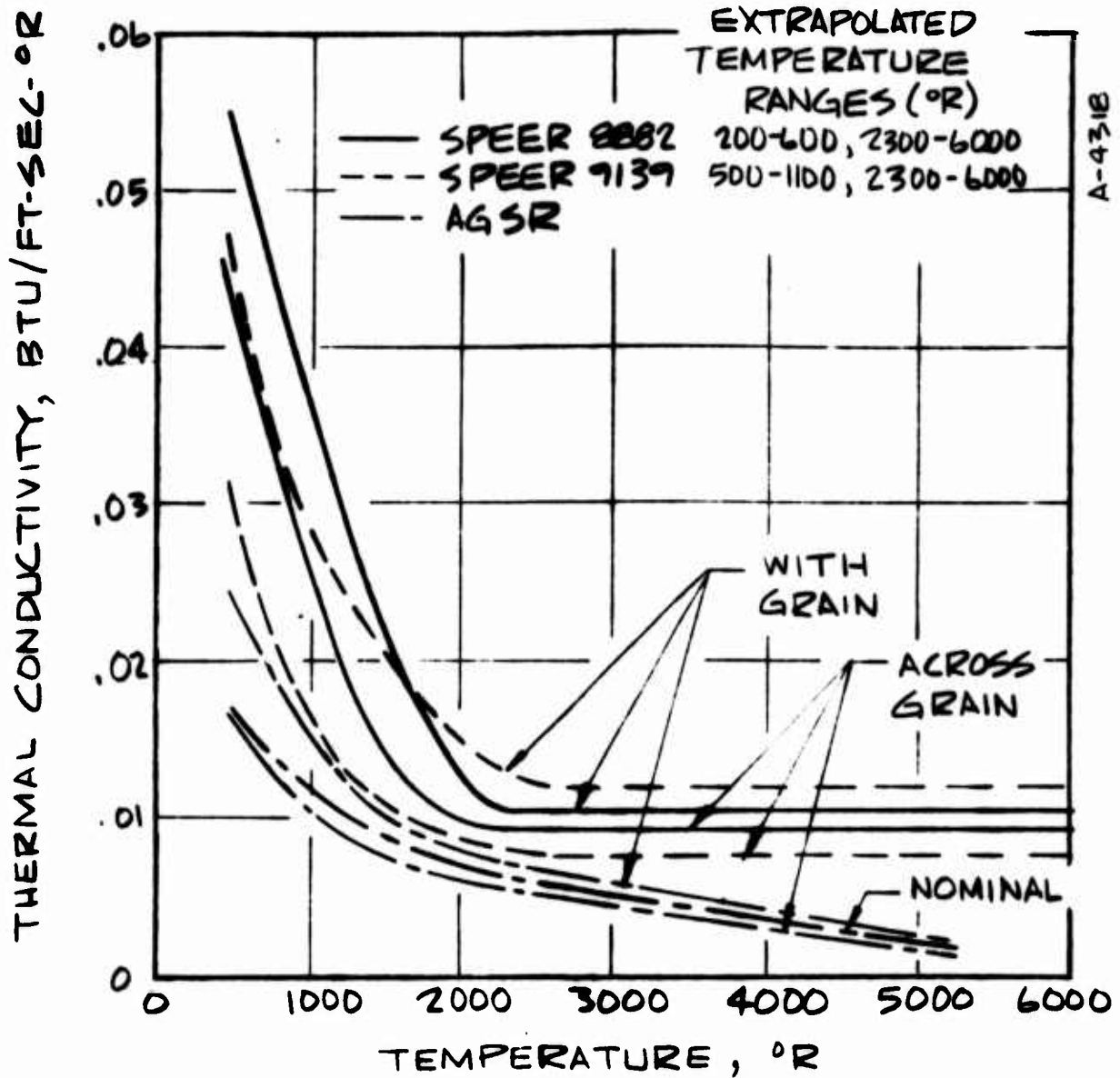


FIGURE 3-5 THERMAL CONDUCTIVITY FOR SPEER 8882, SPEER 9139, AND AGSR BULK GRAPHITES

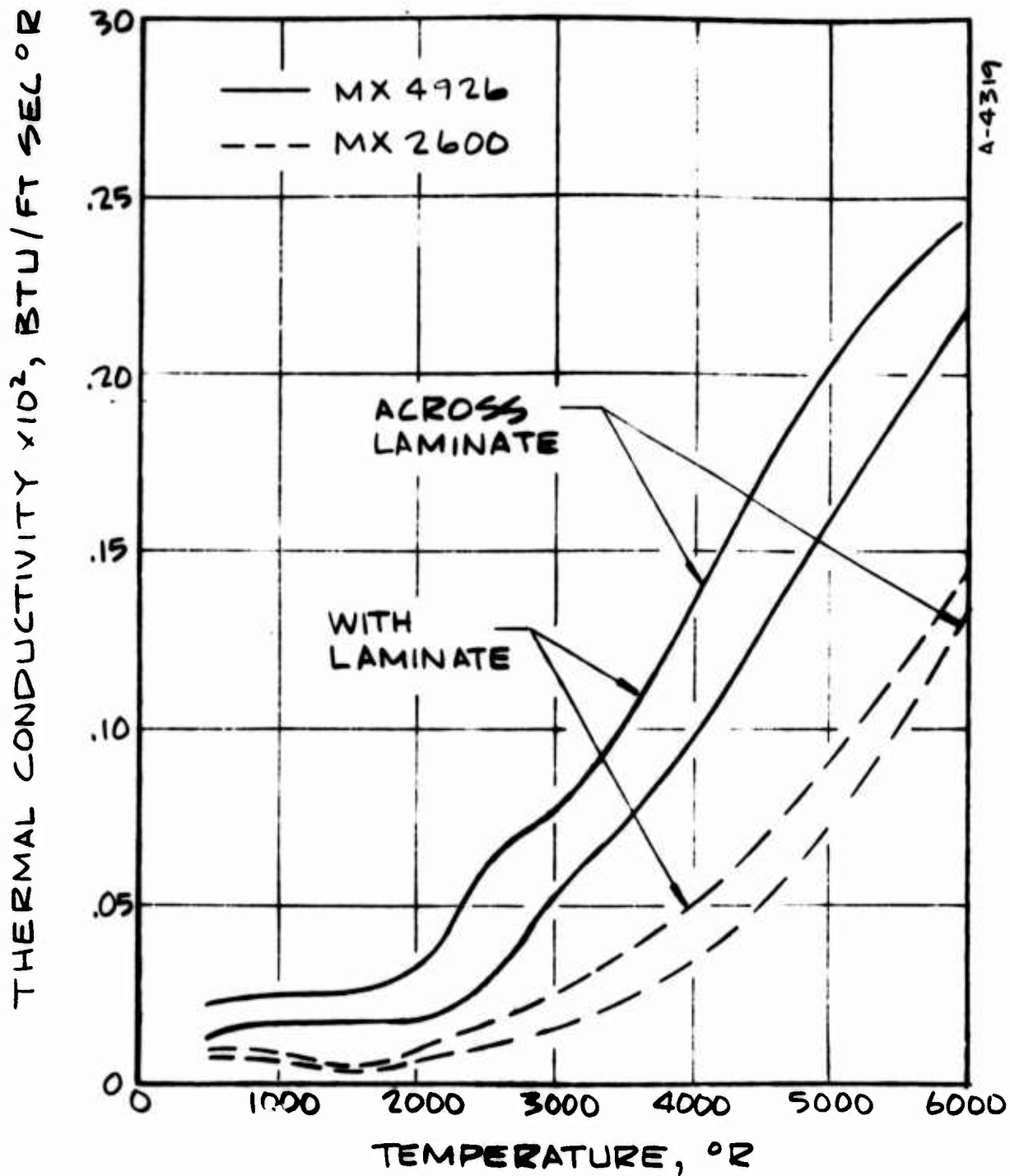


FIGURE 3-6 COMBINED VIRGIN AND CHAR THERMAL CONDUCTIVITY FOR MX 2600 SILICA CLOTH PHENOLIC AND MX 4926 CARBON CLOTH PHENOLIC

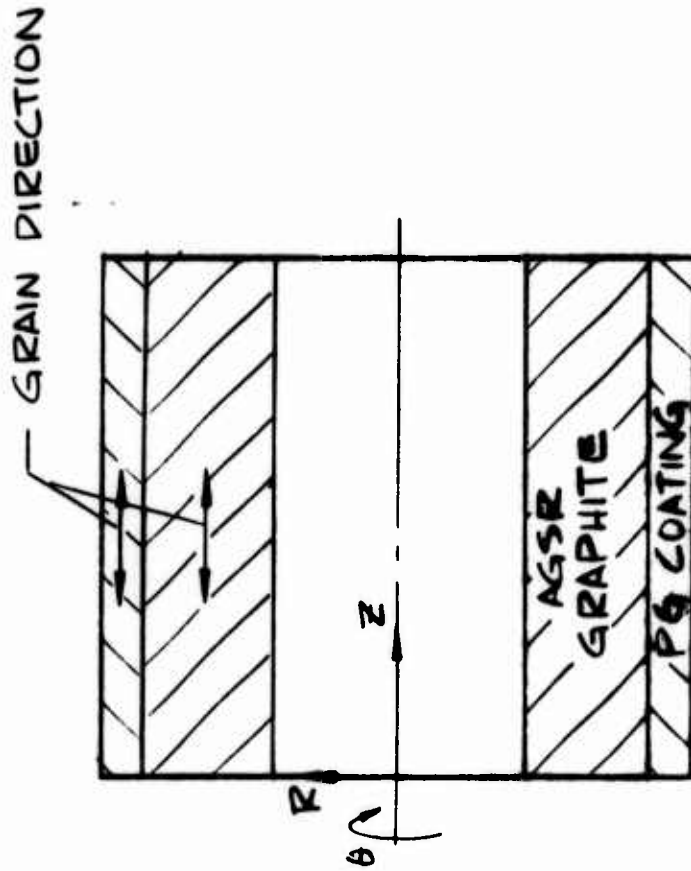


FIGURE 3-7A DEFINITION OF GRAIN DIRECTION

A-4925

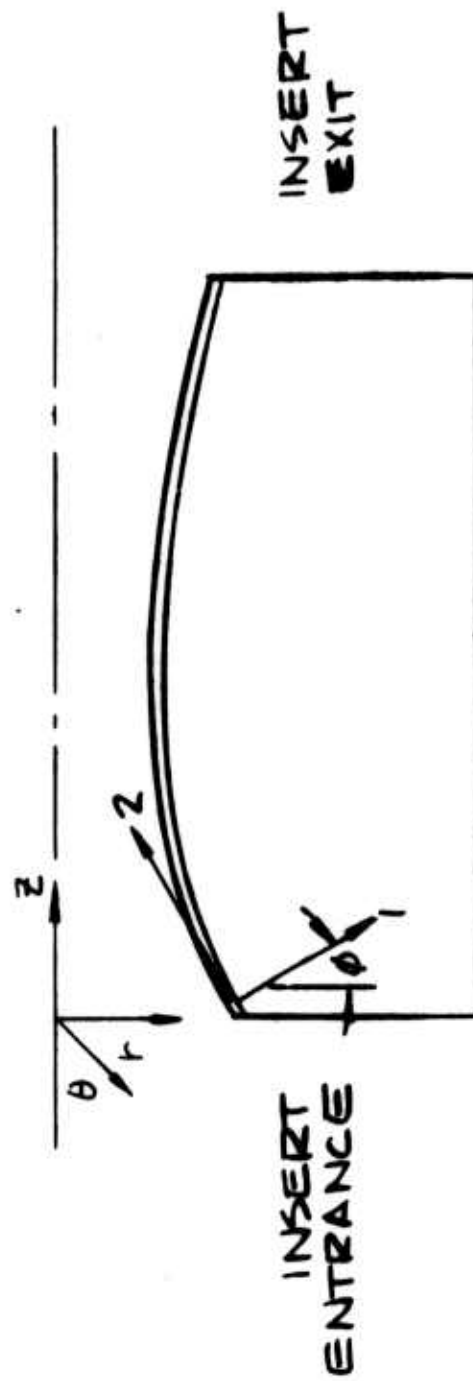


FIGURE 3-7B COORDINATE SYSTEM FOR NOZZLE THROAT INSERT

A-4926

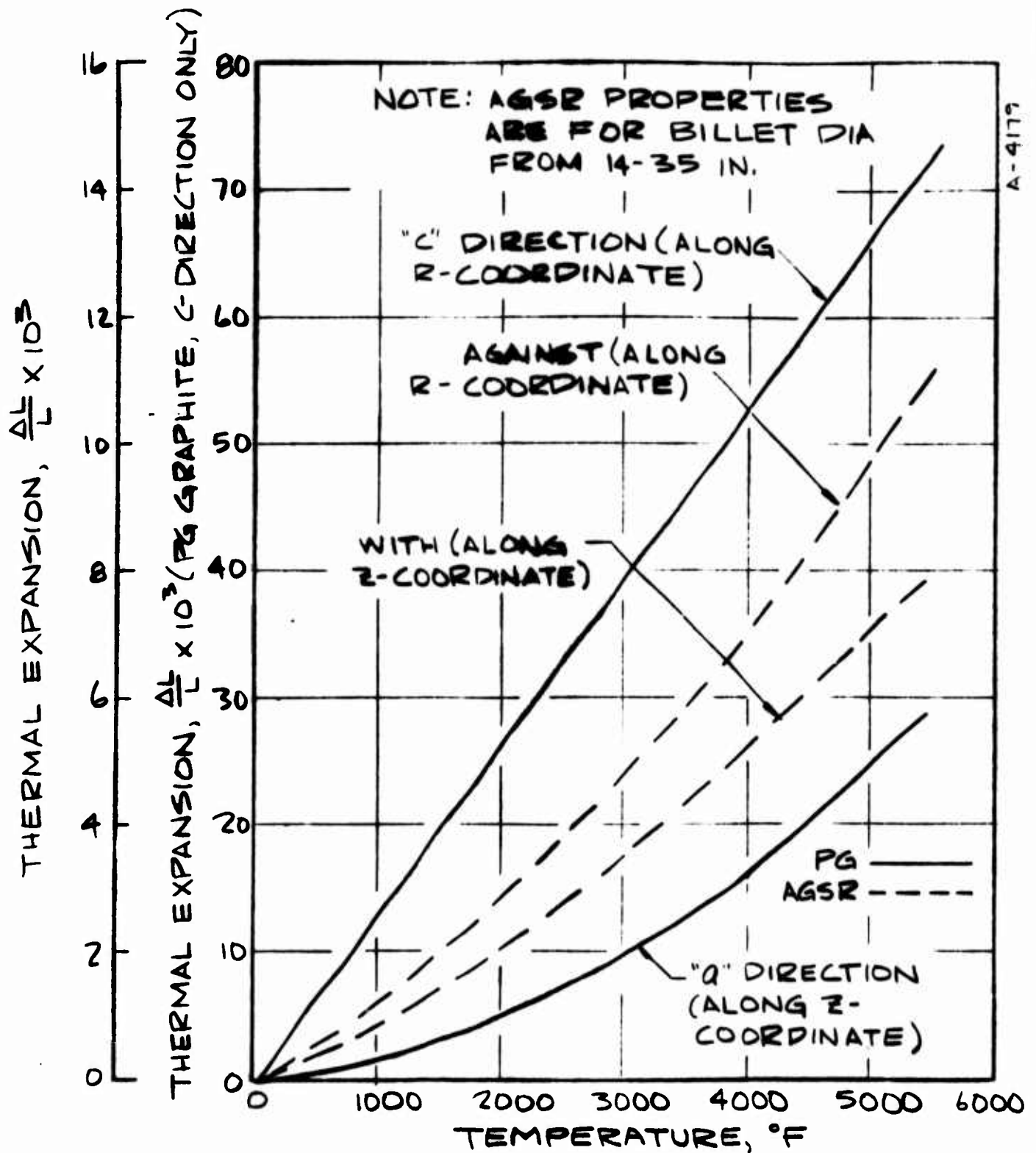


FIGURE 38 THERMAL EXPANSION PROPERTIES OF PYROLYTIC COATING AND AGSR GRAPHITE

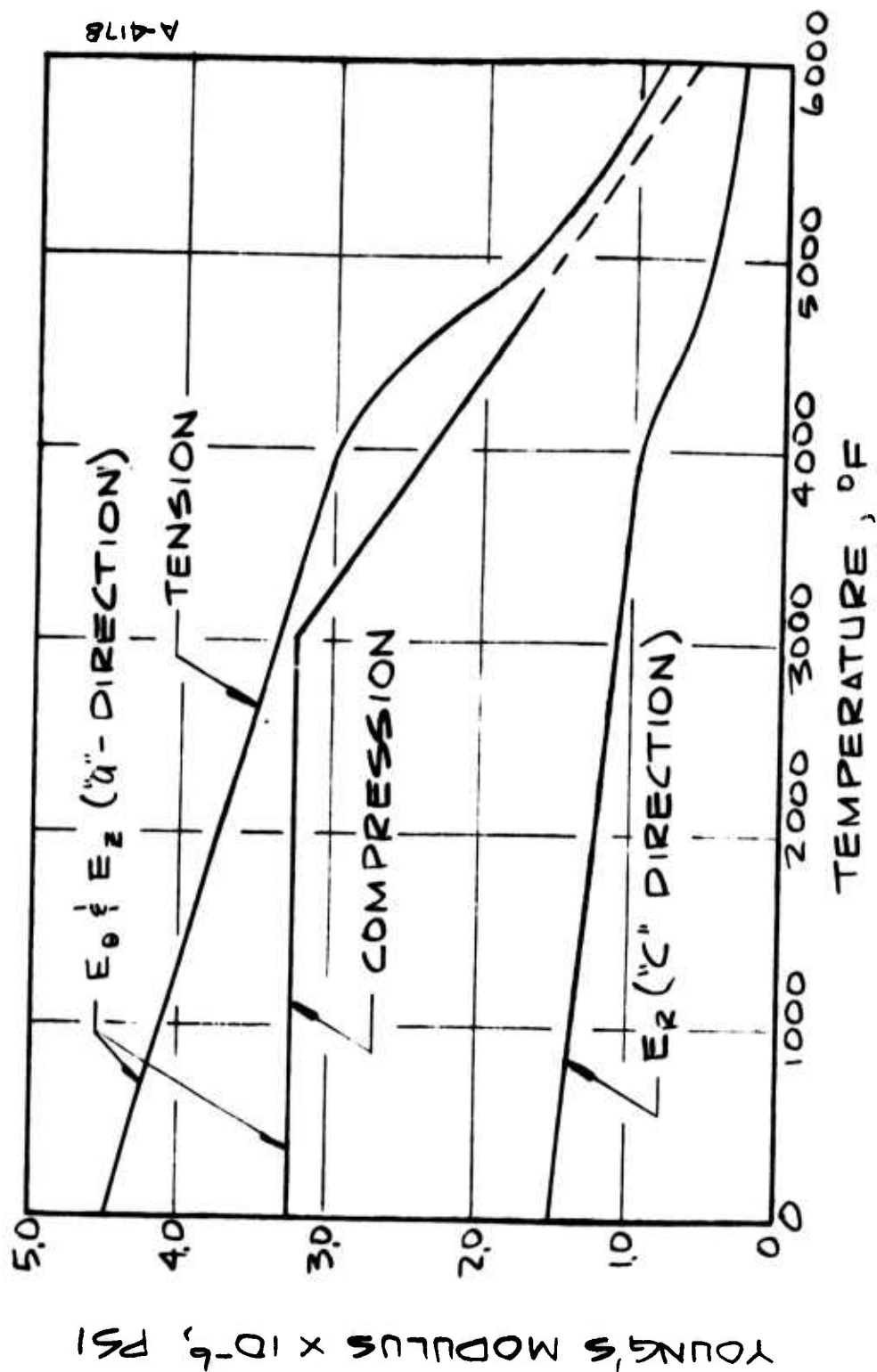


FIGURE 3-9 YOUNG'S MODULUS FOR PYROLYTIC GRAPHITE



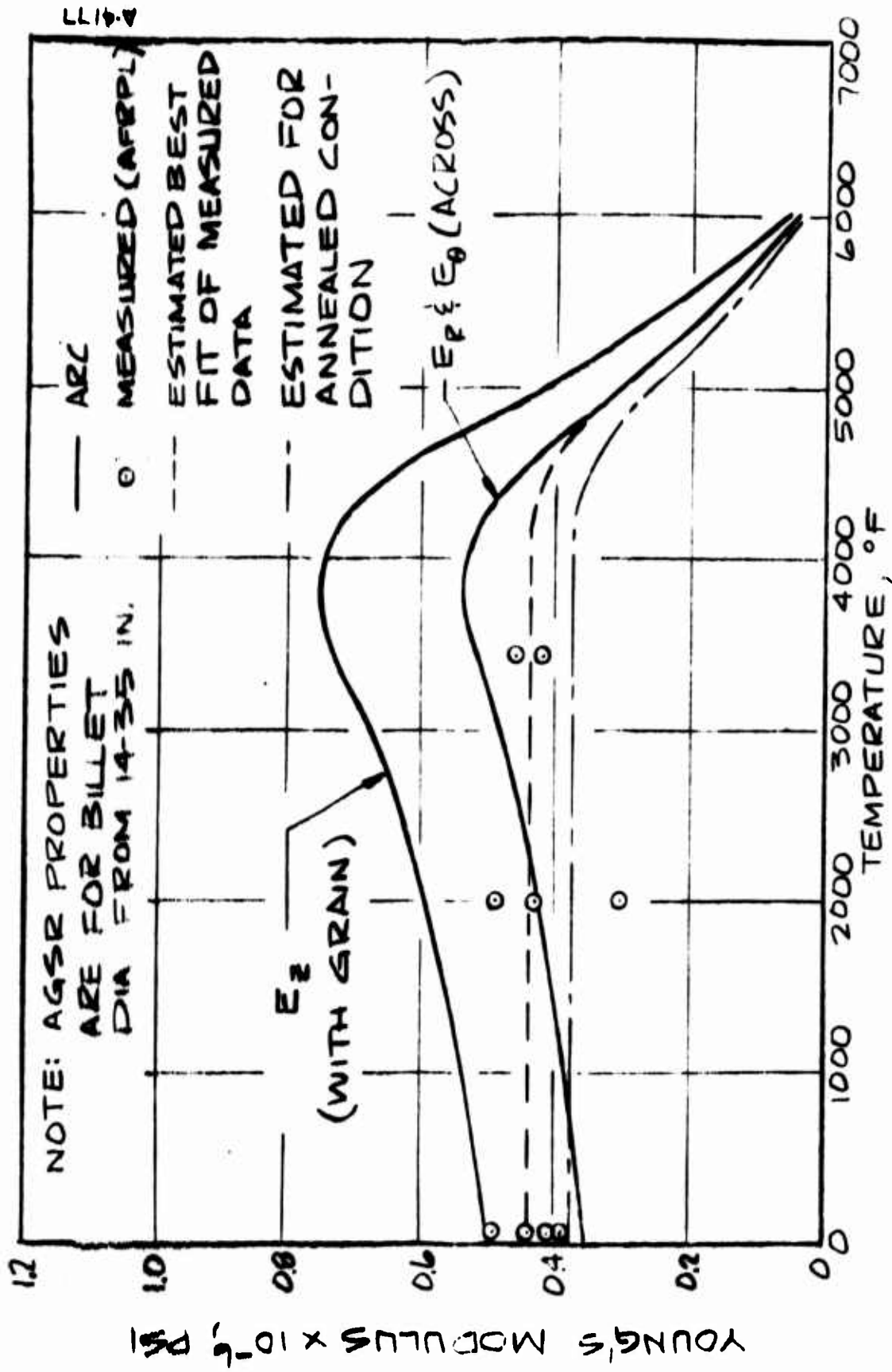


FIGURE 3-10 YOUNG'S MODULUS FOR AGSR GRAPHITE

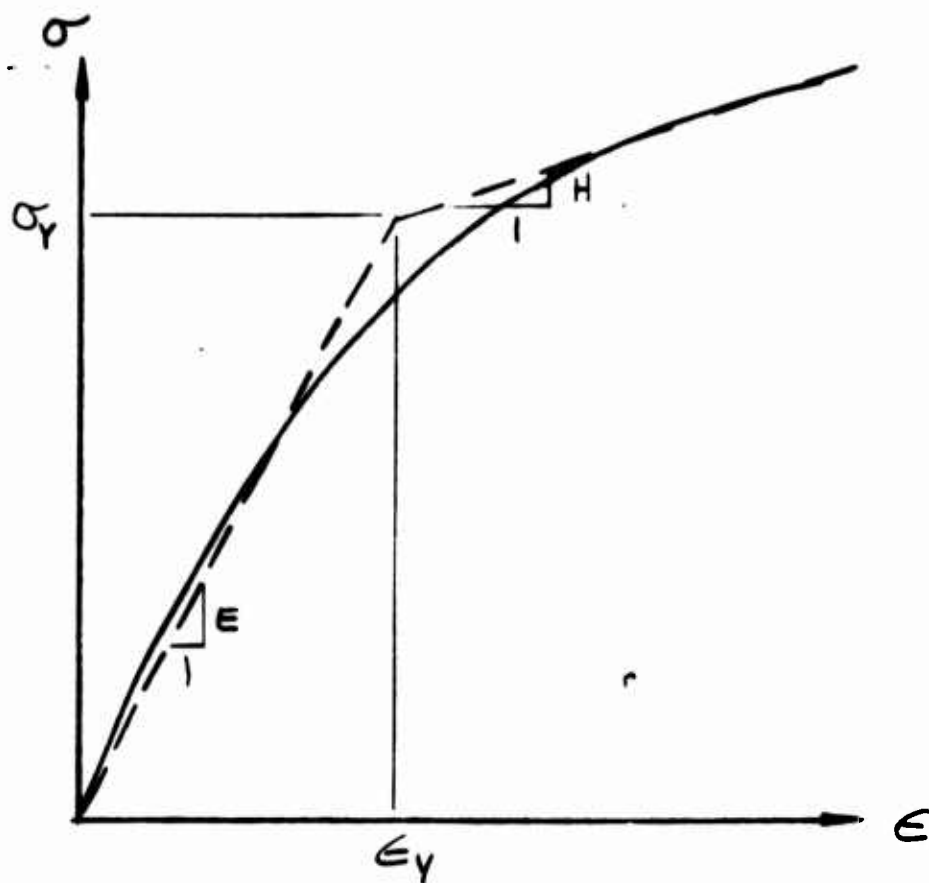


FIGURE 3-11 BILINEAR CURVE FIT OF  
STRESS STRAIN CURVE

A-1927

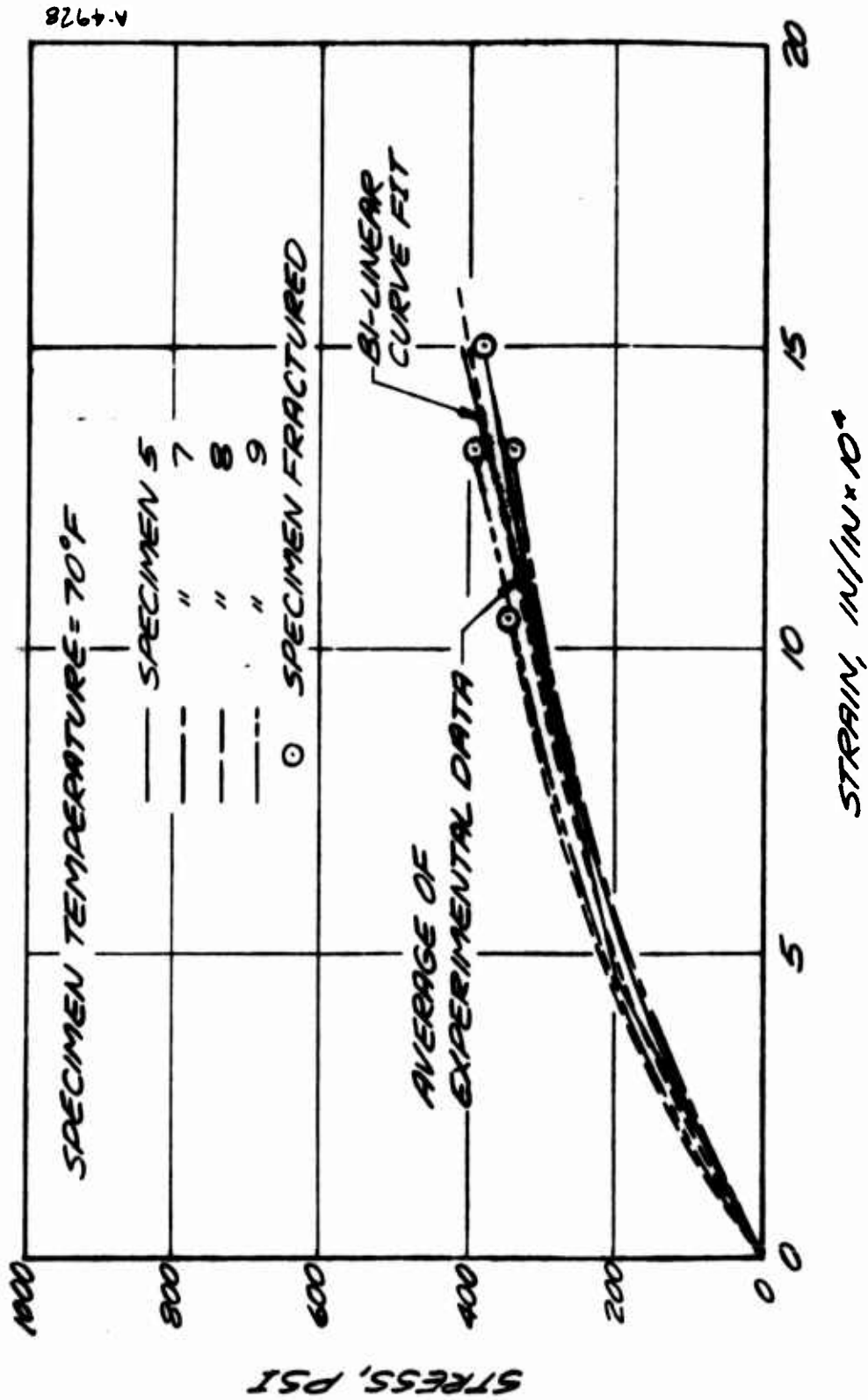


FIGURE 3-12 MEASURED BI-LINEAR CURVE FIT UNIAXIAL STRESS-STRAIN CURVES FOR AGSR GRAPHITE.

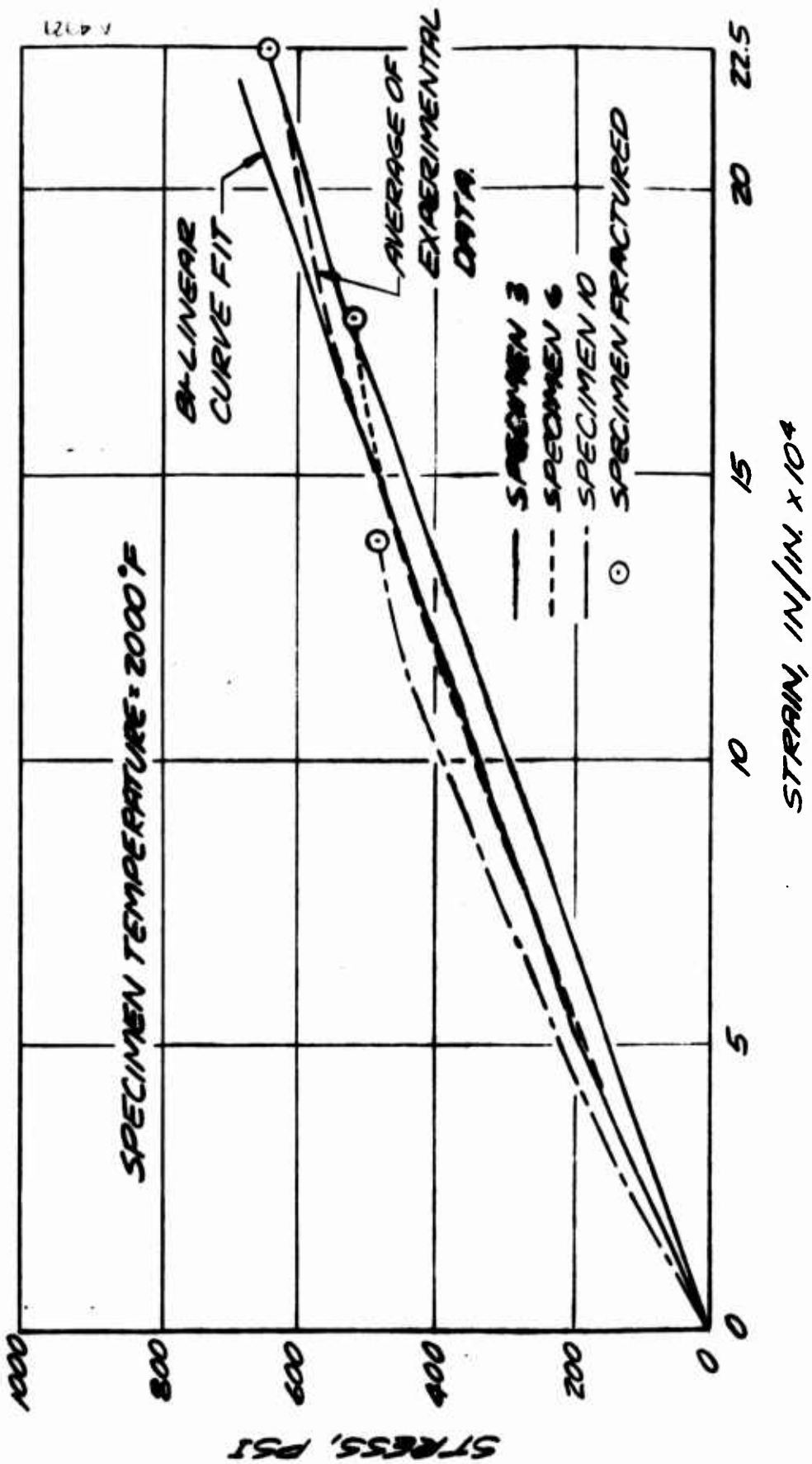


FIGURE 3-13 MEASURED AND BI-LINEAR CURVE FIT  
UNIAXIAL STRESS-STRAIN CURVES FOR  
AGSR GRAPHITE.

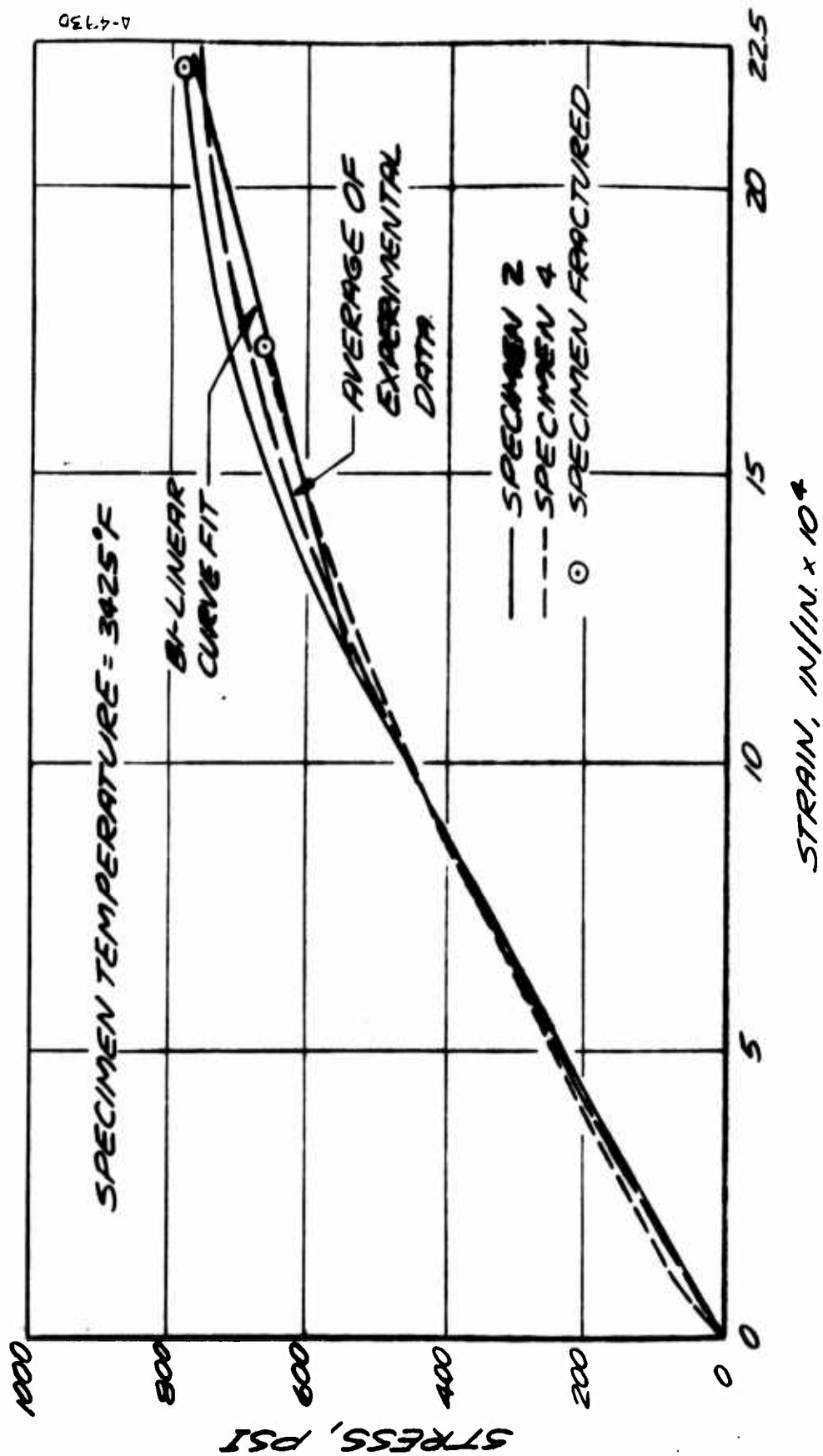


FIGURE 314 MEASURED AND BI-LATERAL CURVE FIT  
UNIAXIAL STRESS-STRAIN CURVES FOR  
AGSR GRAPHITE.

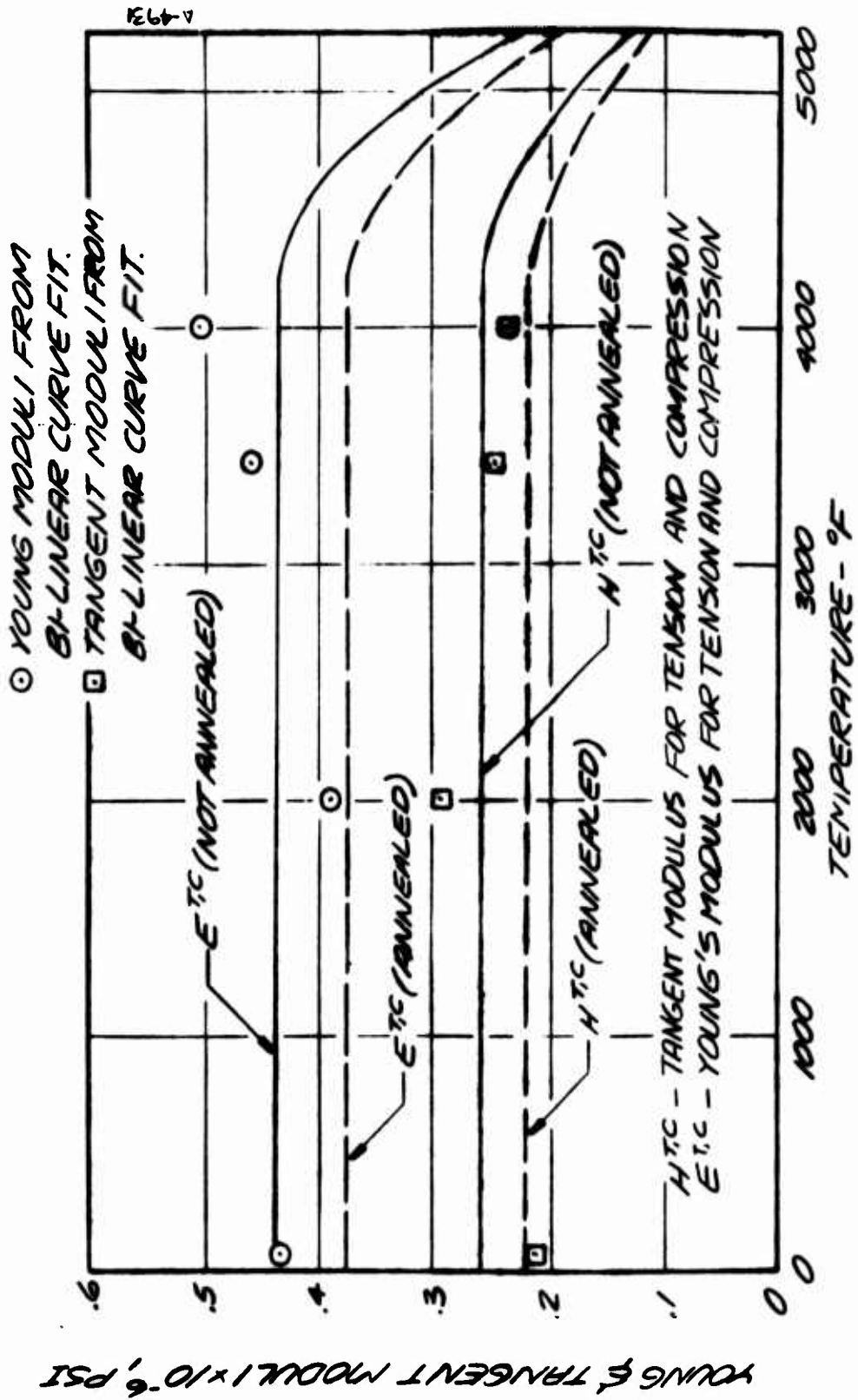


FIGURE 3-15 COURSE GRAIN AGSR BI-LINER MODULI

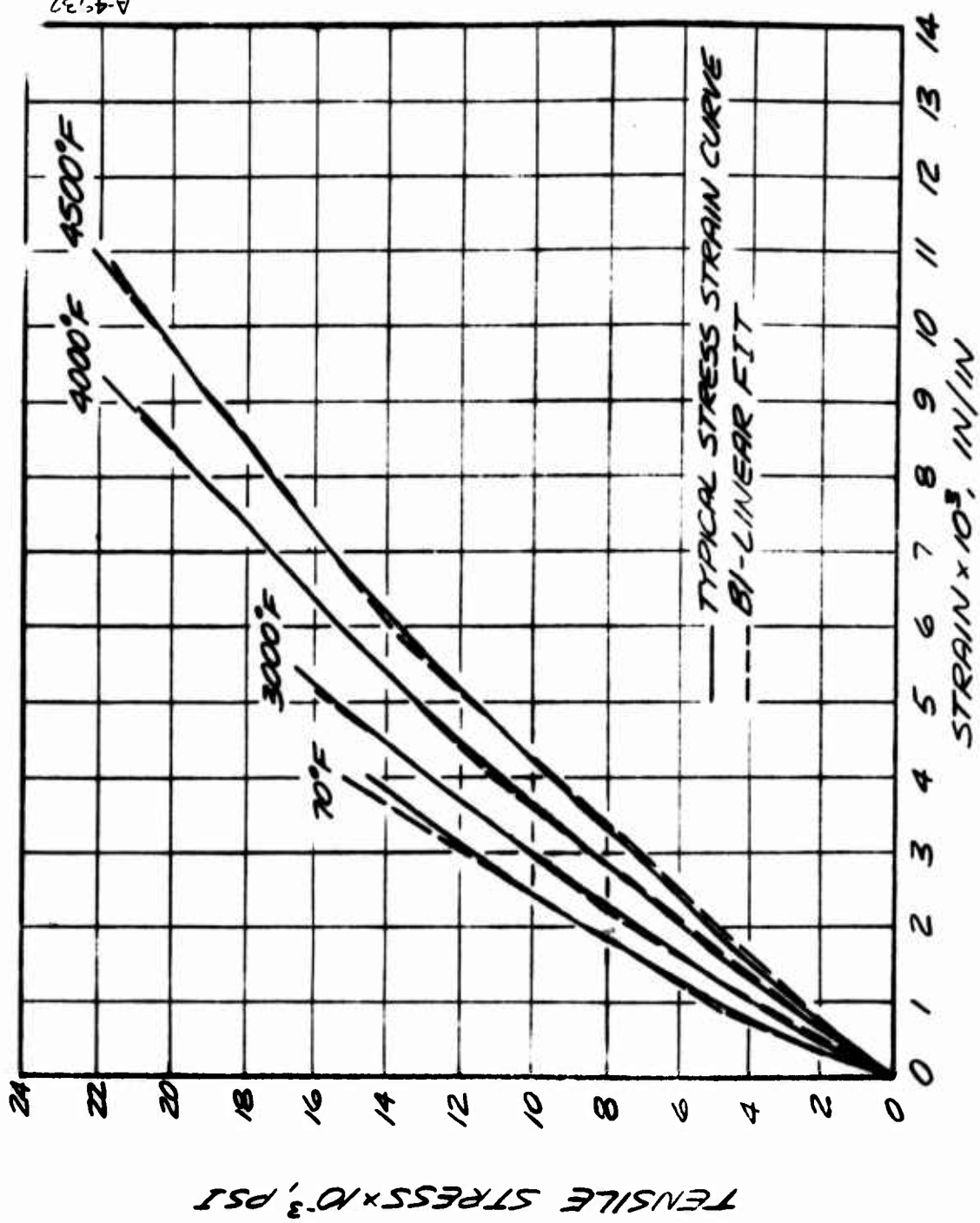


FIGURE 3-16 BI-LINEAR TENSILE STRESS-STRAIN CURVES FOR PYROLYTIC GRAPHITE, "A" DIRE

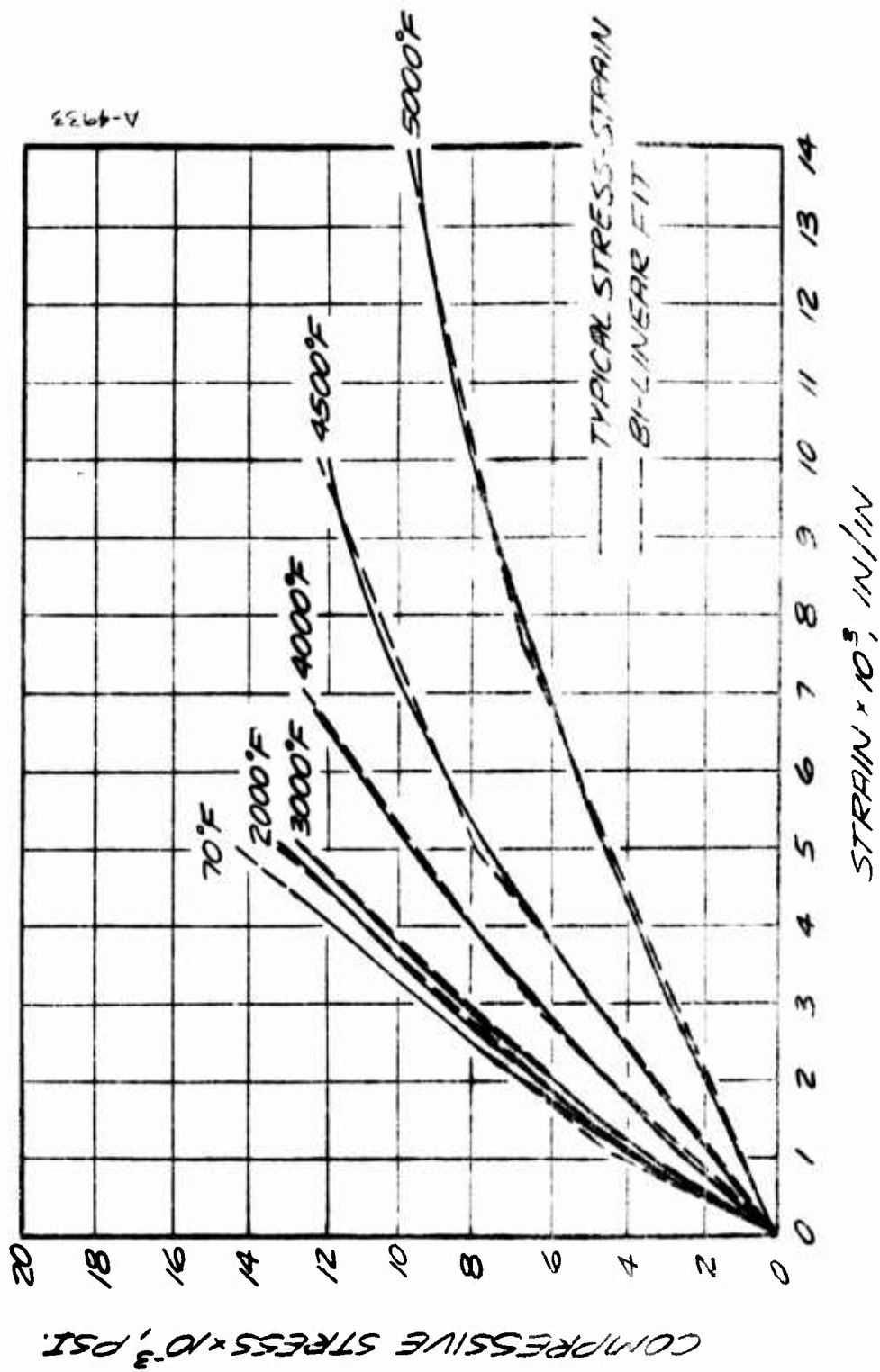


FIGURE 3-17 BI-LINEAR COMPRESSIVE STRESS-STRAIN CURVE FOR PYROLYTIC GRAPHITE, "a" DIRECTION.



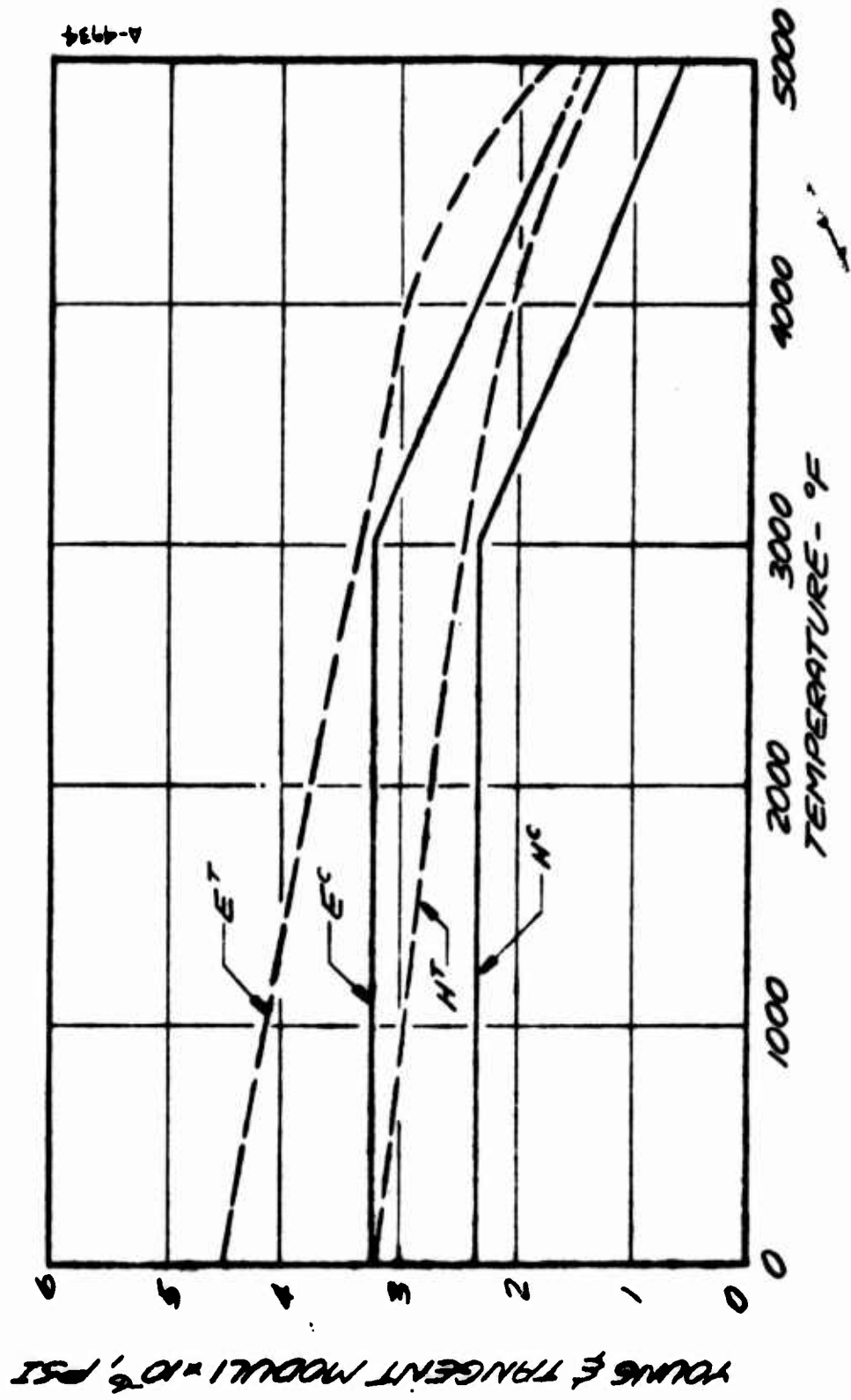


FIGURE 3-18 PYROLYTIC GRAPHITE BI-LINEAR MODULI

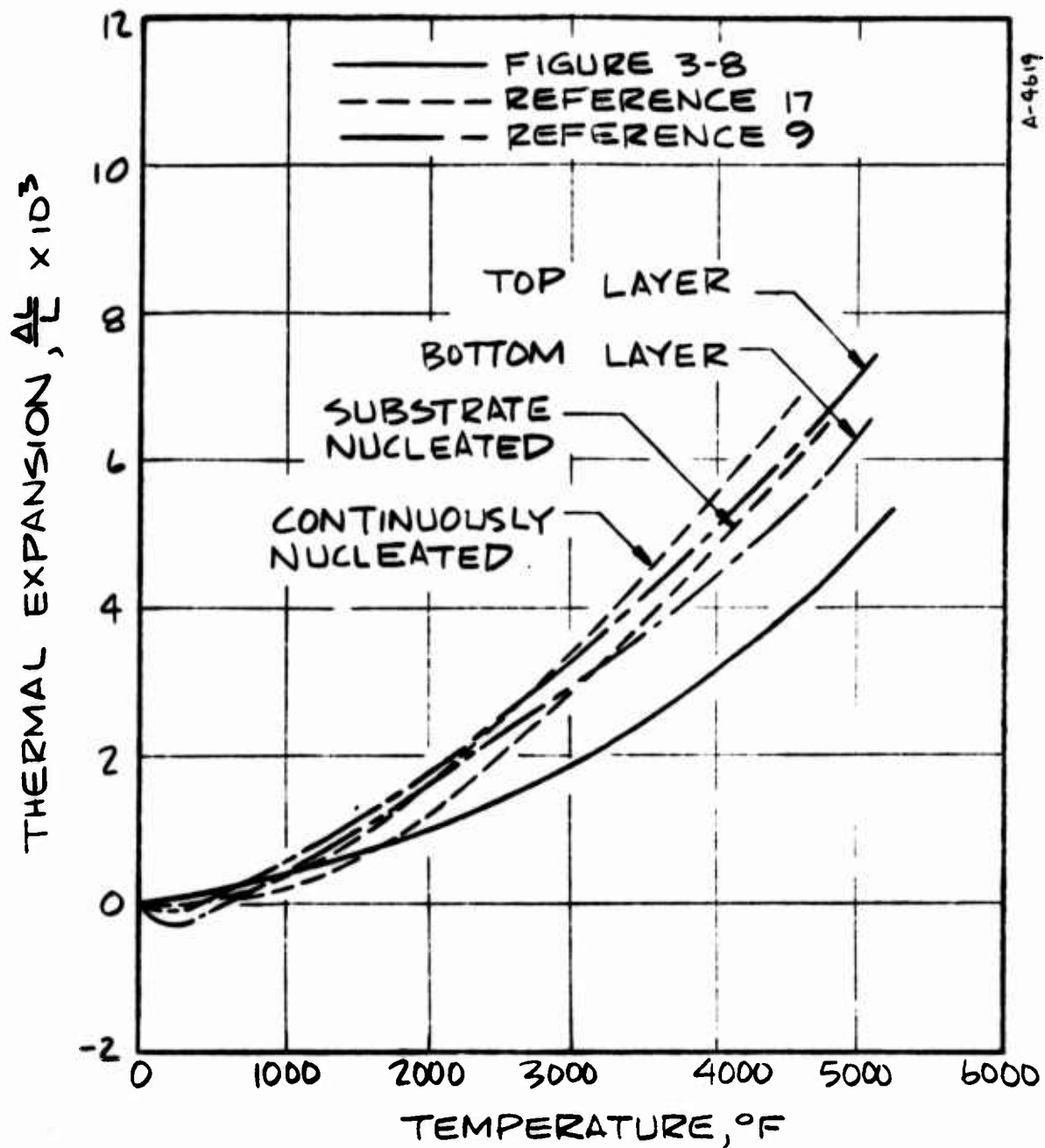


FIGURE 3-19 COMPARISON OF "a" DIRECTION  
PYROLYTIC GRAPHITE THERMAL EXPAN-  
SION

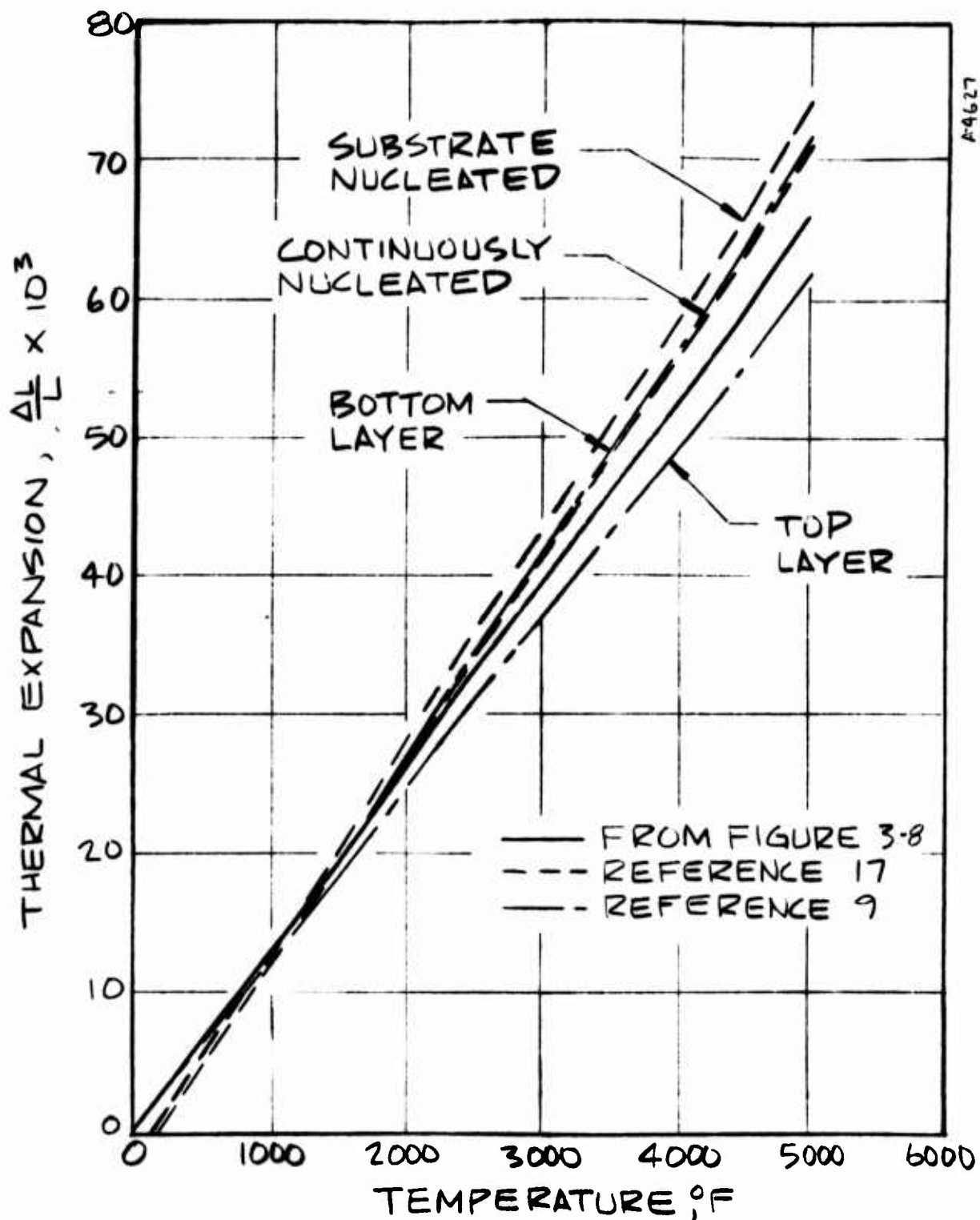


FIGURE 3-20 COMPARISON OF "C" DIRECTION  
PYROLYTIC GRAPHITE THERMAL EXPANSION

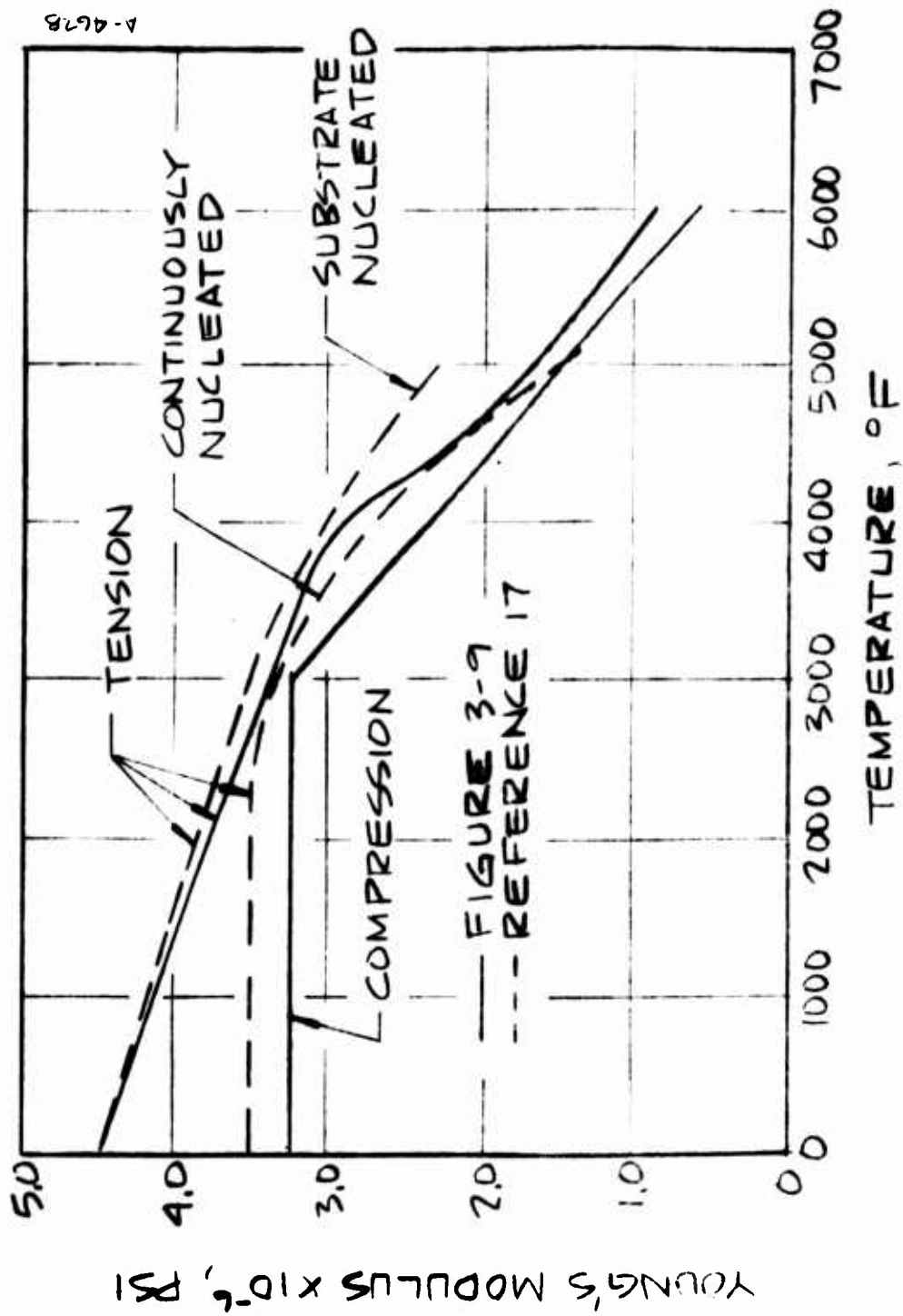


FIGURE 3-21 COMPARISON OF "A" DIRECTION PYROLYTIC GRAPHITE YOUNG'S MODULUS

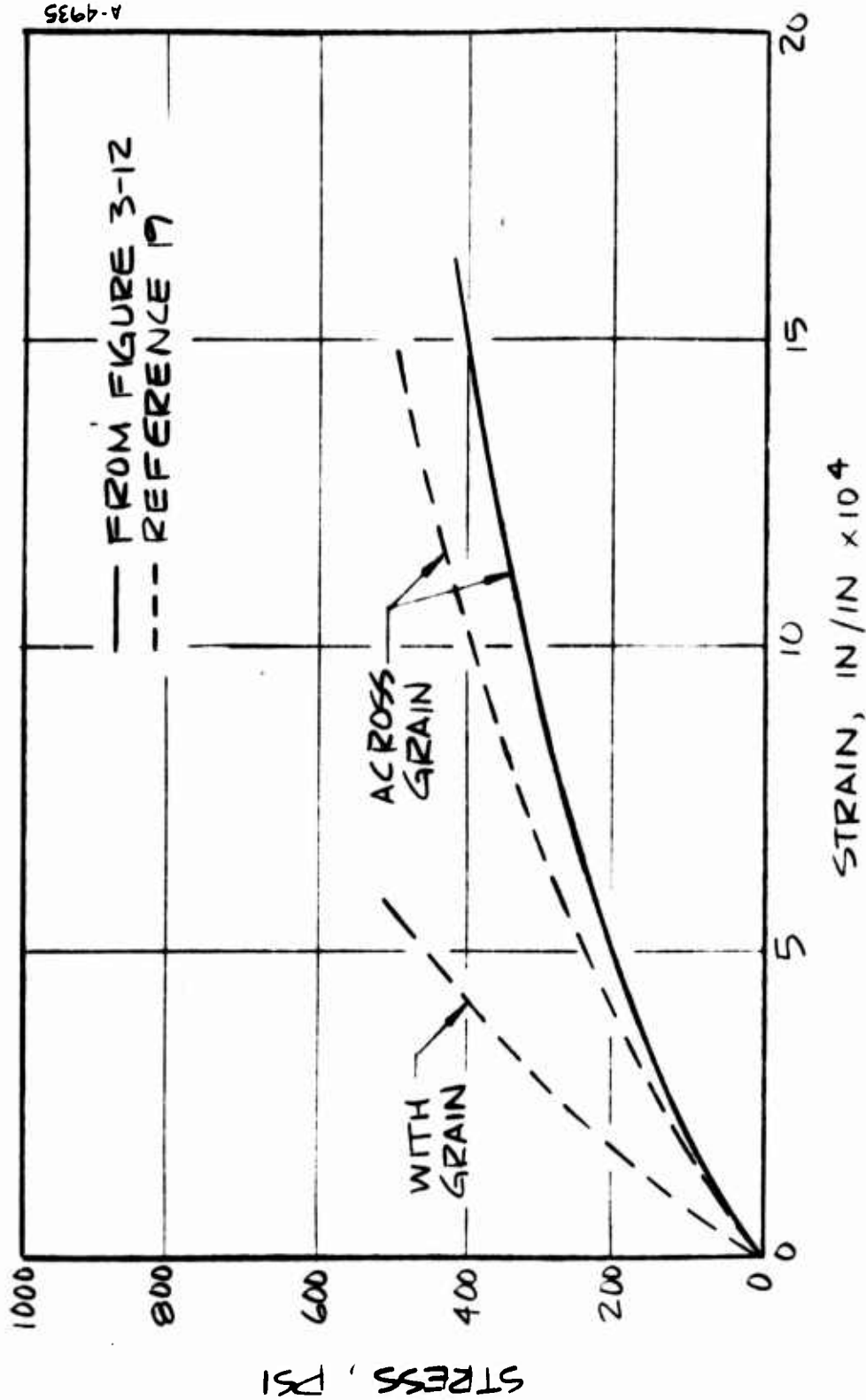


FIGURE 3-22 COMPARISON OF TENSILE STRESS-STRAIN DATA FOR AGSR GRAPHITE

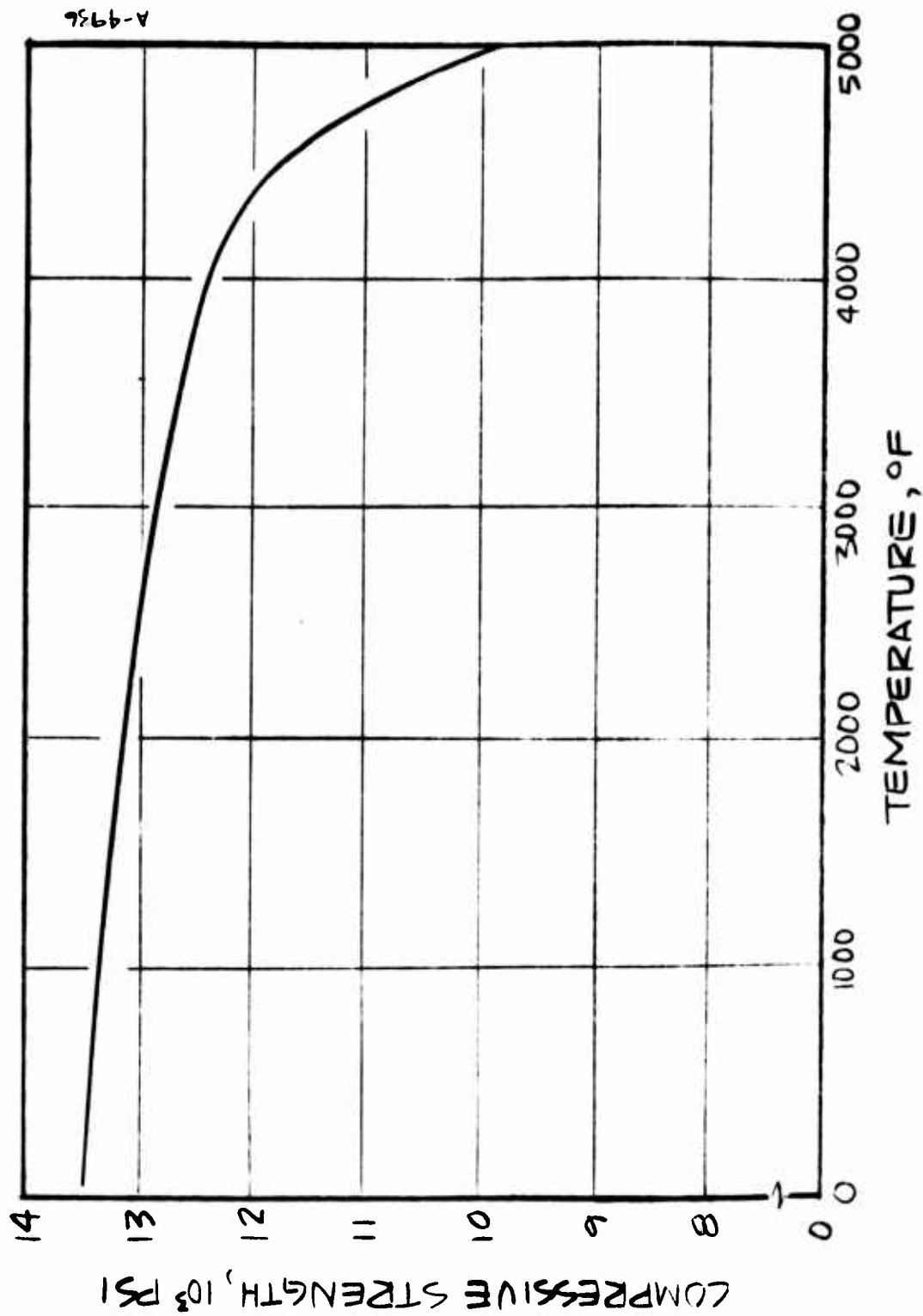


FIGURE 3-23 COMPRESSIVE PROPERTIES VERSUS TEMPERATURE FOR PYROLYTIC GRAPHITE IN "a" DIRECTION

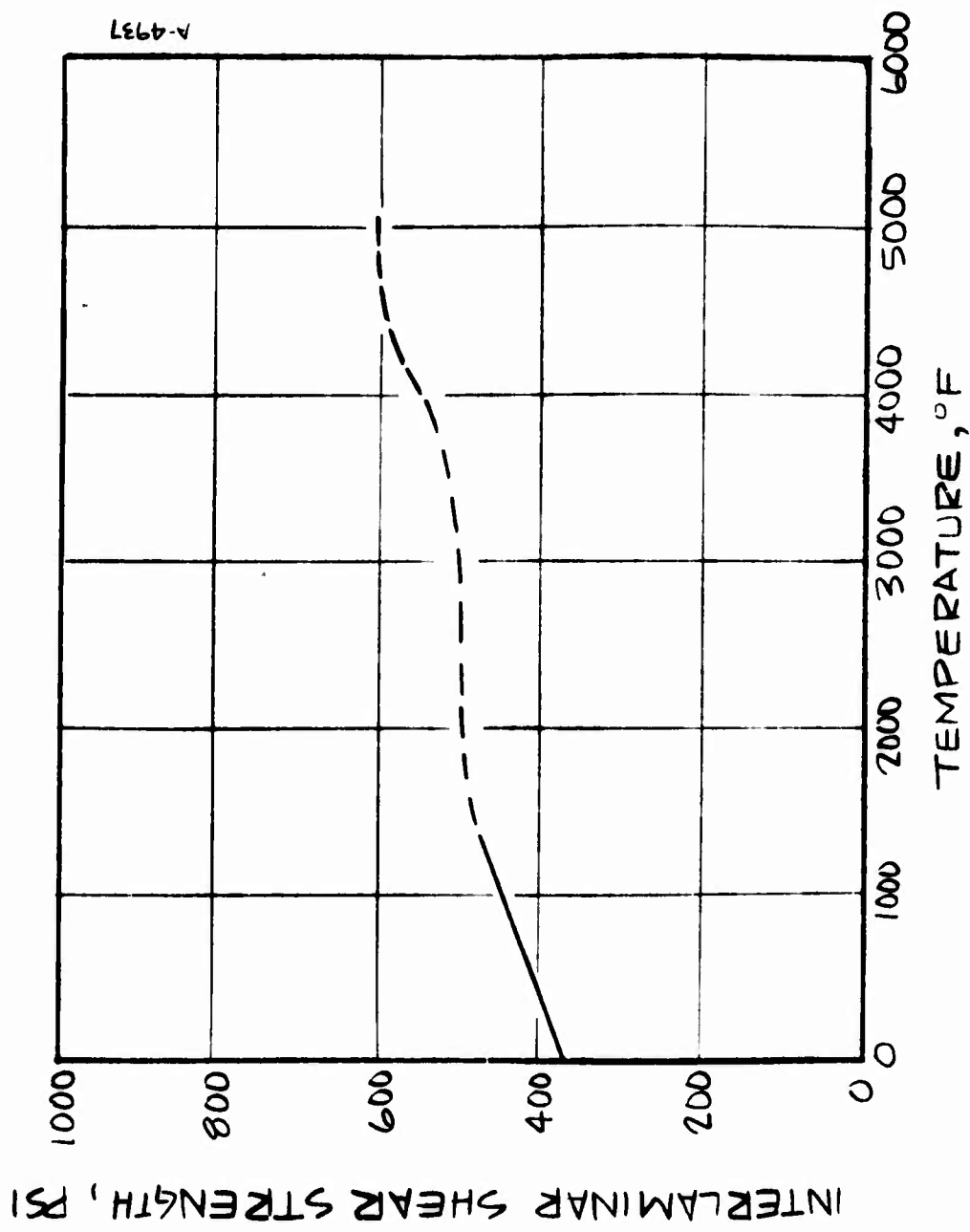


FIGURE 3-24 INTERLAMINAR SHEAR STRENGTH VS. TEMPERATURE FOR PYROLYTIC GRAPHITE

## SECTION 4

### THERMOCHEMICAL ANALYSIS

The results of a detailed thermochemical analysis in the form of surface recession histories and transient in-depth temperature histories are required as input to the thermostructural analysis.

The thermochemical analysis procedure and the corresponding design tools for generating this information are summarized in Section 4.1; the information concerning the nozzle environment which provides the input to the analysis is presented in Section 4.2; and the thermochemical performance of the nozzle materials is defined in Section 4.3.

#### 4.1 ANALYTICAL TECHNIQUES

The analysis of material response to a rocket nozzle environment encompasses both the determination of surface recession due to chemical corrosion and mechanical erosion and the evaluation of in-depth heat conduction and material decomposition. A set of comprehensive computerized analysis tools have been developed to define the thermochemical performance of materials which are typically used in rocket nozzle designs. These computer codes are used to evaluate thermal ablation phenomena, and they have been designed to be applicable for arbitrary material and propellant compositions and for any general environmental duty cycle specifications.

The computer codes utilized for the thermochemical calculations of the 7.0 inch diameter PG coated nozzle throat assembly were as follows:

- Aerotherm Chemical Equilibrium (ACE) Program<sup>\*</sup>
- Aerotherm Real Gas Energy Integral Boundary Layer (ARGEIBL) Program
- Axi-Symmetric Transient Heating and Material Ablation (ASTHMA) Program

The first program computes the thermochemical state of any set of chemical elemental quantities. For ablative rocket nozzle considerations, the code assists in the computations of nozzle expansion properties, gas phase transport and thermodynamic state properties, pyrolysis gas enthalpy-temperature relationships, and

---

<sup>\*</sup>The ACE program combines all the features of the Equilibrium Surface Thermochemistry, Version 3 (EST3) code (currently available to the rocket technology community) and the graphite response code developed under Contract F04611-69-C-0081 to account for surface kinetics.



thermochemical behavior of a surface material in contact with the hyper-thermal boundary layer flow. The surface removal mechanisms considered by the code are diffusion or kinetically controlled chemical corrosion, surface vaporization, and liquid layer removal.

The ARGEIBL program calculates bulk film transfer coefficients for non-ablating laminar and/or turbulent boundary layers of axisymmetric bodies or flat plates using an energy integral method. The solution procedure allows any real gas chemical system because it accepts generalized thermodynamic property information which are obtained from ACE code computations. Variations in axial surface temperature and free stream properties are accounted for in the integral procedure. The convective heat transfer coefficient distributions computed using the ARGEIBL technique have been confirmed by solutions generated with the more sophisticated Boundary Layer Integral Matrix (BLIMP) computer code (Reference 20).

Both the ACE and ARGEIBL codes are utilized to provide information needed by the ASTHMA material response code. The ASTHMA code is used to evaluate the transient response of nondecomposing materials such as graphite within which two-dimensional heat conduction effects are important. The surface boundary condition options include surface recession due to either diffusion or kinetically controlled chemical corrosion. More complete descriptions of the capabilities of the ACE, ARGEIBL, and ASTHMA computer codes are given in References 21 through 24.

The sequence of events in the analysis procedure is outlined in Figure 4-1. The major results of each analysis step in the procedure is defined along with how this result is used to obtain the desired analysis predictions. The analysis starts by defining the boundary layer edge properties from the flow field and ACE expansion analyses and concludes with the definition of the thermal performance parameters, namely, surface recession and in-depth temperature distributions. This latter information is required as input to the structural analysis which is discussed in Section 5.

#### 4.2 NOZZLE ENVIRONMENT

The nozzle environment which consists of the high speed particle laden propellant combustion product provides the driving force for the chemical and/or mechanical surface recession and the rise in the in-depth temperatures. Before a two-dimensional thermochemical analysis can be performed, this nozzle environment must be quantified in terms of the motor ballistics and the propellant constituents (Section 4.2.1), the boundary layer edge properties (Section 4.2.2), and the energy transfer mechanisms at the nozzle surface (Section 4.2.3).

#### 4.2.1 Motor Ballistics and Propellant

The two possible chamber pressure histories which were assumed are shown in Figure 4-2. The thermochemical analysis was performed for the chamber pressure which had a nominal pressure of 1000 psi for a nominal burn time of 60 seconds. Thermal analysis results are reported at motor burn times of 1.5, 10, 30, and 60 seconds. These results for motor burn times of 1.5, 30 and 60 seconds were used as input to the structural analysis. The 1.5 and 30 second results provide a slightly conservative answer for the motor with the 30 second burn time.

The propellant considered in the analysis was a 21 percent aluminized PVC composite with a flame temperature of 5700°F at 1000 psia. The constituents of this propellant are shown below.

	<u>Percent by Mass</u>
Ammonium Perchlorate	59.9
Aluminum	21.1
Polyvinylchloride	8.19
DOA	10.56

#### 4.2.2 Boundary Layer Edge Environment

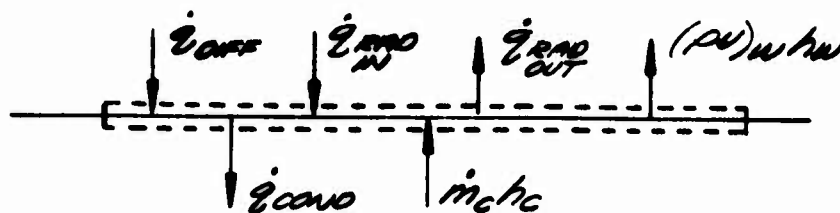
The boundary layer edge environment is defined by performing an expansion analysis using the ACE computer code with the propellant constituents as input data. The results of this analysis are shown in Figures 4-3 and 4-4 as a function of the non-dimensional flow parameter  $\tilde{p}u$ . This flow parameter is the ratio of the local mass flux divided by the mass flux at the sonic point (nozzle throat).

The boundary layer edge properties presented in Figures 4-3 and 4-4 are related to a particular nozzle location through a flow field analysis. For a submerged nozzle, the one-dimensional assumption is not applicable for this flow field analysis but a sophisticated two-dimensional analysis was outside the scope of the present study. In Reference 25 a detailed flow field analysis was performed for a submerged nozzle which was similar to the one shown in Figure 3-1. Because of this similarity, the flow field results for the nozzle geometry presented in Figure 3-1 were approximated from those presented in Reference 25. These approximate results are presented in Figure 4-5.

#### 4.2.3 Wall Surface Energy Balance

For the problem considered here, the ASTHMA computer code performs the energy balance for a control volume fixed to the receding surface as indicated

in the sketch below



The energy fluxes leaving the control volume include conduction into the material, radiation away from the surface, and gross blowing at the surface. Energy inputs to the control volume include radiation from the combustion products enthalpy flux due to the convection of material to the surface associated with surface recession and all the diffusion energy fluxes from the gas phase boundary layer. For a film coefficient model, the energy balance becomes for unequal mass diffusion coefficients

$$\rho_e u_e C_H (H_r - h_w)_{\text{edge gas}} + \rho_e u_e C_M \left[ \sum_i (z_{ie}^* - z_{iw}^*) h_i^{T_w} + B_c' h_c - B_c' h_w \right] + \alpha_w \dot{q}_{\text{inc rad}} - F_{scw} T_w^4 - \dot{q}_{\text{cond}} = 0 \quad (4-1)$$

The convection and mass diffusion coefficients required by the above equation are defined in Section 4.2.3.1, and the radiation terms are defined in Section 4.2.3.2. The chemical potential and enthalpy terms are generated using the ACE computer code, and this information will not be presented here. However, the thermochemical maps for the surface materials are presented in Section 4.2.3.3.

#### 4.2.3.1 Convective Heat Transfer Coefficients

The convective heat transfer coefficients were calculated using the Aerotherm Real Gas Energy Integral Boundary Layer (ARGEIBL) program. This program has been used previously to perform boundary layer analysis of the type presented here (i.e., References 5, 20, and 25). The primary inputs for this program are

- The real gas (with the  $\text{Al}_2\text{O}_3$  particles removed) Mollier tables for the propellant.
- The boundary layer edge properties as a function of  $pu$ .
- The  $pu$  ratio as a function of nozzle location.

The first two items of input data were generated using the Aerotherm Chemical Equilibrium (ACE) program and the third item was obtained from Figure 4-5.

One other item to note is that the initiation of the boundary layer ( $\lambda = 0$ ) is defined in Figure 3-1 and is on the backface of the submerged nozzle. The convective heat transfer coefficient results from the ARGEIBL program are presented in Figure 4-6 for two wall temperatures. Based on previous analyses (References 5, 20, and 25) these coefficients were multiplied by 0.75 prior to using them in the two-dimensional heat conduction analysis. The mass transfer coefficients were generated from these convective heat transfer coefficients using the relation

$$\rho_e u_e C_M = \rho_e u_e C_H Le^{2/3} \quad (4-2)$$

where  $\rho_e u_e C_M$  - mass transfer coefficient

$\rho_e u_e C_H$  - heat transfer coefficient

$Le$  - Lewis number

#### 4.2.3.2 Radiation Heating

This section is concerned with the two radiation terms in Equation (4-1). The radiant flux absorbed by the surface ( $\dot{q}_{rad \text{ in}}$ ) is defined as the incident radiation multiplied by the absorptance of the wall. The radiant flux emitted by the surface ( $\dot{q}_{rad \text{ out}}$ ) is defined as that emitted by a black body multiplied by an emittance factor and by a view factor. Therefore the net radiation to the surface ( $\dot{q}_{net \text{ rad}}$ ) is defined by

$$\dot{q}_{net \text{ rad}} = \alpha_w \dot{q}_{inc \text{ rad}} - F \epsilon_w \sigma T_w^4$$

where

$\alpha_w, \epsilon_w$  - absorptivity and emissivity, respectively, of wall material  
( $\alpha_w$  and  $\epsilon_w$  are equal by Kirchoff's Law for a gray body)

$\sigma$  - Stefan-Boltzmann constant

$T_w$  - wall temperature

$F$  - view factor

In order to model the radiation transport between a particle laden stream and the nozzle surface, it was assumed that the stream was optically thick and that the particles and wall exchange radiant energy as if they were two parallel plates. In this way multiple reflections between the wall and stream were taken into account. In addition, it was assumed that both the stream and wall behave as gray bodies and that they emit and reflect radiant energy diffusely. Based on the above assumption, the net radiant heat flux relation is given as

$$\dot{q}_{\text{net rad}} = \epsilon_{\text{eff}} (\sigma T_s^4 - \sigma T_w^4) \quad (4-4)$$

where

$$\epsilon_{\text{eff}} \text{ (effective emissivity)} = \left( \frac{1}{\frac{1}{\epsilon_w} + \frac{1}{\epsilon_s} - 1} \right) \quad (4-5)$$

$\epsilon_s$  - particle laden stream emissivity

$T_s$  - local stream static temperature

To define the net radiation heat flux using Equation (4-4) the local static stream temperature and the effective emissivity had to be evaluated. The stream temperature was obtained from the isentropic expansion data presented previously in Figures 4-3 and 4-4. The effective emissivity was evaluated from Equation (4-5) using a value of 0.9 for the wall emissivity and using the following relationship (Reference 5) for the emissivity of the particle laden combustion products.

$$\epsilon_s = 1 - \exp \left( -C \frac{n}{16} \rho D \right) \quad (4-6)$$

where

$C$  - experimentally determined constant (0.808 for the propellant being considered in this analysis)

$n$  - percentage of aluminum loading

$\rho$  - local density of propellant combustion species (lb/ft<sup>3</sup>)

$D$  - local beam length, usually taken as the diameter (in.)

#### 4.2.3.3 Surface Thermochemistry Maps

In order to perform a transient two-dimensional thermal analysis of the nozzle throat assembly, surface thermochemistry maps are required for the Speer 8882 and Speer 9139 bulk graphites, the PG coating, and the MX 4926 carbon cloth phenolic. The surface thermochemical response of the first three materials is controlled by the finite (as opposed to equilibrium) reaction rates of the surface carbon atoms with the H<sub>2</sub>O, CO<sub>2</sub>, and H<sub>2</sub> components of the solid propellant. The kinetically controlled reaction rate models developed under Air Force Contract F04611-69-C-0081 (Reference 24) were utilized to compute the surface response of these graphite materials, and solutions were performed using the ACE code.

The kinetic response model incorporates a Langmuir type surface reaction inhibition expression into an Arrhenius temperature dependent rate relation. The rate expression and reaction kinetic rate constants are given in Table 4-1. The partial pressure quantities were evaluated in the ACE code using the film coefficient, multicomponent unequal diffusion boundary layer model. The area ratio, local static pressure and temperature, and the local heat and mass transfer coefficient value for which the kinetically controlled response calculations were performed are given in Table 4-2. The non-dimensional kinetically controlled surface thermochemistry maps are shown in Figure 4-7. For comparison, the non-dimensional diffusion controlled map is also shown in this figure.

The steady state surface thermochemistry map for the MX4926 carbon cloth phenolic is shown in Figure 4-8. For the particular environment which it is subjected to, the steady state assumption is probably reasonable for this material. However, the primary reason for this assumption is that the two-dimensional computer code does not account for material degradation, and thus, it can not account for variable pyrolysis gas rates.

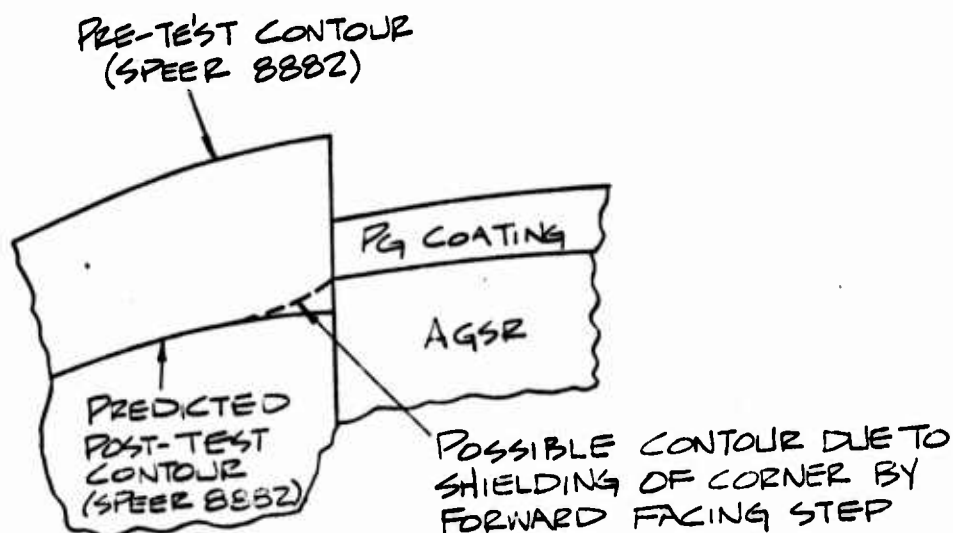
#### 4.3 NOZZLE WALL MATERIAL THERMOCHEMICAL PERFORMANCE

A two-dimensional thermal analysis including the effects of surface ablation was performed using the Axi-Symmetric Transient Heating and Material Ablation (ASTHMA) program (Reference 21). An analysis was performed using two nodal layouts: the nozzle insert nodal grid (Figure 4-9) and the nozzle assembly nodal grid (Figure 4-10). These grids represent the two possible extremes with 1) the validity of the nozzle insert nodal grid dependent upon the assumption of infinite thermal resistance between the insert and the adjacent materials, and 2) the validity of the nozzle assembly grid dependent upon the assumption of zero thermal resistance between the insert and the adjacent materials. Because of the fabrication procedure, tolerances, and bonding materials, the latter assumption is believed to be more realistic.

The surface temperatures, surface recession rates, and net surface recessions are presented in Figures 4-11 through 4-13 for the nozzle insert grid and for the entire 60 second motor firing and in Figures 4-14 through 4-16 for the nozzle assembly grid and for the first 30 seconds of the motor firing. The results presented in these figures were based on the original "c" direction thermal conductivity values for pyrolytic graphite. The PG results presented in Figure 4-11 through 4-16 which are comparable show that the predicted performance of the PG coating is independent of the nodal grid.

The predicted performance presented in Figures 4-14 through 4-16 for both the downstream bulk graphite and the MX4926 carbon cloth phenolic materials indicate no design problem. However, the predicted performance of the upstream

Speer 8882 bulk graphite material is marginal for a 60 second firing. The problem is that the predicted surface recession for this material would be approximately 320 mils for a 60 second firing. This amount is larger than the combined thickness of the Speer 8882 lip (200 mils) and the PG coating (60 mils). A comparison of this thickness with the predicted recession means that the interface between the PG coating and the AGSR substrate would be exposed. Because this interface would be partially shielded as shown by the sketch below, the actual recession at the interface would be less than the predicted value of 320 mils. However, this shielding may not be sufficient to prevent undercutting of the PG coating.



Isotherm temperature contours for motor firing times of 1.5, 5.0, 10.0, 30.0, and 60.0 and for the nozzle insert grid are presented in Figures 4-17 through 4-21. These figures show the gradual progression of the isotherms into the AGSR as the motor firing continues. For example, at  $t = 1.5$  seconds, the interface of the PG coating and the AGSR substrate is approximately  $1000^{\circ}\text{R}$ . At  $t = 10$  seconds, this interface has increased to  $2000^{\circ}\text{R}$  and the majority of the substrate is above  $1000^{\circ}\text{R}$ . At  $t = 30$  seconds, the interface is approximately  $3000^{\circ}\text{R}$ , and at  $t = 60$  seconds, it is approximately  $4000^{\circ}\text{R}$ . In addition, these figures show that the upstream portion of the substrate is at higher temperatures than either the throat or downstream sections. This is due to the substrate being relatively thinner at the upstream section.

Isotherm temperature contours for motor firing times of 1.5, 5.0, 10.0 and 30.0 seconds and for the nozzle assembly grid are presented in Figures 4-22 through 4-25. For the nozzle insert, the primary difference between the temperature contours presented in these figures and the corresponding ones presented previously is the progression towards the throat of the upstream and downstream

portions of the isotherms. This progression is caused by thermal energy being transmitted through the upstream and downstream bulk graphites and into the AGSR substrate and is a result of the thermal conductivity of the bulk graphites being much higher than for the "c" direction of the PG coating. The differences in the thermal profiles at the entrance, throat, and exit of the nozzle insert for the two nodal grids are illustrated in Figure 4-26. A comparison of these profiles shows the following:

- For the entrance and exit sections of the AGSR the predicted temperatures for  $t = 30$  seconds using the nozzle assembly grid are approximately the same as those predicted for  $t = 60$  seconds using the nozzle insert grid
- At 30 seconds, the predicted temperatures at the throat section are approximately the same for both nodal grids.

The differences between the nozzle insert temperatures for the two nodal grids do not significantly affect the thermal performance of the throat. However, these temperature differences might have a significant effect on the structural performance of the insert, and this effect will be investigated in the structural analysis which is presented in Section 5.

A two-dimensional analysis was performed using the revised "c" direction PG thermal conductivity properties and the nozzle insert nodal grid. By comparing the results of this analysis, which are presented in Figures 4-27 through 4-31, with those presented in Figures 4-17 through 4-21, one notes that the revised PG properties cause a marked increase in the thermal penetration of the AGSR substrate. This increase is best seen by comparing the location of the 3000°R and 4000°R isotherms presented in Figures 4-21 and 4-31. The primary reason for performing the analysis using the revised PG properties was to show the effect that the "c" direction PG thermal conductivity has on the AGSR substrate temperatures.



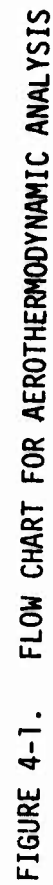
Table 4-1

KINETICALLY CONTROLLED REACTION RATE EXPRESSIONS USED FOR PG LAYER  
AND SPEER BULK GRAPHITE SURFACE THERMOCHEMISTRY SOLUTIONS<sup>a</sup>

Material	Pre-Exponent Factors (units to give $X_{C^*}$ below)		Activation Energies (cal/mole)	
	$B_1$	$B_2$	$E_1$	$E_2$
Layer PG	12.5	0.77	46,000	55,500
Edge PG <sup>b</sup>	$1.65 \times 10^4$	$4.12 \times 10^6$	65,500	129,500
ATJ (Bulk) Graphite	$1.98 \times 10^5$	$4.94 \times 10^7$		
<sup>a</sup> $X_{C^*} = \frac{B_1 \exp(-E_1/RT_w)}{(1 + P_{H_2O} + P_{H_2} + P_{CO_2} + P_{CO})(1 + 3P_{HCl})} \left[ \left( P_{H_2O} - \frac{P_{CO}P_{H_2}}{K_{H_2O}} \right) + \left( P_{CO_2} - \frac{P_{CO}^2}{K_{CO_2}} \right) \right]$ $+ \frac{B_2 \exp(-E_2/RT_w)}{(1 + P_{H_2O} + P_{CO_2} + P_{CO})} \left[ \left( P_{H_2} - \frac{P_{C_2H_2}}{K_{H_2}} \right) \right], \text{ moles of reaction/ft}^2\text{sec}$				
<sup>b</sup> No edge PG solutions were performed; constants included for completeness.				

TABLE 4-2  
SUMMARY OF EDGE CONDITIONS FOR SURFACE THERMOCHEMISTRY MAPS

Map No.	Material	Radius (in)	Edge Static Conditions		Nominal Transfer Coefficient	
			Pressure (atm)	Temperature (°R)	Heat <sup>a</sup> (lb/ft <sup>2</sup> sec)	Mass <sup>b</sup> (lb/ft <sup>2</sup> sec)
1	Speer 8882 Graphite	3.84	43.0	6000.	1.15	.726
2	PG Coating	3.75	42.4	5980.	1.12	.704
3	PG Coating	3.50	39.0	5810.	1.11	.699
4	PG Coating	3.60	29.0	5660.	1.04	.656
5	Speer 9139 Graphite	3.74	23.5	5480.	.990	.622
6	MX4926 Carbon Cloth Phenolic	3.98	19.0	5340.	.840	.529
a Heat transfer coefficient equals 0.75 times ARGEIBL result						
b Ratio of mass to heat coefficient equals to 0.630						



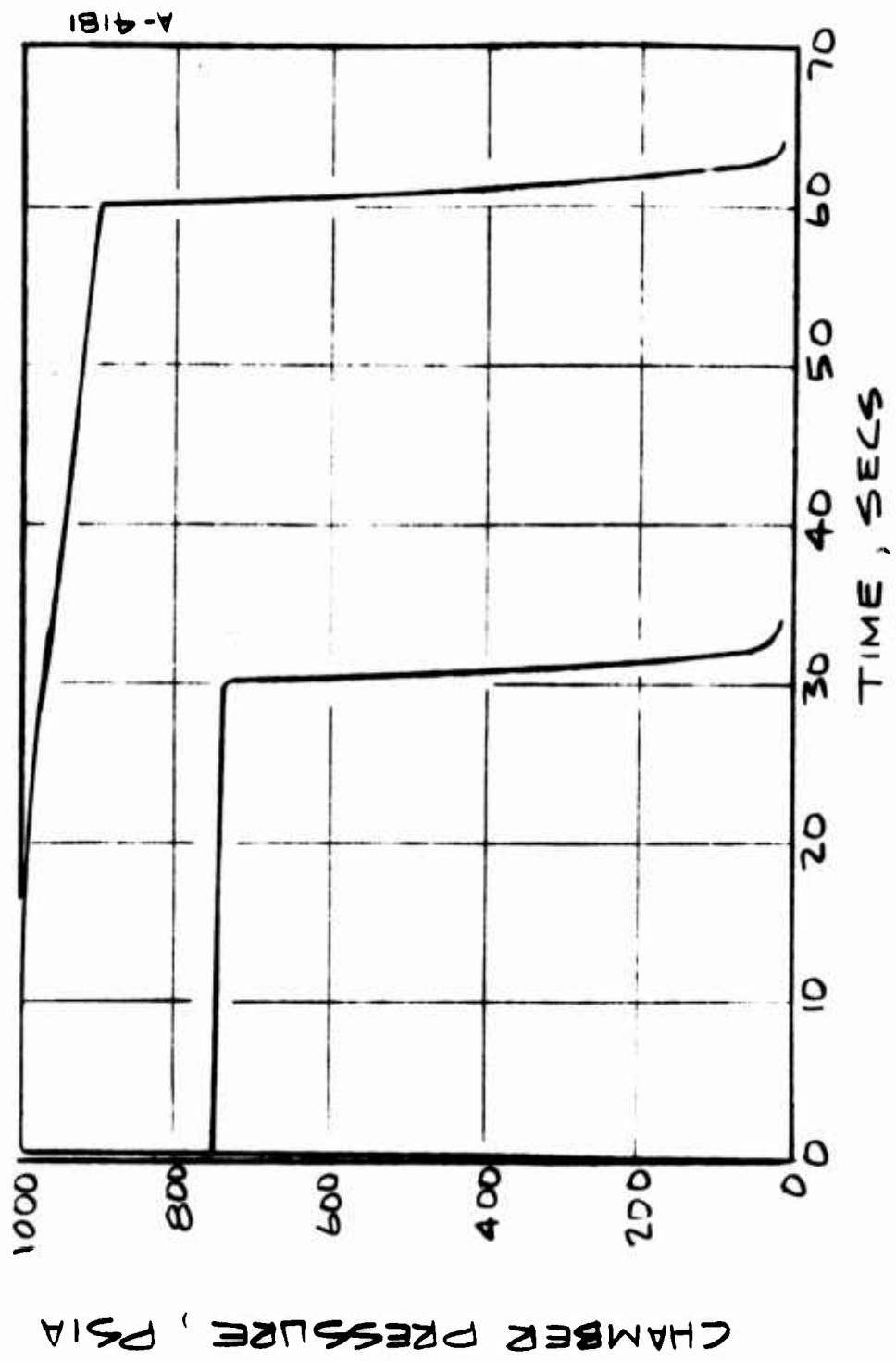


FIGURE 4-2 ASSUMED CHAMBER PRESSURE HISTORIES

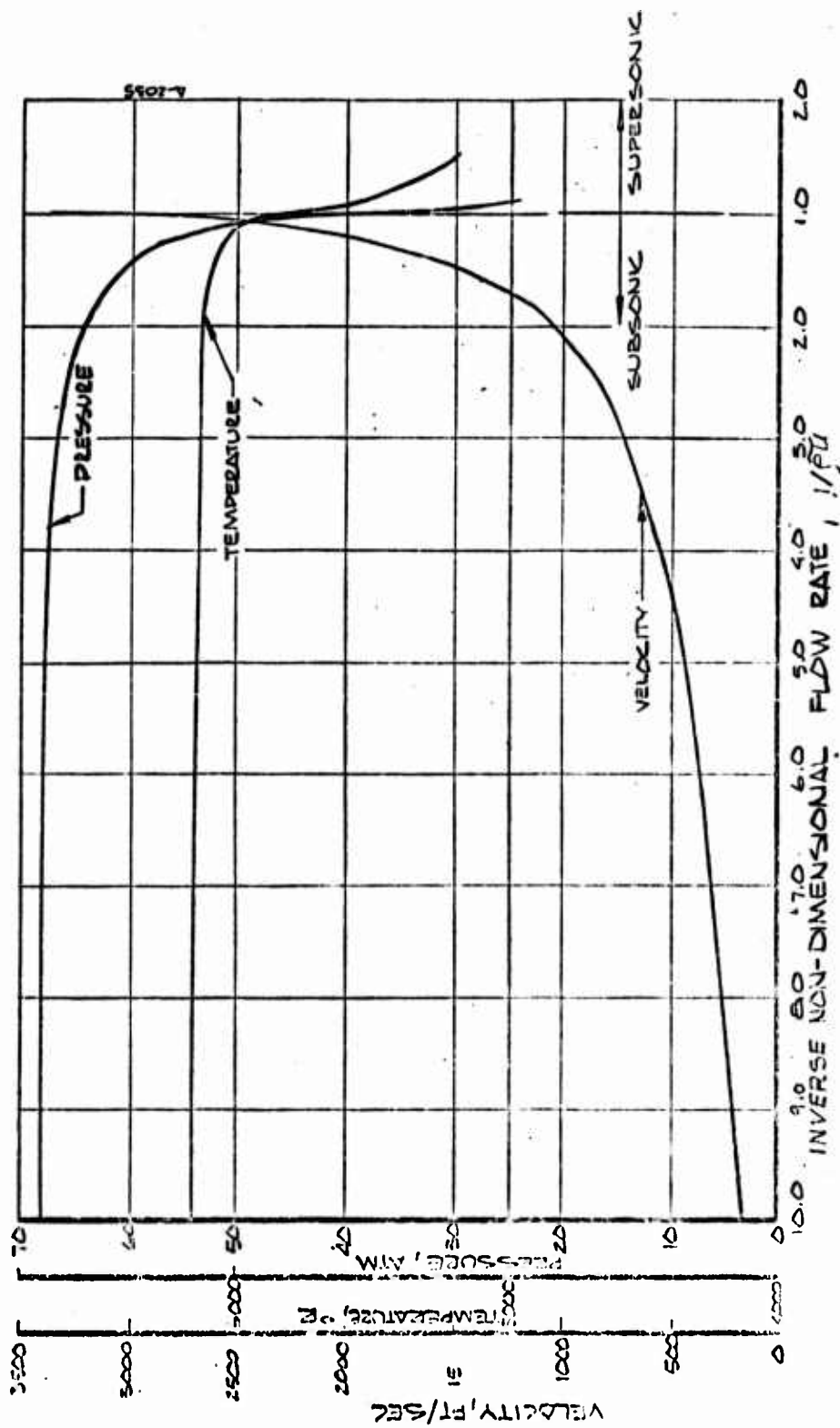


FIGURE 4-3. FLOW FIELD PARAMETERS FOR SUBSONIC AND TRANSONIC NON-DIMENSIONAL FLOW RATES - TEST WEIGHT NOZZLE

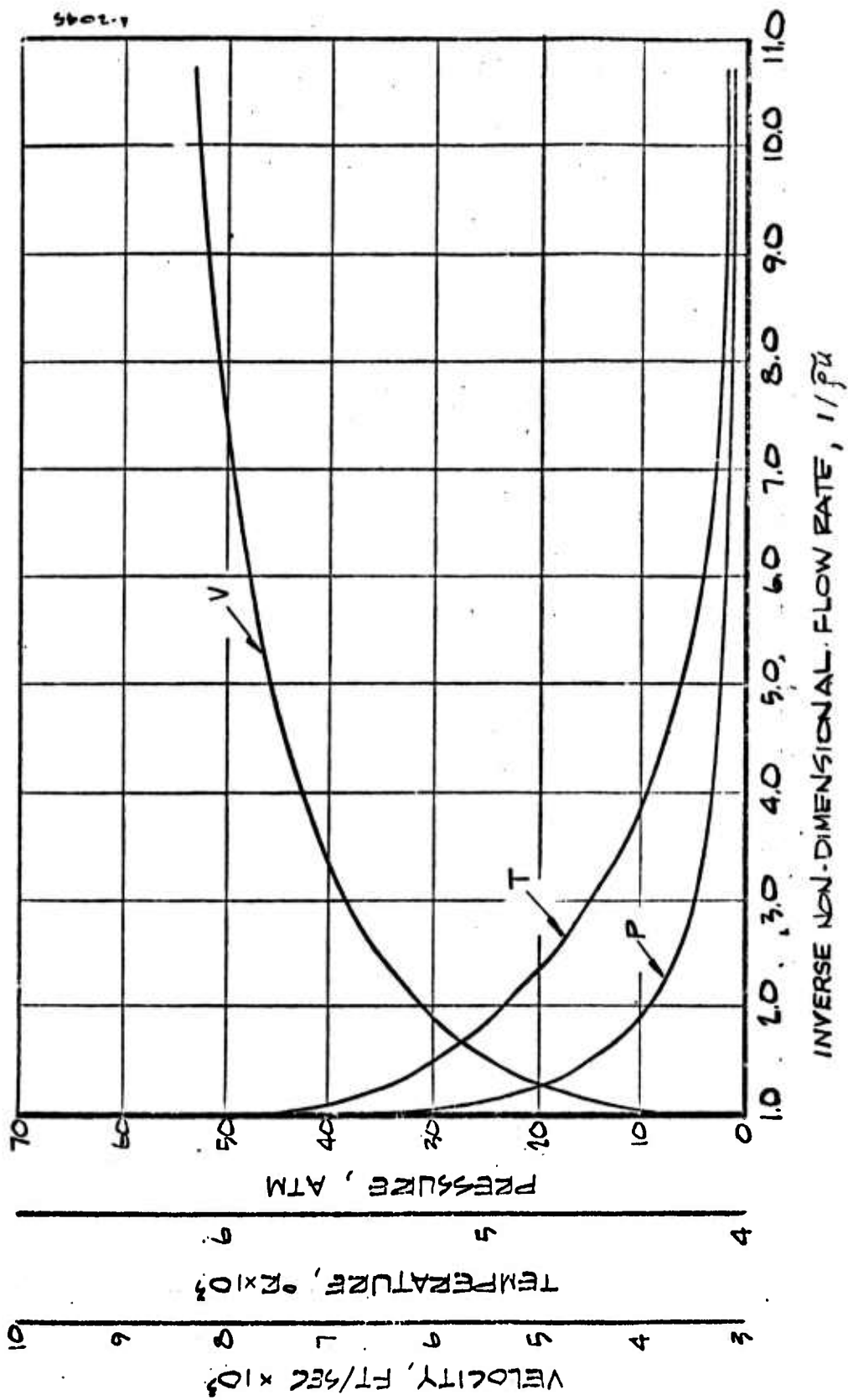


FIGURE 4-4 FLOW FIELD PARAMETERS FOR SUPERSONIC NON-DIMENSIONAL FLOW RATES = TEST WEIGHT NOZZLE -

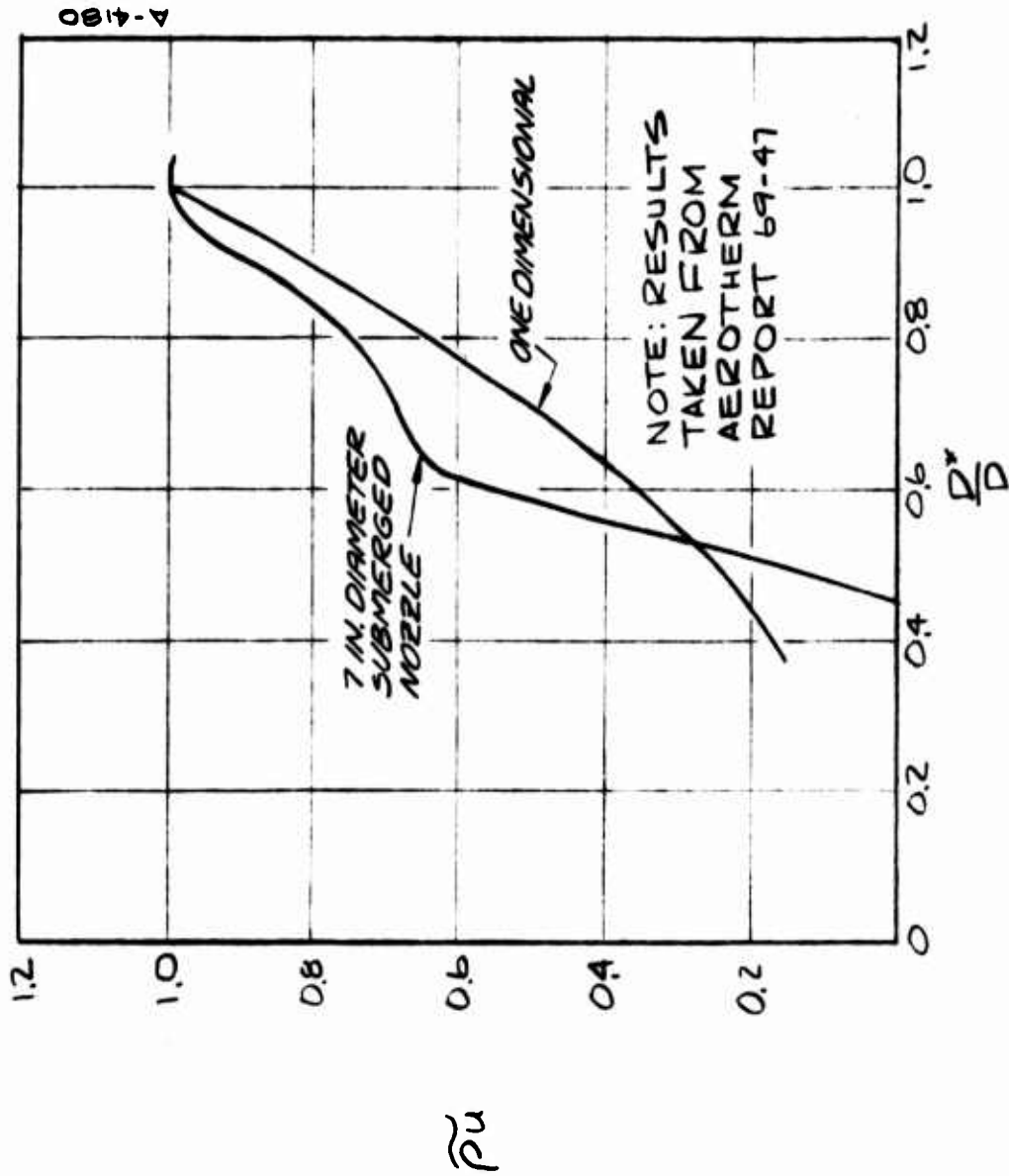


FIGURE 4-5 NONDIMENSIONAL MASS FLUX AS A FUNCTION OF  $\tilde{D}^*/D$

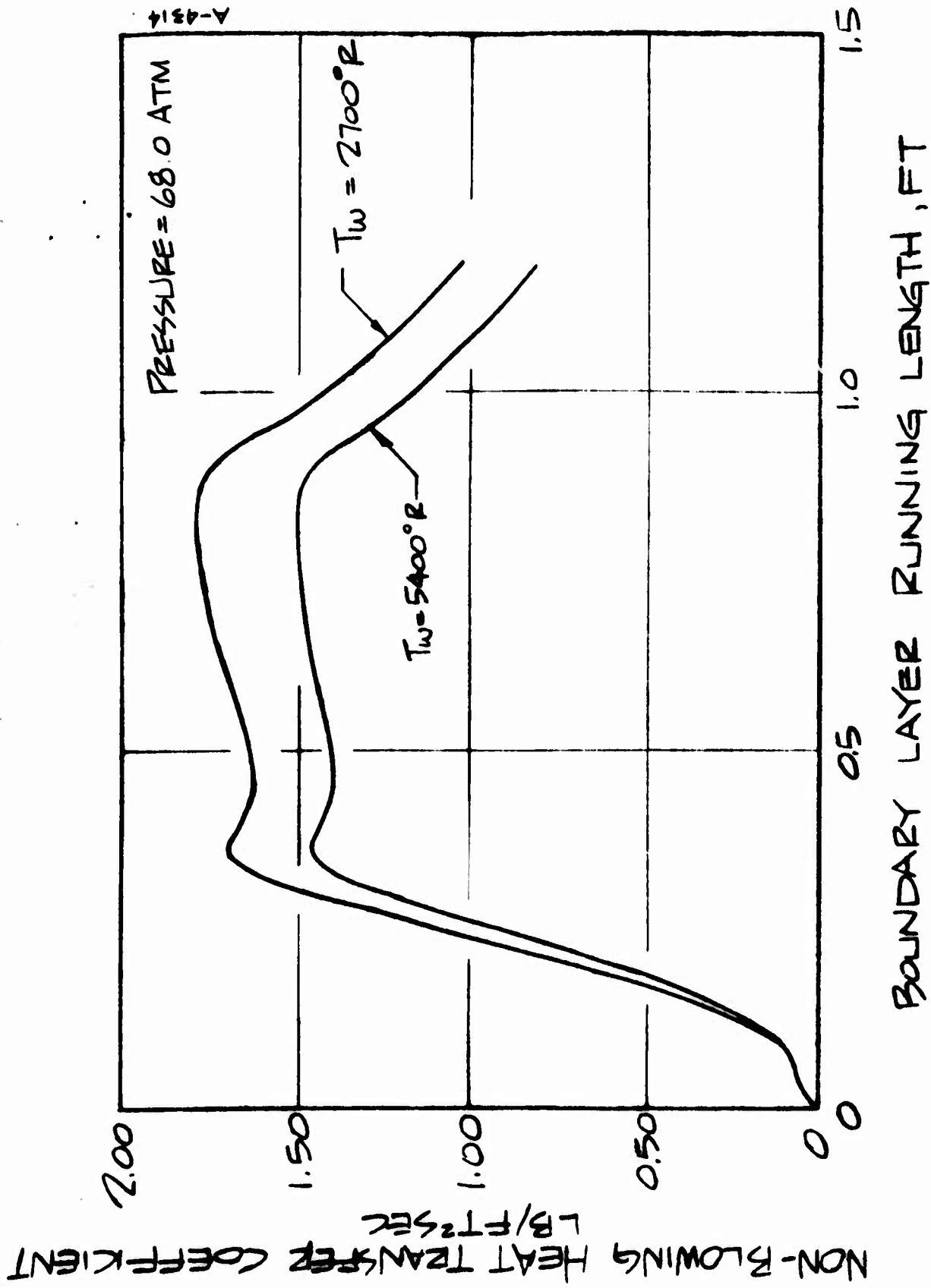


FIGURE 4-6 NON-BLOWING CONVECTIVE HEAT TRANSFER COEFFICIENTS FOR 7 INCH THROAT DIAMETER SUBMERGED NOZZLE



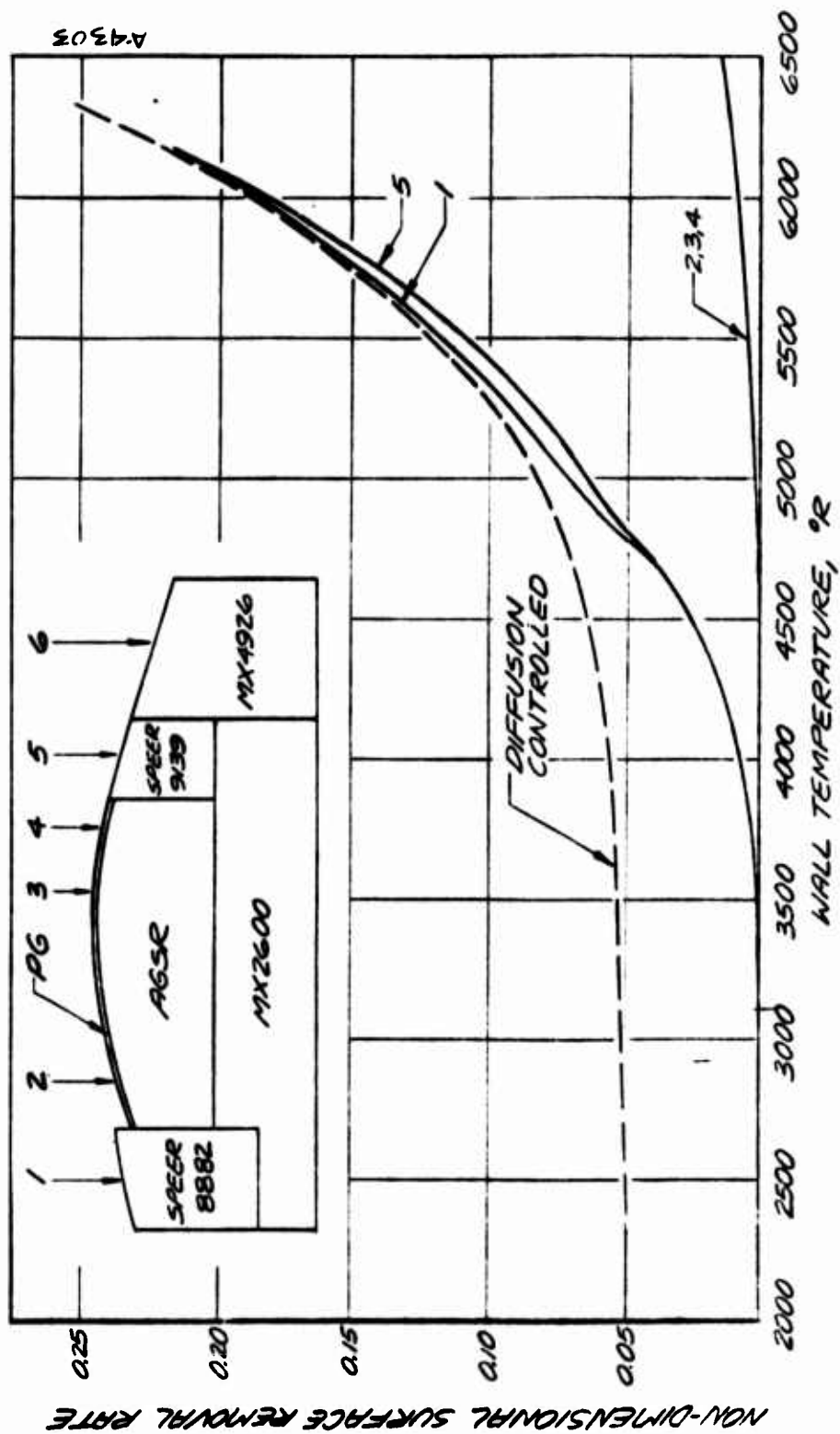


FIGURE 4-7 KINETICALLY CONTROLLED THERMOCHEMISTRY MAPS  
FOR BULK GRAPHITE AND PG COATING.

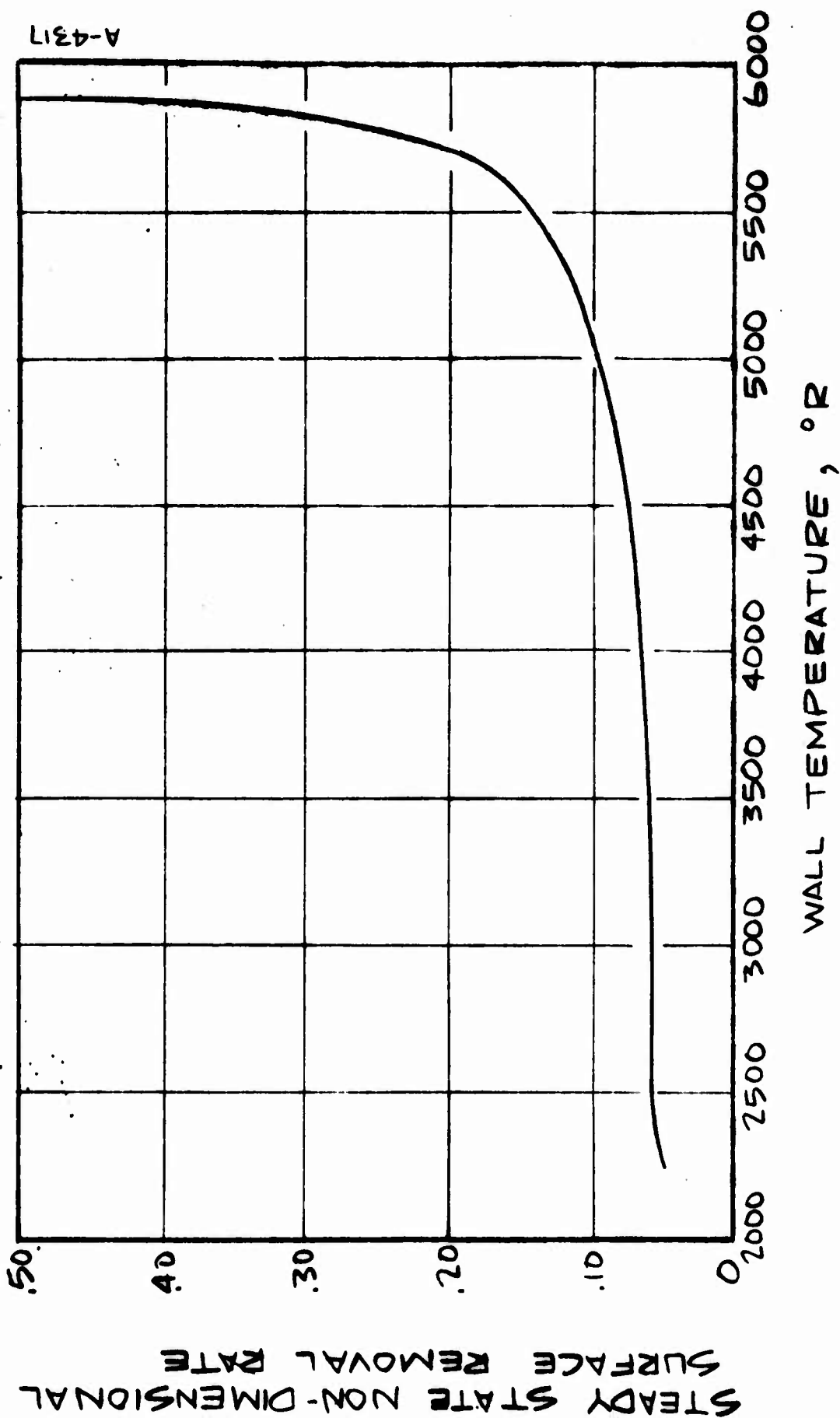


FIGURE 4-8 STEADY STATE DIFFUSION CONTROLLED SURFACE  
THERMOCHEMISTRY MAP FOR MX 4926 CARBON  
CLOTH PHENOLIC

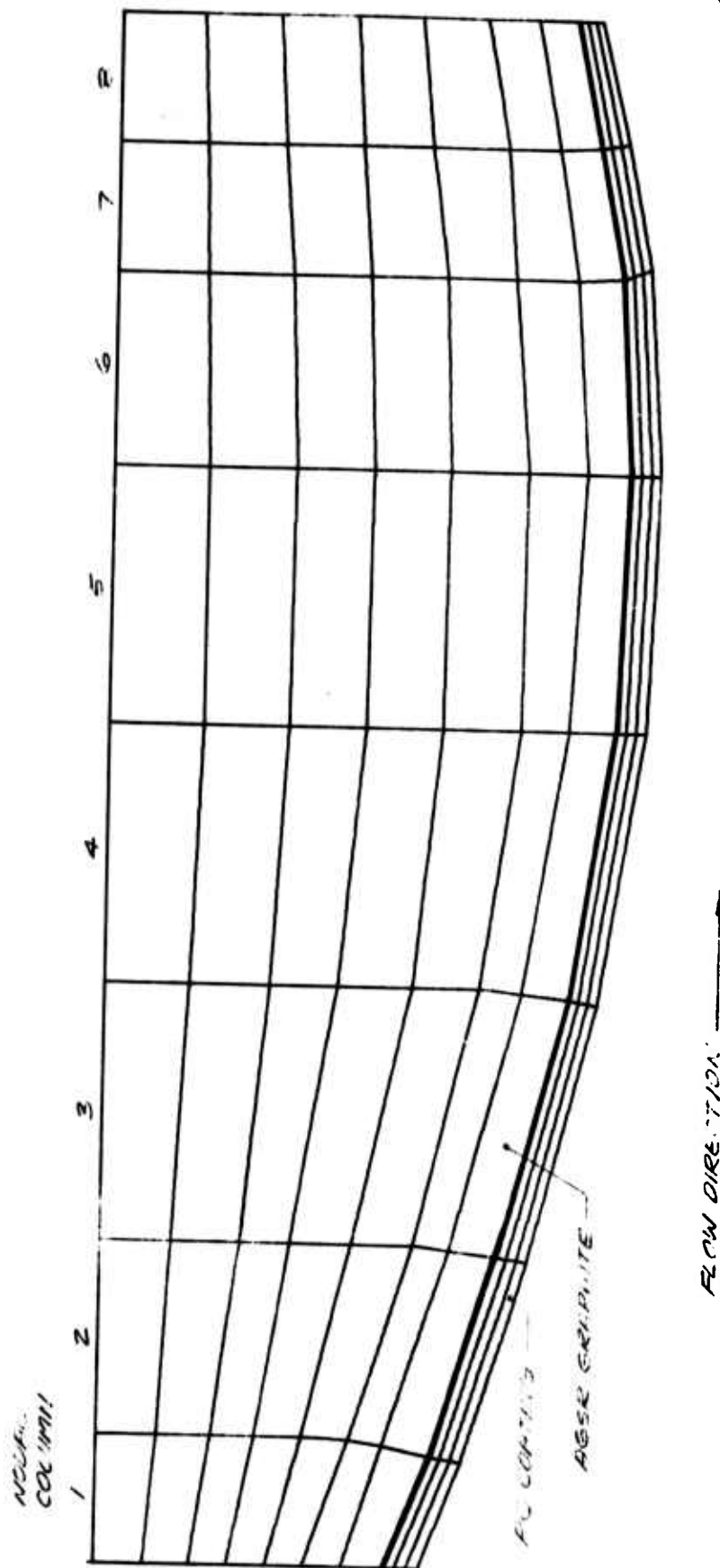


Figure 4-9. Nozzle Insert Nodal Grid

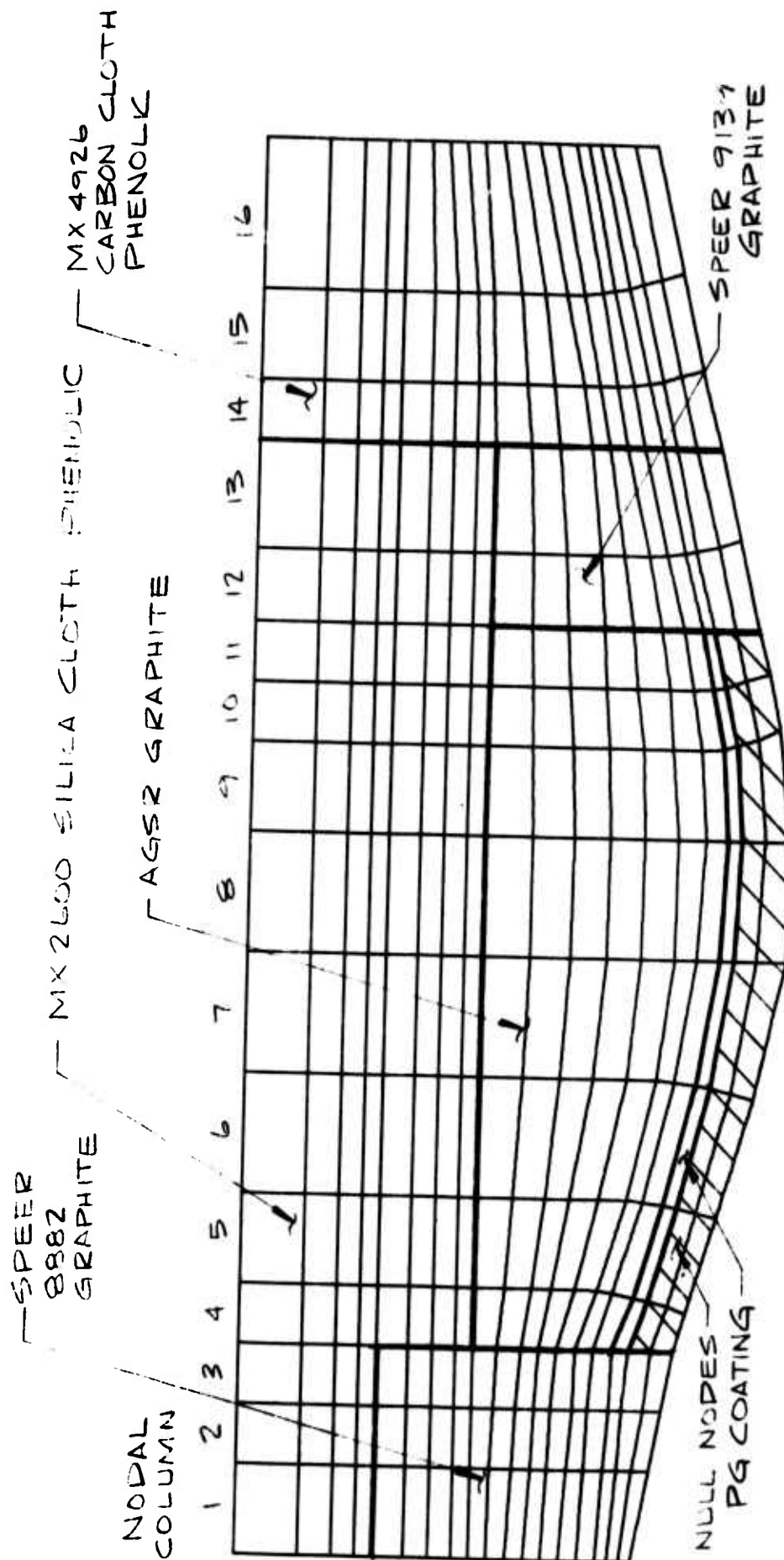


Figure 4-10. Nozzle Assembly Nodal Grid

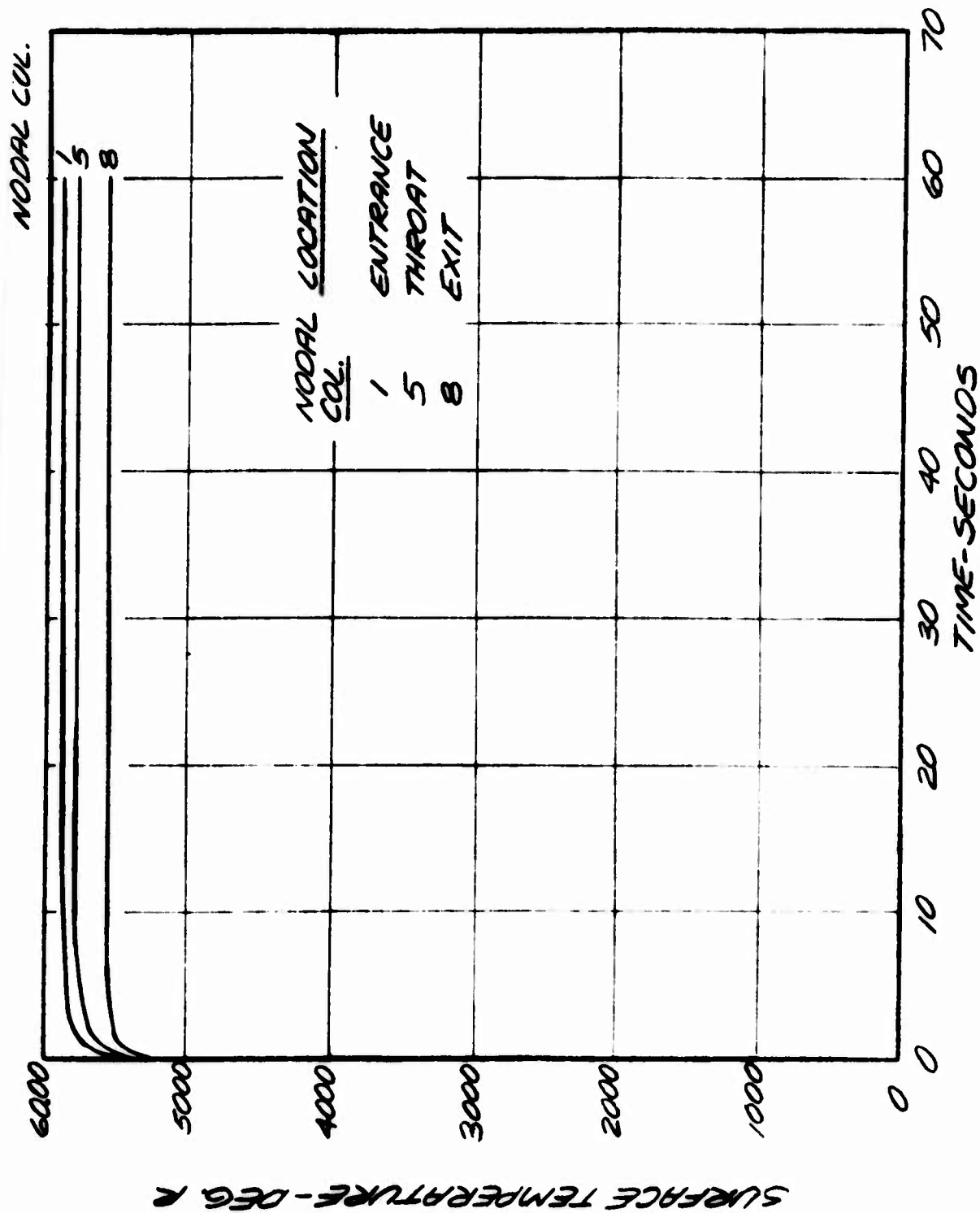


FIGURE 4-11 SURFACE TEMPERATURE HISTORIES FOR  
PG COATING USING NOZZLE INSERT  
NODAL GRID.

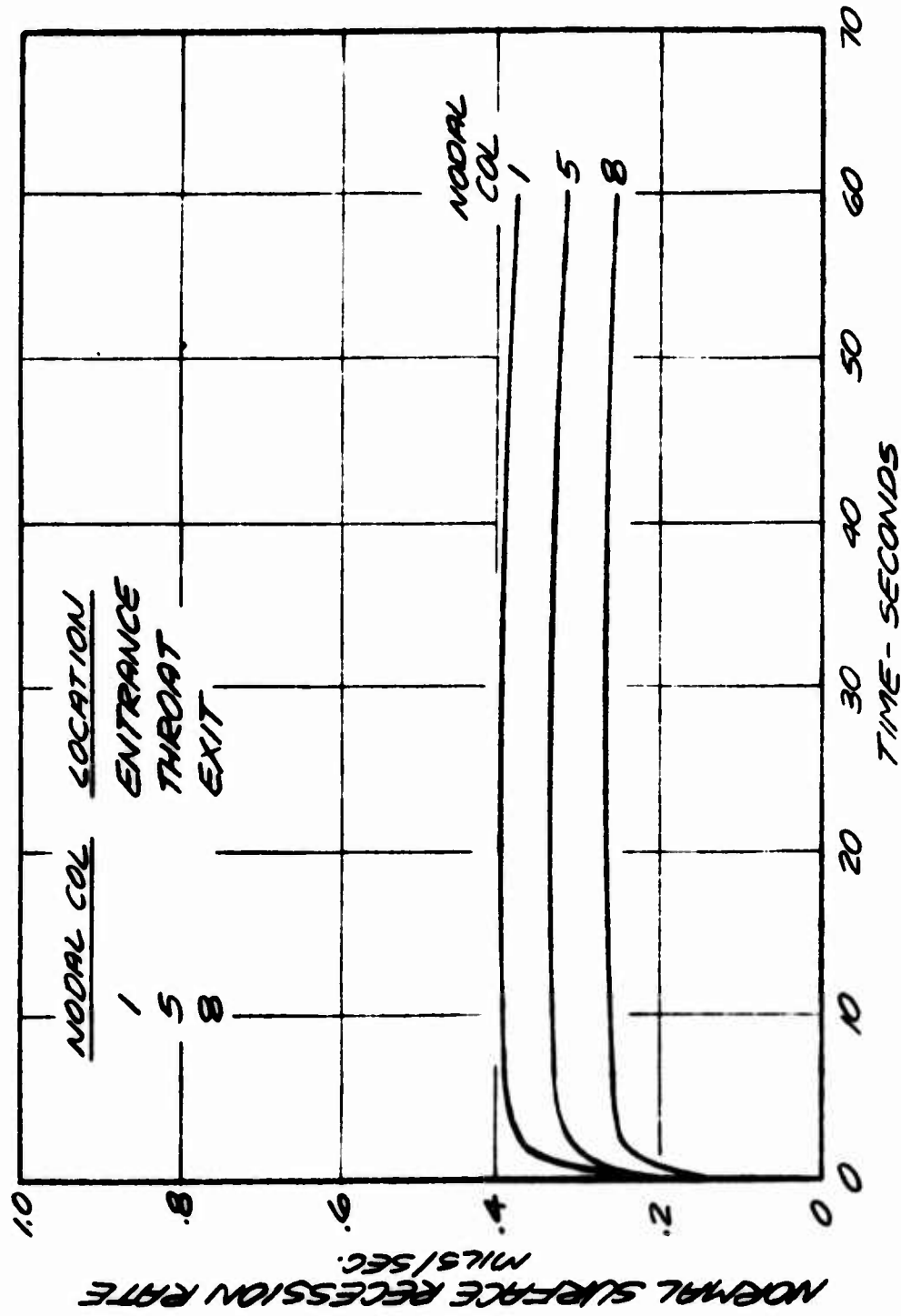


FIGURE 4.12 SURFACE RECESSION RATE HISTORIES FOR PG COATING USING NOZZLE INSERT NODAL GRID.

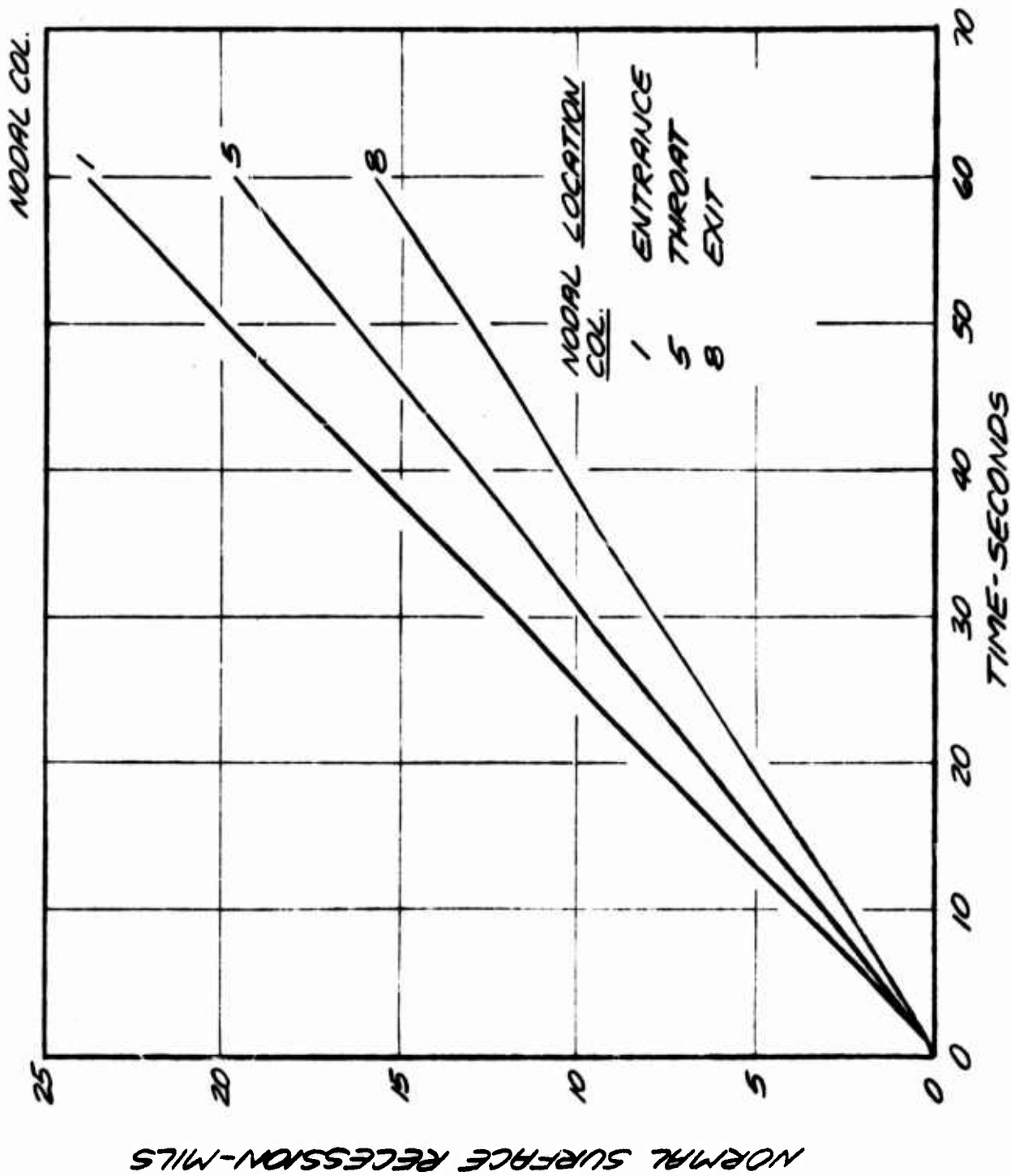


FIGURE 4-13 SURFACE RECESSION HISTORIES FOR PG COATING USING NOZZLE INSERT NODAL GRID.

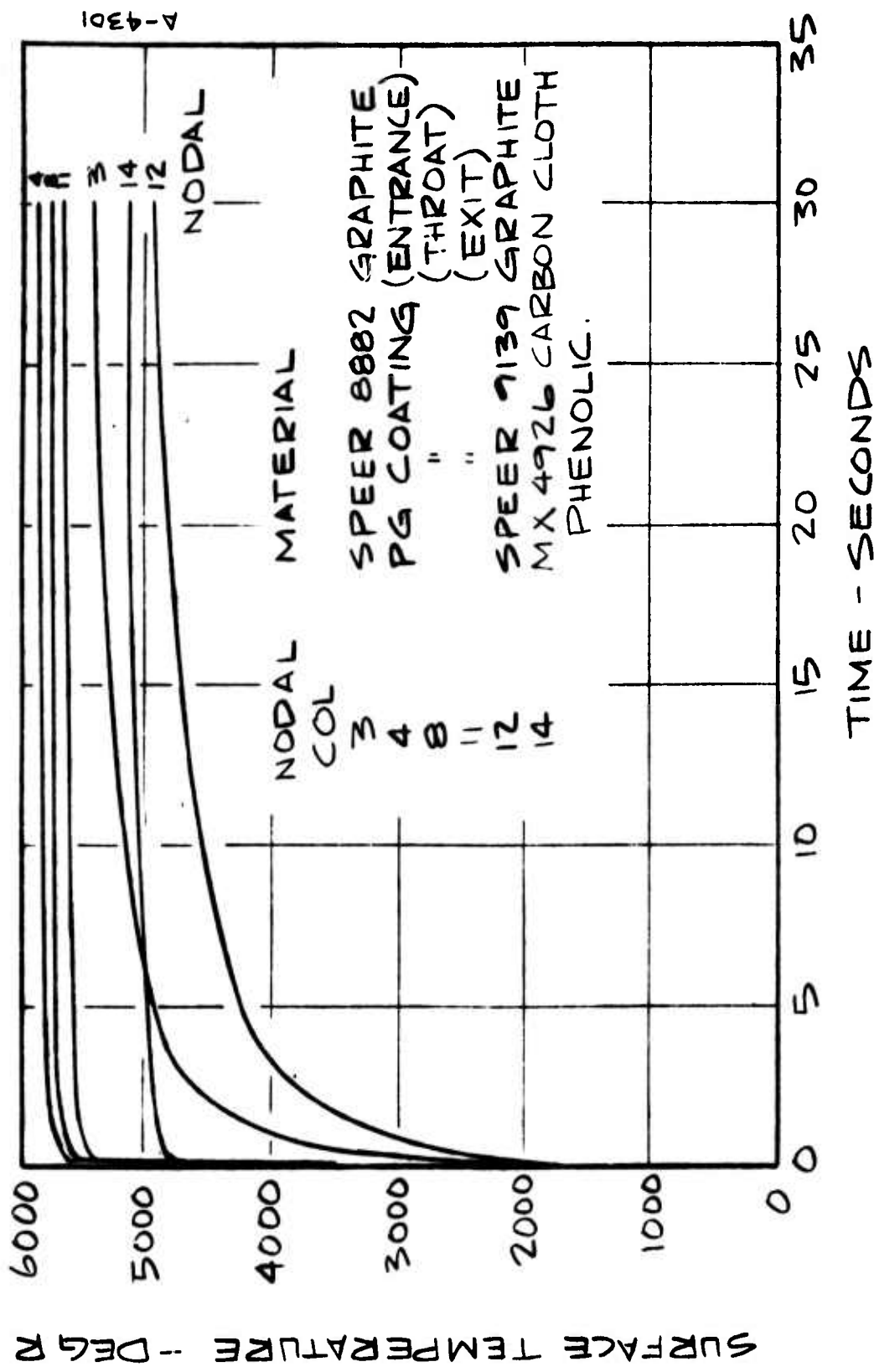


FIGURE 4/4 SURFACE TEMPERATURE HISTORIES FOR BULK GRAPHITE, PG COATING AND MX 4926 CARBON CLOTH PHENOLIC USING NOZZLE ASSEMBLY NODAL GRID



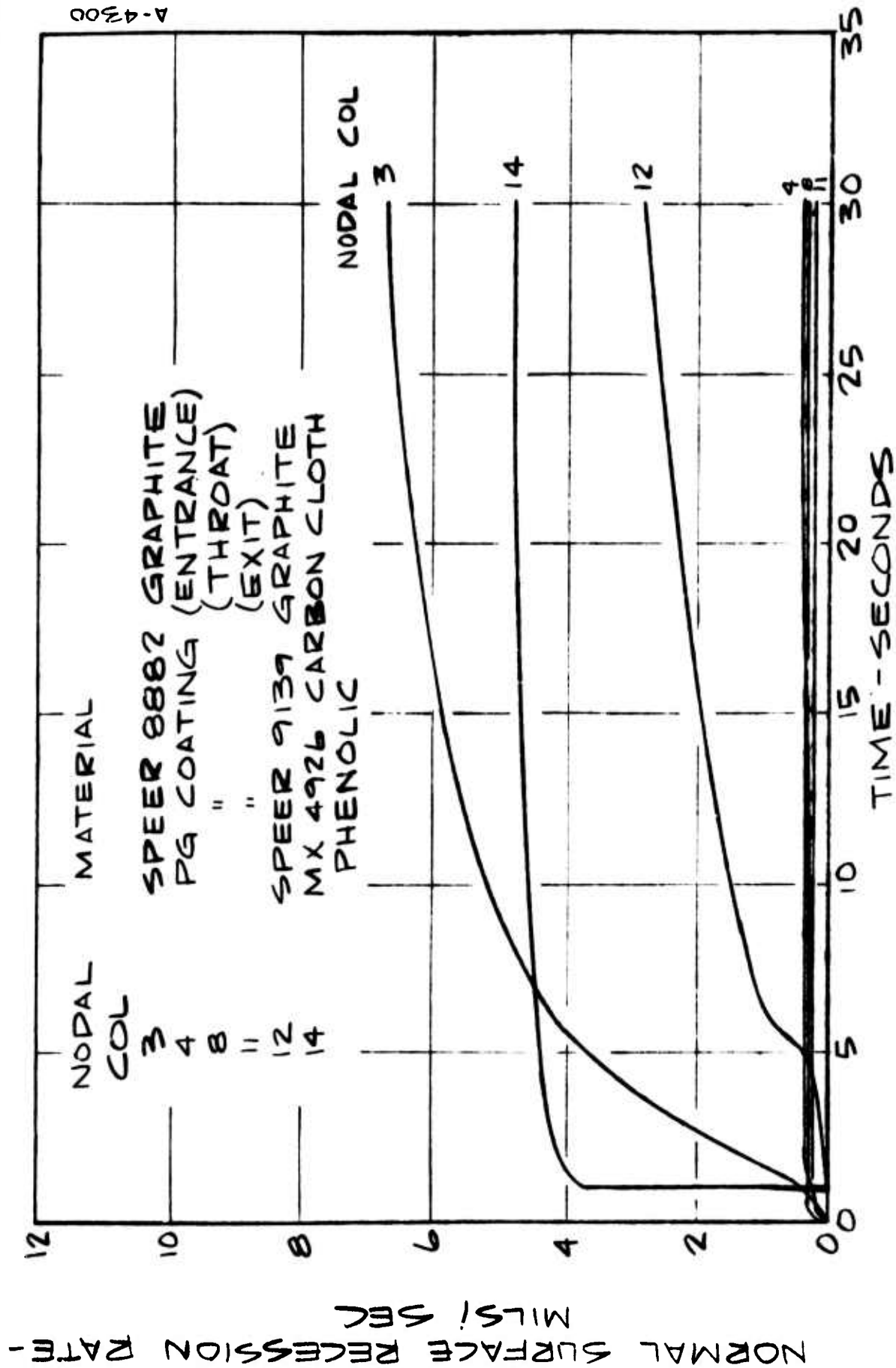
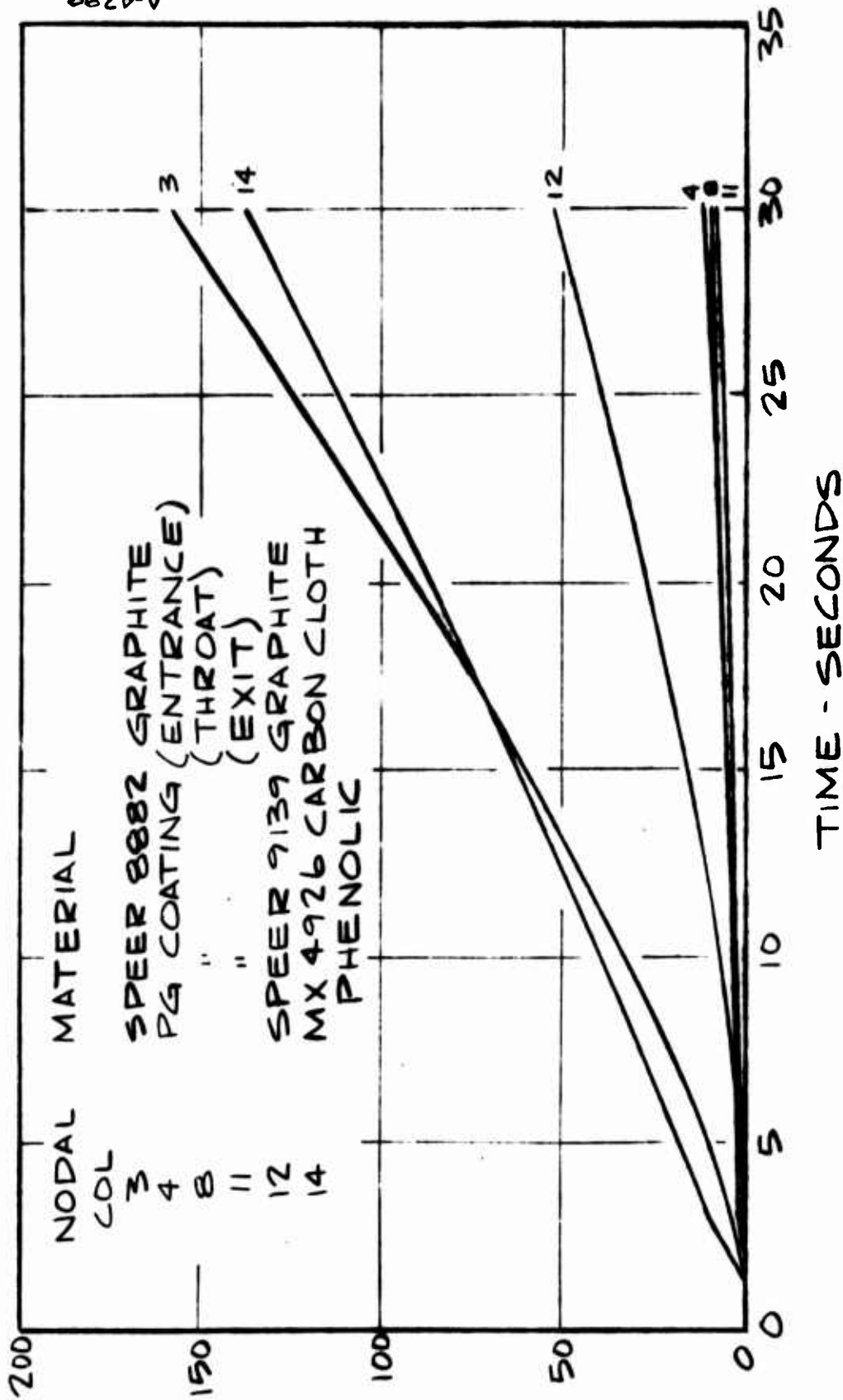


FIGURE 4-15 SURFACE RECESSION RATE HISTORIES FOR BULK GRAPHITE, PG COATING, AND MX4926 CARBON CLOTH PHENOLIC USING NOZZLE ASSEMBLY NODAL GRID.

NORMAL SURFACE RECESSON - MILS



A-4299

FIGURE 4-16 SURFACE RECESSON HISTORIES FOR BULK GRAPHITE, PG COATING, AND MX4926 CARBON CLOTH PHENOLIC USING NOZZLE ASSEMBLY NODAL GRID

# LEGEND

\* SURFACE  
 ◇ 5000 °R  
 × 4000 °R  
 + 3000 °R  
 ^ 2000 °R  
 ○ 1000 °R  
 □ 600 °R



Figure 4-17. Isotherm Temperature Profiles for Nozzle Insert  
 Nodal Grid -  $t = 1.5$  seconds

LEGEND

*	SURFACE
x	5000 °R
+	4000 °R
Δ	3000 °R
○	2000 °R
□	1000 °R

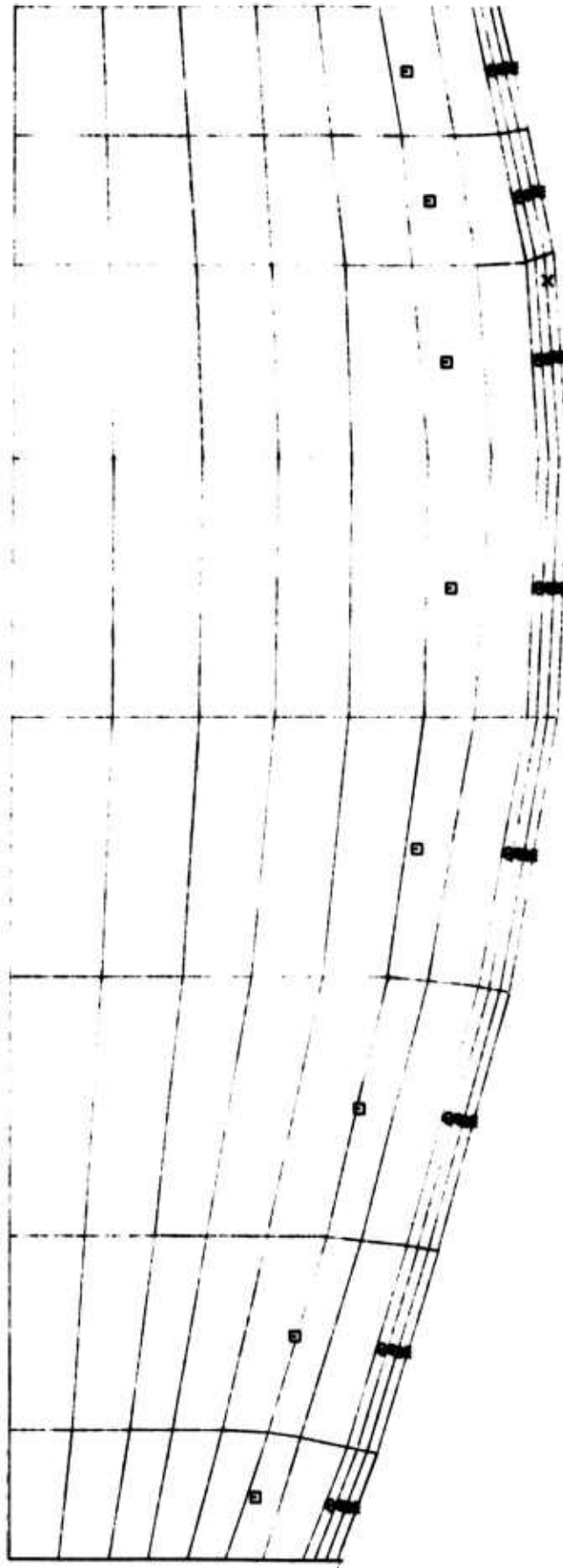


Figure 4-18. Isotherm Temperature Profiles for Nozzle Insert  
Nodal Grid -  $t = 5.0$  seconds

# LEGEND

- \* SURFACE
- x 5000 °R
- + 4000 °R
- Δ 3000 °R
- 2000 °R
- 1000 °R

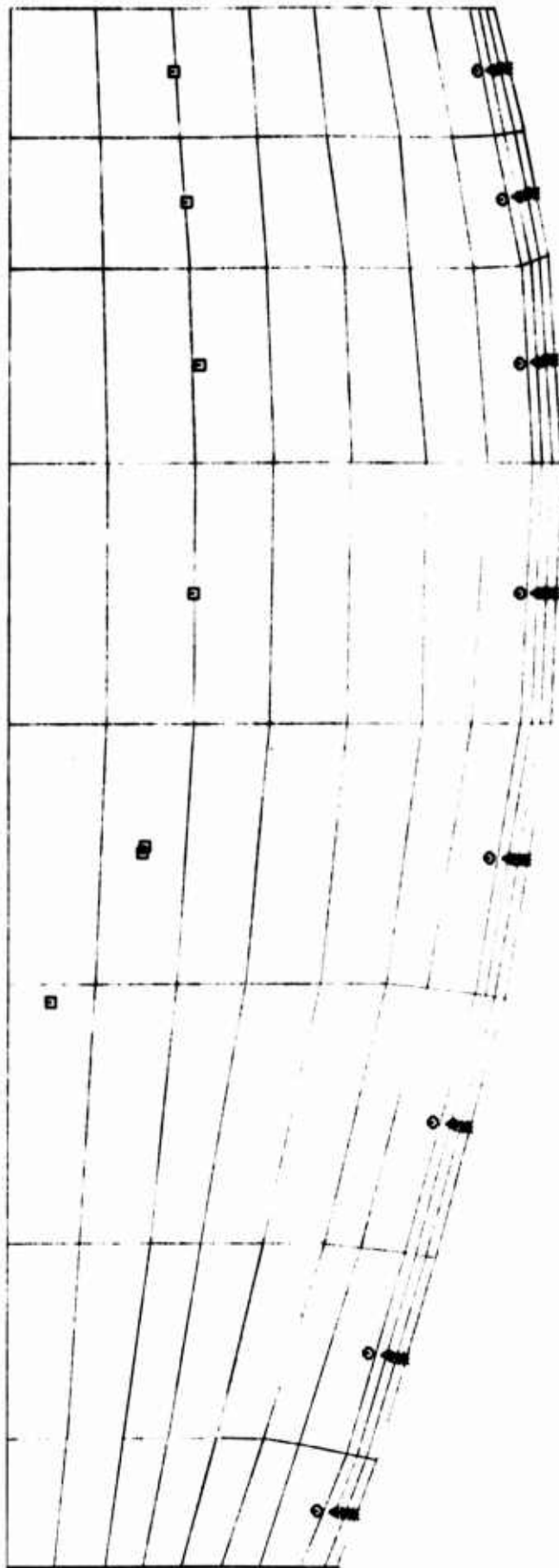


Figure 4-19. Isotherm Temperature Profiles for Nozzle Insert  
Nodal Grid -  $t = 10.0$

LEGEND

- \* SURFACE
- + 5000 °R
- △ 4000 °R
- 3000 °R
- 2000 °R

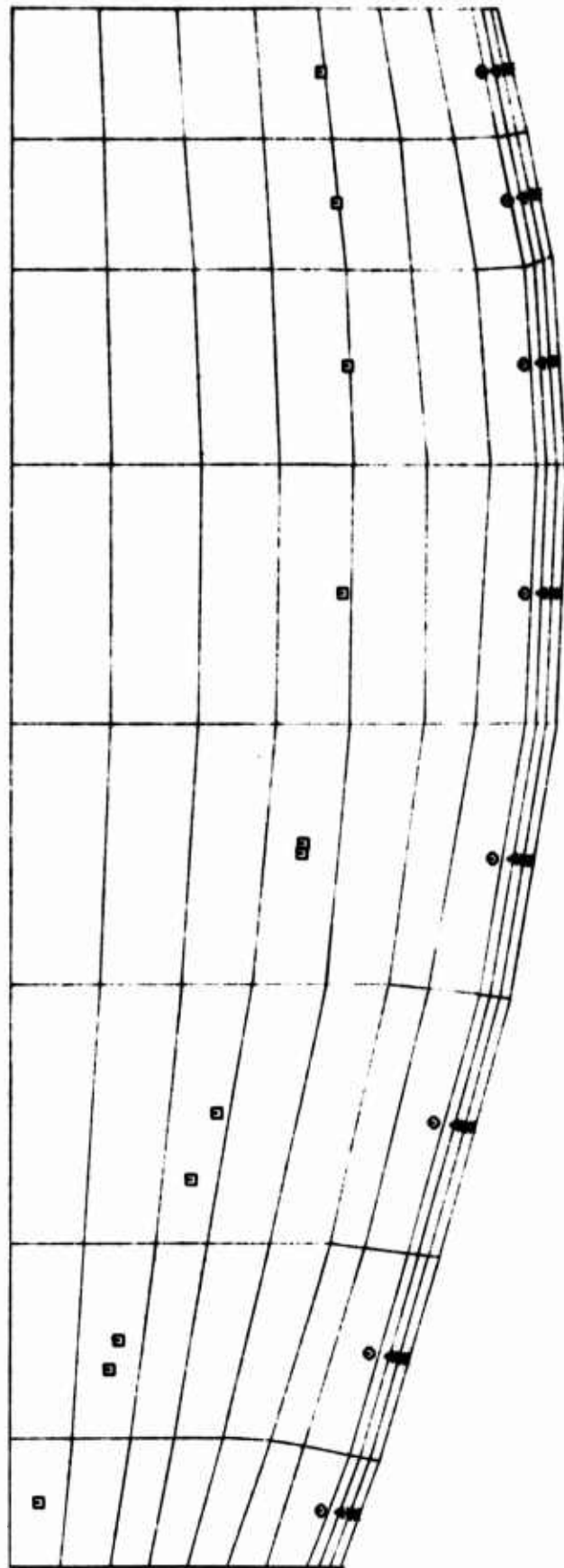


Figure 4-20. Isotherm Temperature Profiles for Nozzle Insert  
Nodal Grid -  $t = 30.0$  seconds

LEGEND

- \* SURFACE
- △ 5000 °R
- 4000 °R
- 3000 °R

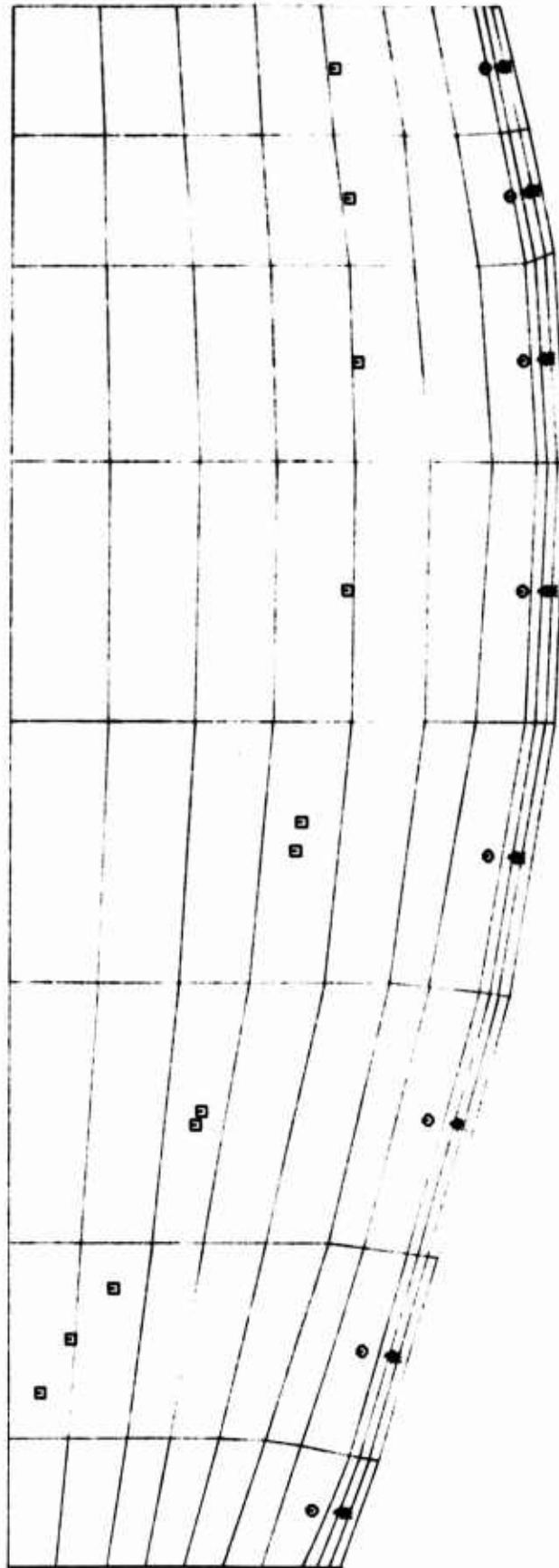


Figure 4-21. Isotherm Temperature Profiles for Nozzle Insert  
Nodal Grid -  $t = 60.0$

\* SURFACE  
 ◇ 5000° R  
 x 4000° R  
 + 3000° R  
 △ 2000° R  
 ○ 1000° R  
 □ 600° R

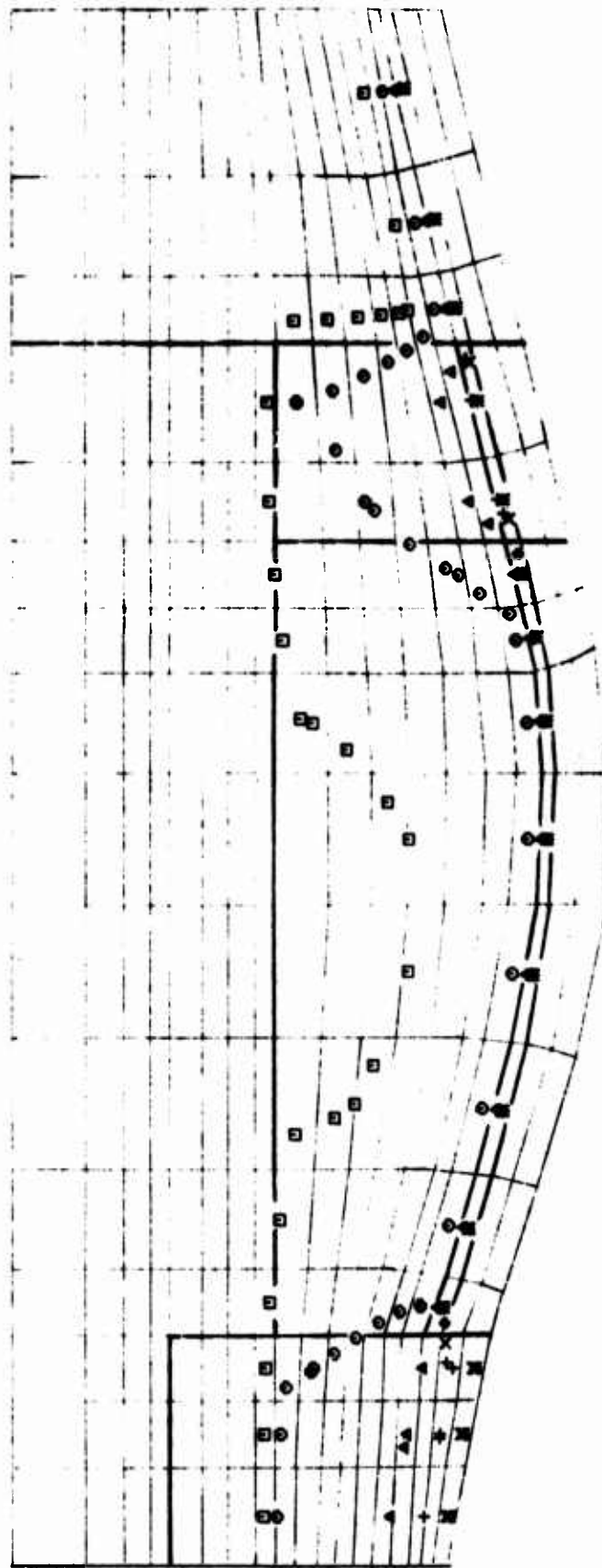


Figure 4-22. Isotherm Temperature Profiles for Nozzle Assembly  
 Nodal Grid -  $t = 1.5$  seconds



# LEGEND

\* SURFACE  
 ◇ 5000° R  
 x 4000° R  
 + 3000° R  
 △ 2000° R  
 ○ 1000° R  
 □ 600° R

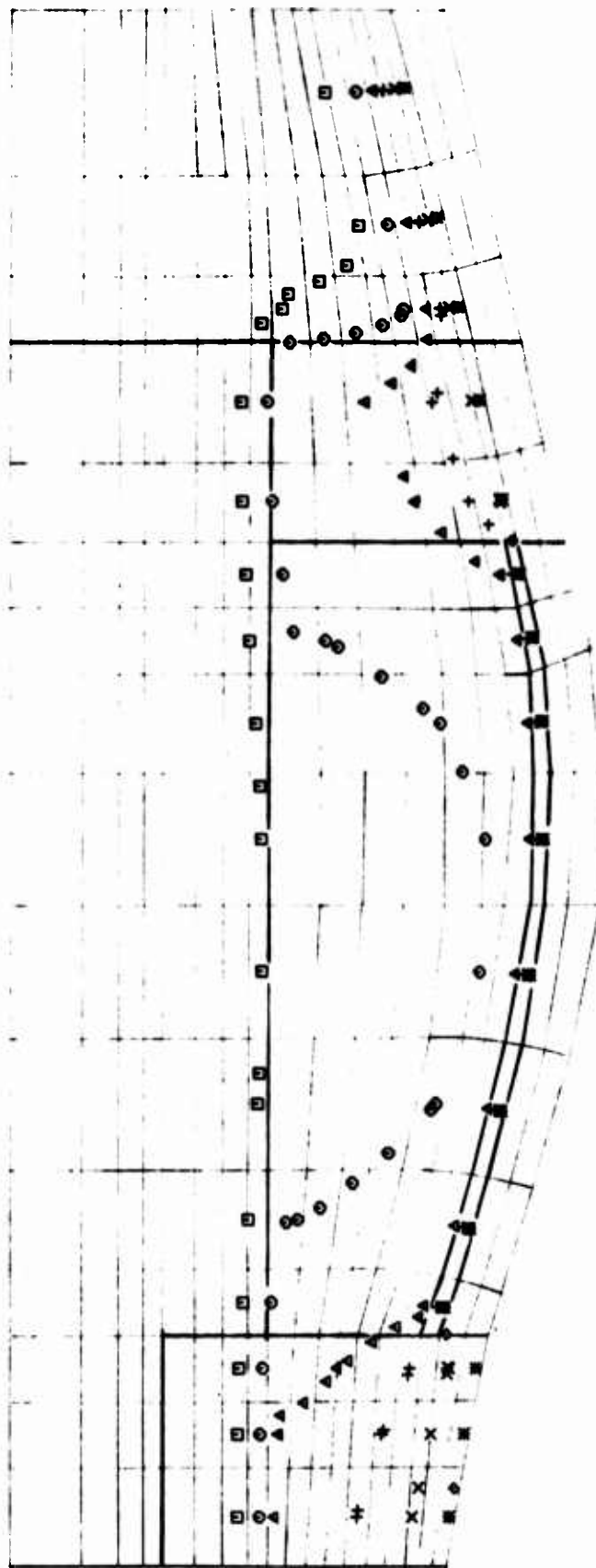


Figure 4-23. Isotherm Temperature Profiles for Nozzle Assembly  
 Nodal Grid -  $t = 5.0$  seconds

# LEGEND

\* SURFACE  
 ◇ 5000°R  
 X 4000°R  
 + 3000°R  
 △ 2000°R  
 ○ 1000°R  
 □ 600°R

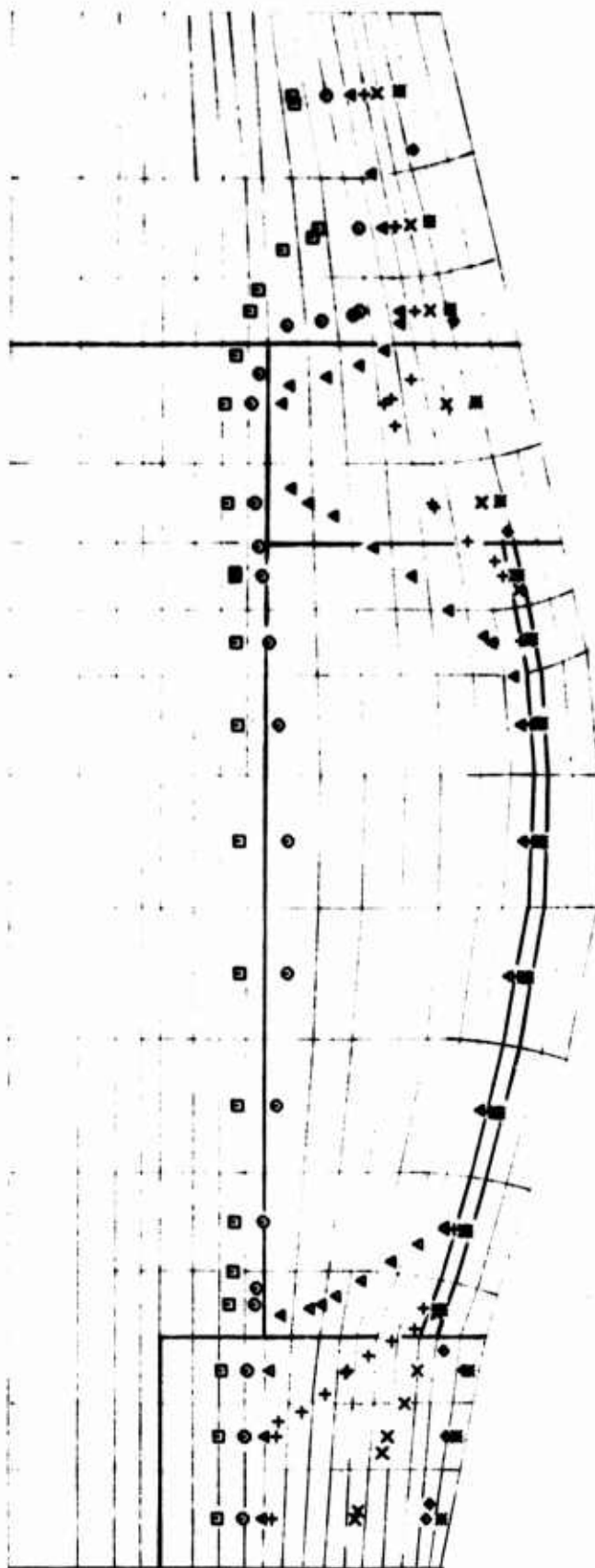


Figure 4-24. Isotherm Temperature Profiles for Nozzle Assembly  
 Nodal Grid -  $t = 10.0$  seconds

LEGEND

*	SURFACE
∪	5000° R
x	4000° R
+	3000° R
△	2000° R
○	1000° R
□	600° R

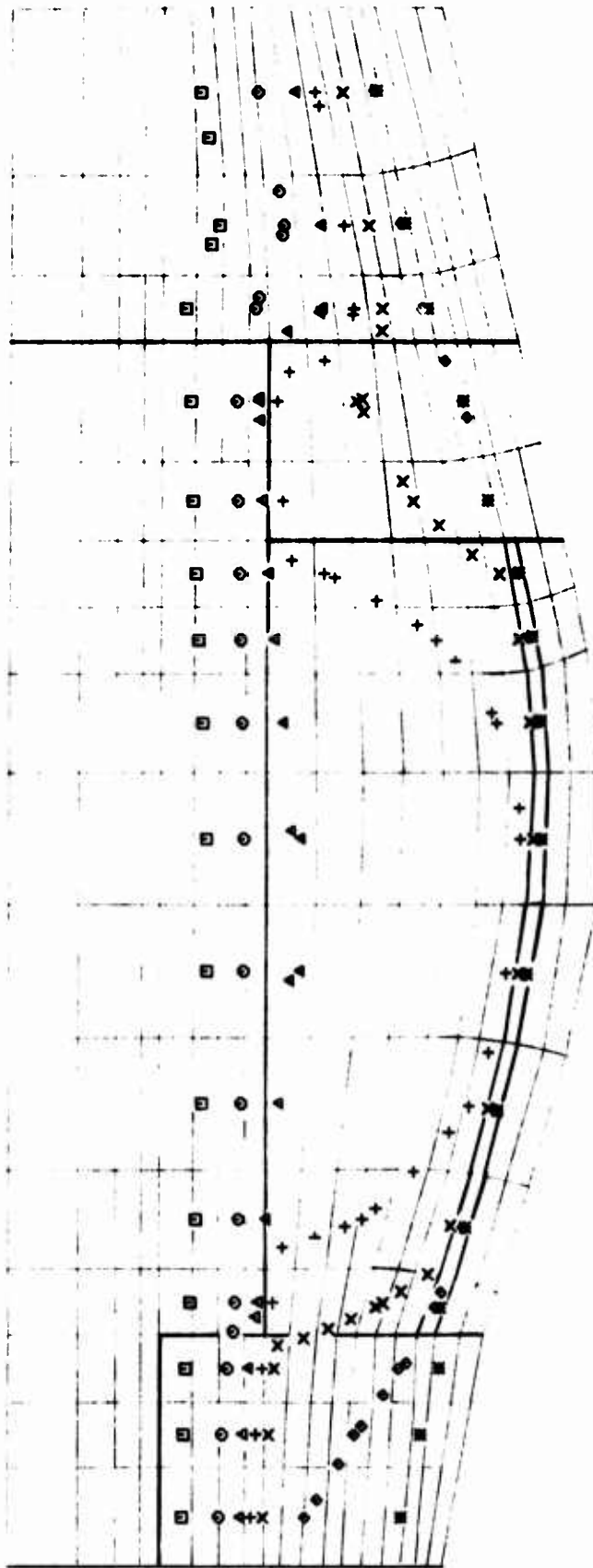


Figure 4-25. Isotherm Temperature Profiles for Nozzle Assembly  
Modal Grid -  $t = 30.0$  seconds

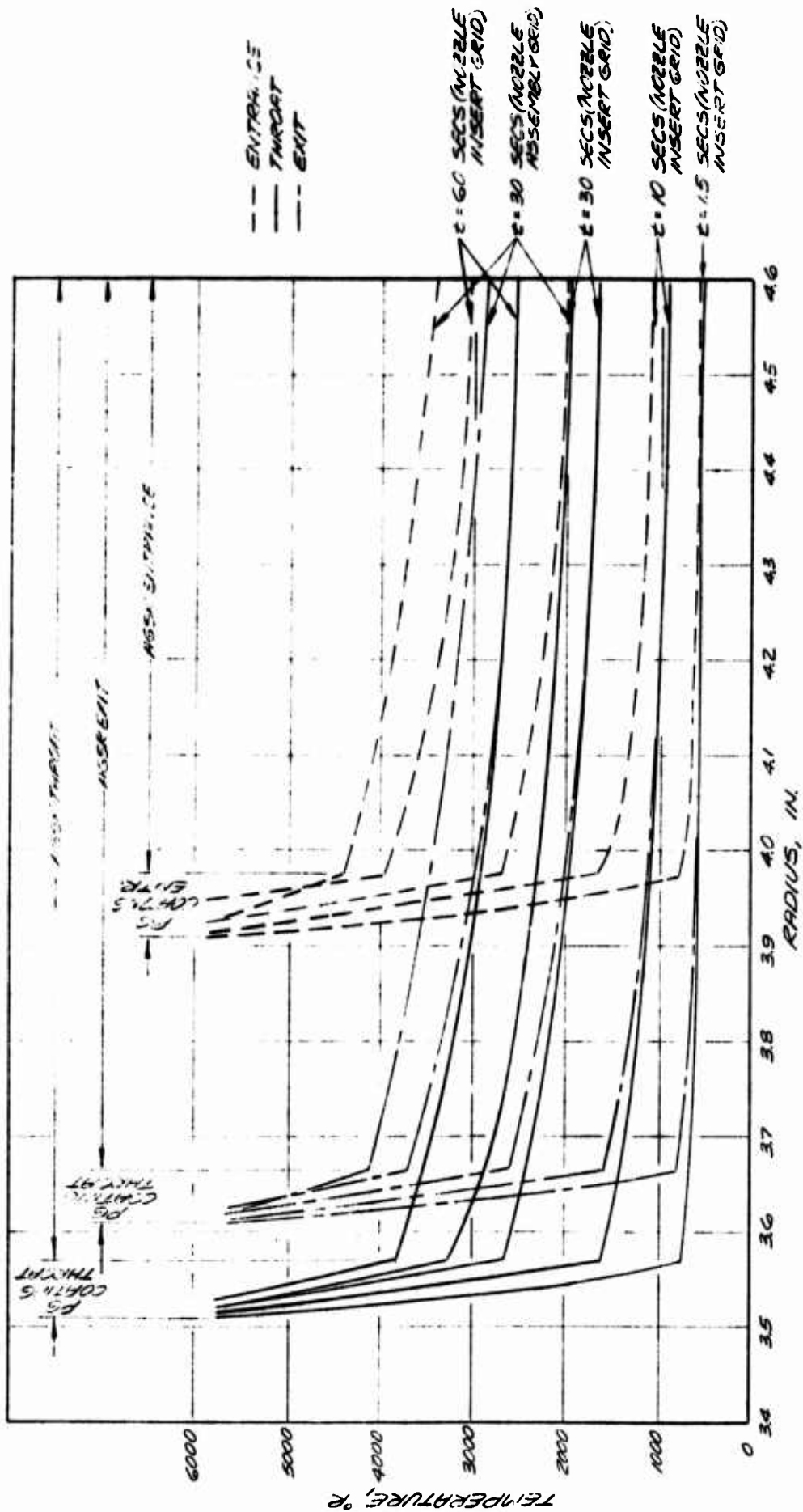


FIGURE 4-26 REPRESENTATIVE TEMPERATURE PROFILES THROUGH THE PYROLYTIC GRAPHITE THROAT INSERT.

LEGEND

\* SURFACE  
 ◇ 5000 °R  
 X 4700 °R  
 + 3000 °R  
 △ 2000 °R  
 ○ 1000 °R  
 □ 600 °R



Figure 4-27. Isotherm Temperature Profiles for Nozzle Insert Nodal Grid (Revised Pyrolytic Graphite Thermal Properties) -  $t = 1.5$  seconds

LEGEND

\* SURFACE  
 x 5000 °R  
 + 4000 °R  
 Δ 3000 °R  
 ○ 2000 °R  
 □ 1000 °R

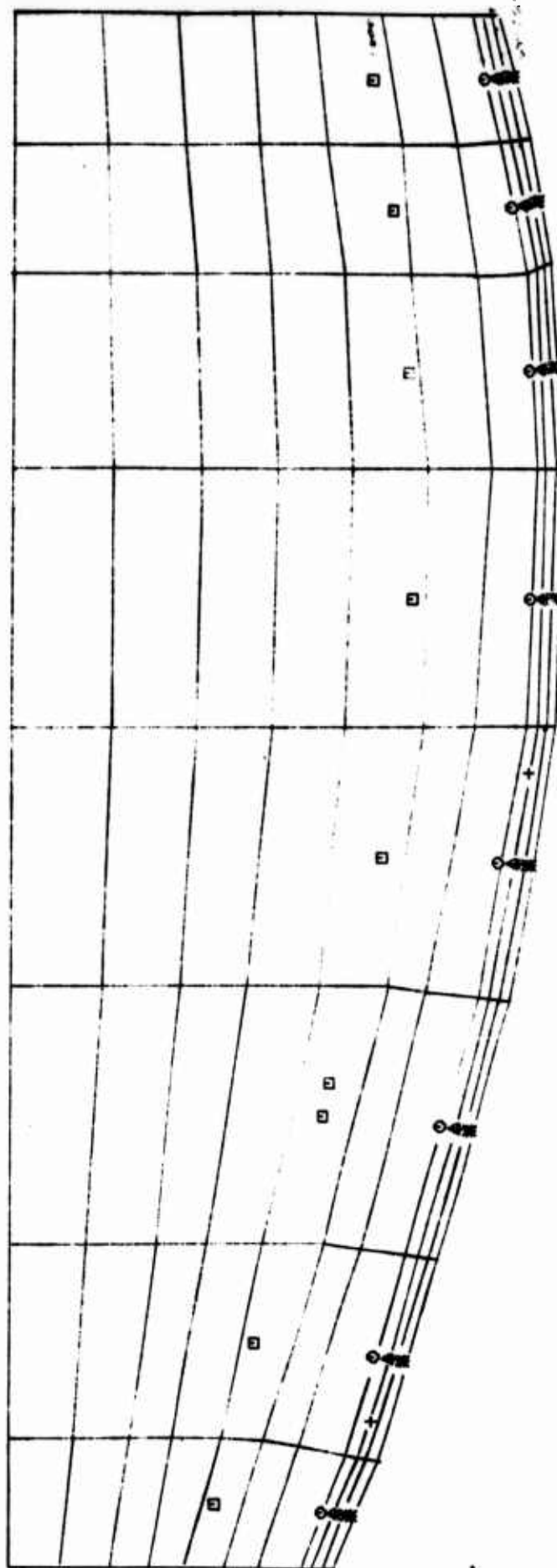


Figure 4-28. Isotherm Temperature Profiles for Nozzle Insert Nodal Grid (Revised Pyrolytic Graphite Thermal Properties) -  
 t = 5.0 seconds

LEGEND

*	SURFACE
x	5000 °R
+	4700 °R
Δ	3000 °R
○	2000 °R
□	1000 °R



Figure 4-29. Isotherm Temperature Profiles for Nozzle Insert Nodal Grid (Revised Pyrolytic Graphite Thermal Properties) -  $t = 10.0$  seconds

LEGEND

*	SURFACE
+	5000°R
Δ	4000°R
○	3000°R
□	2000°R



Figure 4-30. Isotherm Temperature Profiles for Nozzle Insert Nodal Grid (Revised Pyrolytic Graphite Thermal Properties) -  $t = 30.0$  seconds



LEGEND

\* SURFACE  
 Δ 5000 °R  
 ○ 4000 °R  
 □ 3000 °R

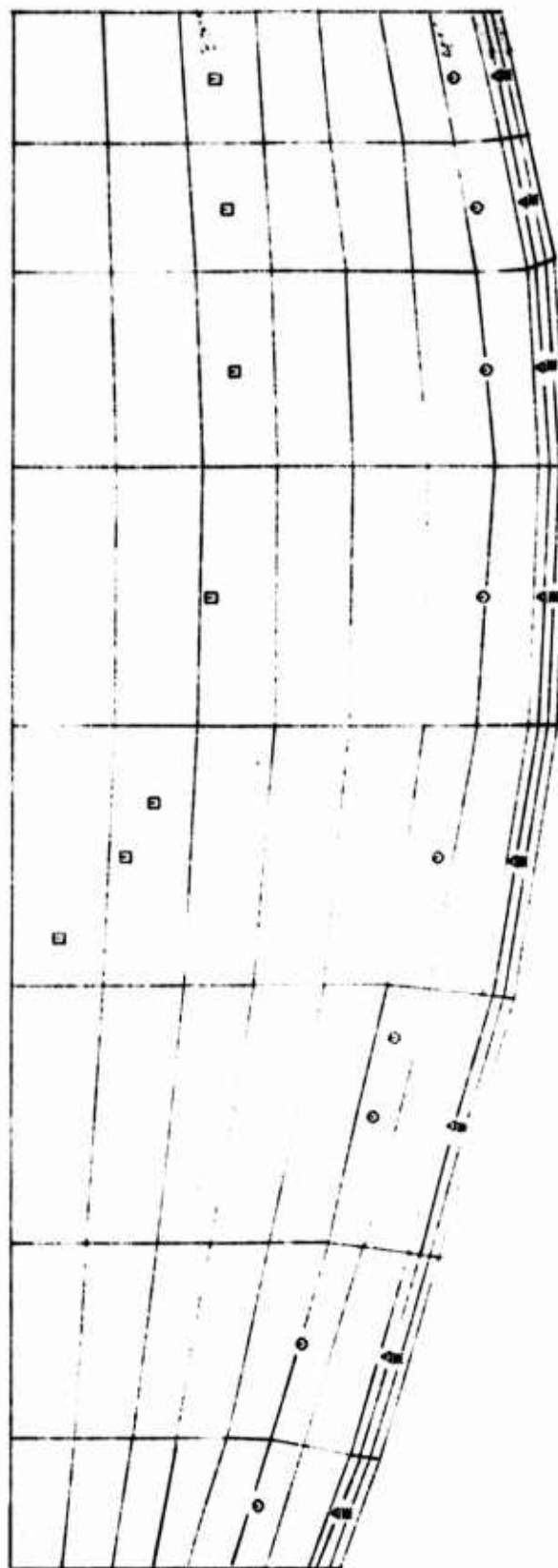


Figure 4-31. Isotherm Temperature Profiles for Nozzle Insert Nodal Grid (Revised Pyrolytic Graphite Thermal Properties) -  $t = 60.0$  seconds

## SECTION 5

### STRUCTURAL ANALYSIS

The overall objective of the structural analysis was to define the structural adequacy of the large PG coated nozzle throat insert using available design techniques and material properties. To evaluate this objective required performing structural analyses at three stages during the fabrication of the PG coated insert and at several times during the motor firing. As outlined in Table 5-1, structural analyses were performed for

- The heat up of the AGSR substrate to 2000°C
- The cooldown of the PG coated insert from 2000°C to room temperature
- The machining of the insert
- The motor firing corresponding to times of 1.5, 30.0, and 60.0 seconds

In addition, the results from the structural analyses were to provide some guidelines concerning the influence of the following design and/or analysis variables.

- Define the effect on the stress (or strain) distribution resulting from the placement of grooves in the upstream and downstream ends of the AGSR substrate
- Define the effect on the predicted stress (or strain) distributions resulting from the inclusion of plasticity effects in the analysis
- Define the effect on the predicted stress (or strain) distributions resulting from using the nozzle insert or nozzle assembly temperatures
- Define the effect on the predicted stress (or strain) distributions resulting from variations in the backside boundary constraints.

As shown by Table 5-1, the effect of the grooves in the substrate were evaluated for the cooldown of the PG coated insert and for a motor firing time of 1.5 seconds, the effect of including plasticity in the analysis was evaluated only for the cooldown of the insert, the effect of the temperature distribution

was evaluated for a motor firing time of 30 seconds, and the effect of the back-side constraint was evaluated for motor firing times of 1.5, 30.0, and 60.0 seconds.

The material properties used in the structural analyses have been presented in Section 3.2.2. The analytical tool used for these structural analyses was the Deformation Orthotropic Axisymmetric Solution of Inelastic Solids (DOASIS) computer program, and it is described in Section 5.1. The geometric representation of the nozzle insert is outlined in Section 5.2, and the analytical modeling of the insert fabrication process is presented in Section 5.3. The insert external boundary conditions are defined in Section 5.4, and the in-depth thermal loading is outlined in Section 5.5. Finally, the thermostructural response of the insert for the fabrication cooldown and motor firing environments is described in Section 5.6.

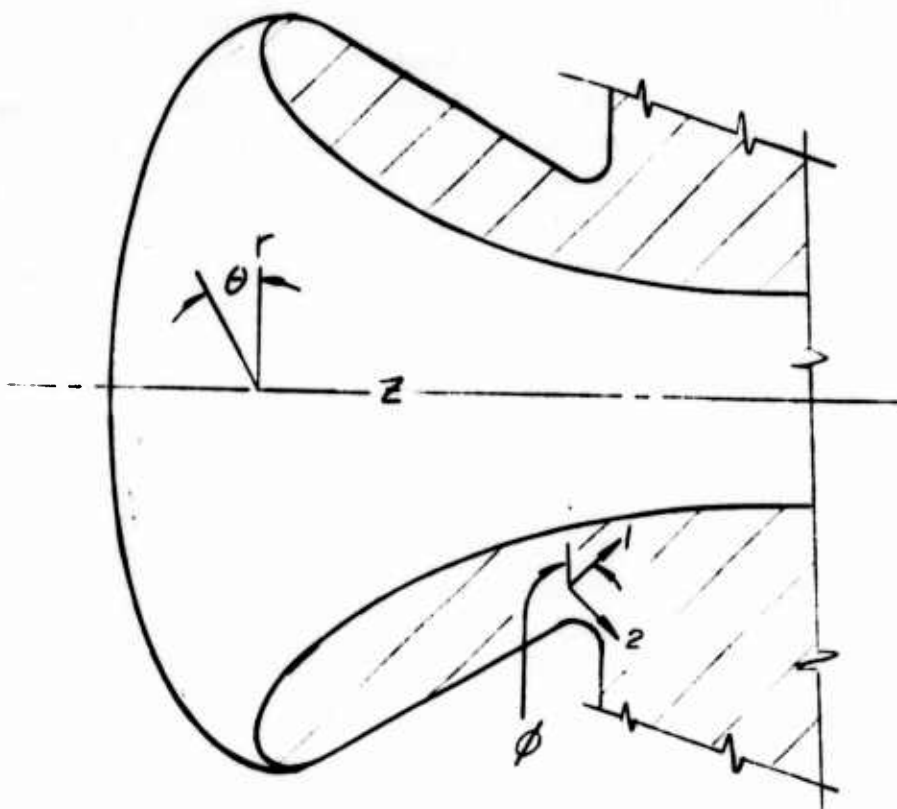
## 5.1 ANALYTICAL TECHNIQUES

The primary analytical tool used in the structural analysis of the rocket nozzle insert was the DOASIS computer code. The DOASIS program is a very general computer code which has the capability of analyzing the elastic-plastic behavior of either axisymmetric bodies of revolution, plane stress, or plane strain solids. The program is capable of handling generalized multi-modulus, orthotropic materials. The influences of thermal, pressure, shear, concentrated force, centripetal force, body force, and pre-stress loadings are accounted for. In addition, displacement and interference fit boundary conditions are available options.

DOASIS obtains the above-mentioned solutions by use of the finite element method. That is, a continuous body is subdivided into small, discrete, quadrilateral or triangular elements. The peripheral program MESHGEN generates this assemblage of elements for DOASIS by a Laplacian interpolation technique. The DOASIS program then uses this mesh and the material properties, loading and boundary condition data to generate a stiffness matrix for the given program. The elastic-plastic problem is then solved by the most efficient method available, i.e., by using an iterative technique in which only the nodal point force vector changes during the iterative process. Hence the stiffness matrix of the structure need only be generated once and decomposed once.

The program allows a general treatment of orthotropy. The material properties in each of the principal directions (designated as the 1-2- $\theta$  axis system) are independent and are input in tabular form as arbitrary functions of temperature. The sketch below provides a convenient representation of the generality. The program allows the principal (1-2) axes to be inclined at an angle  $\phi$  to the

r-z axis system. The angle  $\phi$  can vary from point to point in an arbitrary manner. The meridional (r-z plane) geometry can be completely arbitrary, but the loading must be axisymmetric.



For plasticity problems, the code uses the associated flow rule of plasticity theory. The magnitude of any plastic strain increment is determined by the strain hardening portion of the stress-strain curves (the tangent moduli) and their directions (ratio of the components with respect to one another) by the outward normal to the yield surface as described by the current stresses. The yield surface used here is a modified form of the Hill-Hu orthotropic yield surface given by

$$\bar{\sigma}^2 = \alpha_{r\theta}(\sigma_r - \sigma_\theta)^2 + \alpha_{\theta z}(\sigma_\theta - \sigma_z)^2 + \alpha_{zr}(\sigma_z - \sigma_r)^2 + \beta_{rz}\tau_{rz}^2 = \bar{Y}^2$$

where  $\bar{\sigma}$  = equivalent stress,  $\bar{Y}$  = equivalent yield stress and  $\alpha_{ij}$  = anisotropic parameters. A full development of the theory can be found in the Aerotherm DOASIS User's Manual (Reference 15).

The peripheral programs besides MESHGEN which feed input data to DOASIS are (1) TEMINT, a generalized temperature interpolator program which takes an arbitrary two-dimensional temperature distribution and interpolates to find the temperatures of all the points required by the DOASIS code; (2) GETPR, a program designed to translate a given pressure distribution on the outside surface of a sphere-cone geometry to the outside surface of a similar structural finite element mesh and generates a general "cosine" distribution of pressure for the backside surface of the structural finite element mesh; (3) INTERG, a program which uses the results of a DOASIS computer run to calculate maximum and minimum stresses, strains and strain ratios, and determines the locations of all the components of the different variables; and (4) CONTOUR, a program which is designed to make contour plots of the analysis results generated by the DOASIS computer code.

## 5.2 GEOMETRIC REPRESENTATION OF ROCKET NOZZLE INSERT

### 5.2.1 Insert Without Stress Relieving Grooves

The finite element structural representation of the rocket nozzle insert without stress relieving grooves is shown in Figure 5-1. A total of 195 elements were used to represent the AGSR portion of the insert, and 45 elements accounted for the PG coating. A finer mesh was used in the PG coating because of the large stress and strain gradients expected there. The dimensions of the entire mesh correspond to the geometry of the insert before machining 0.1 inch from the ends. The structural mesh of the insert without grooves was used primarily to compute cooldown stresses. These computations were used as a basis for determining the effect of grooves in reducing the residual stresses in an insert resulting from cooldown. Only one motor firing structural analysis was performed using the mesh without grooves. In that particular case, the mesh was modified by shortening the end elements to account for the machining process which was performed prior to placing the insert in the rocket nozzle structural shell.

### 5.2.2 Insert with Stress Relieving Grooves

The finite element structural representation of the rocket nozzle insert with stress relieving grooves is shown in Figure 5-2. A total of 391 elements were used to represent the AGSR portion of the insert, and 45 elements accounted for the PG coating. A finer mesh was used with this geometry for several reasons:

1. The presence of the grooves results in larger stress concentration gradients near the ends of the insert

2. Elements at the ends were required to be 0.1 inch thick so that they could be removed when analyses were performed on a machined insert.
3. Motor firing loadings and boundary conditions were applied to the insert with grooves, therefore large radial thermal gradients were present in the PG coating.
4. The PG coating ablated during the motor firing, hence a variable number of elements were removed from the coating depending on the number of seconds elapsed in the motor firing.

### 5.3 MODELING OF THE INSERT FABRICATION PROCESS

The fabrication of the rocket nozzle insert was modeled by decomposing the process into several steps. Each step was chosen such that there was no need for any simplifying assumptions with regard to the material response. The results of each preceding step were inserted as input data to the next step in the process, if necessary. The fabrication process was segmented as follows (also refer to Figure 5-3):

1. An unmachined billet of AGSR without a PG coating and in a stress free state is machined so that the stress relieving grooves are placed on both ends of the substrate, and the nozzle contour is placed on the inner surface of the substrate.
2. The billet of AGSR is next heated from 70° to 2000°C.
3. The PG coating is placed on the inner surface of the AGSR substrate at 3634°F (2000°C).
4. The combined PG coating and AGSR substrate are then cooled to 70°F.
5. The insert is then machined so that 0.1 inch is removed from each end.

This completes the fabrication process. In each step, the surface of the insert was assumed to be stress free.

### 5.4 DEFINITION OF INSERT BOUNDARY CONDITIONS FOR MOTOR FIRING

Once the fabrication process is complete, the insert is placed in position in the rocket nozzle structural shell. At this point it becomes very important to properly define the boundary conditions on the exterior surfaces of the insert. These boundary conditions are illustrated in Figure 5-4. The various faces of the insert are defined as the inner, outer, upstream, or downstream surfaces. Each surface will be considered separately.

#### **5.4.1 Inner Surface Boundary Condition**

The inner surface of the insert faces the nozzle chamber environment. It is, therefore, exposed to the severe pressure, thermal, and corrosive environment of the propellant combustion products. For the 7-inch diameter PG coated nozzle insert, the pressure varies approximately linearly from 57.5 atmospheres at the upstream edge to 26.7 atmospheres at the downstream edge. The severe thermochemical environment causes the PG coating to ablate so that the thickness of the coating varies during the motor firing.

#### **5.4.2 Outer Surface Boundary Condition**

The outer surface of the AGSR is overwrapped with 0.006 inches of teflon which is separated from the silica cloth phenolic by a 0.10 inch thick bondline of EA913 adhesive. Various boundary conditions were placed on this surface depending on the particular case considered. In cases where the 1.5 second motor firing conditions were considered, it was assumed that the bondline and teflon were rigid compared with the AGSR, and hence there was no displacement in the radial direction but free movement in the axial direction. In cases where the 30 and 60 second motor firing conditions were considered, it was assumed that the teflon evaporated in one case, and that both the teflon and the bondline evaporated in another case. Therefore, the boundary condition on the outer surface in these two cases was a stress free condition until the insert expanded to contact the silica cloth phenolic. This is also referred to as an interference fit boundary condition. In another case, a 0.2 inch thickness of multi-layered grafoil was assumed to exist between the AGSR and the silica cloth phenolic. In this case, the outer surface of the grafoil was assumed to be a rigid boundary but free axial movement was allowed. The inner surface of the grafoil was assumed bonded to the outer surface of the AGSR.

#### **5.4.3 Upstream Surface Boundary Condition**

The upstream surface of the rocket nozzle insert is separated from the Speer 8882 material by a 0.005 to 0.02 inch thick bondline consisting of Armstrong A-2. This bondline was assumed to be structurally weak, hence the pressure at the inner edge of this surface was assumed to be transmitted throughout the Armstrong A-2. Therefore, the boundary condition on the upstream surface was always assumed to be a pressure of 57.5 atmospheres.

#### **5.4.4 Downstream Surface Boundary Condition**

The boundary condition on this surface was the most complicated because:



1. The pressure on the surface must be greater than the local gas static pressure in order to place the insert in force equilibrium during the motor firing.
2. The differential surface recession rate between the PG coating and the bulk graphite continually changes the area over which this reaction pressure is applied.
3. The 0.005 to 0.020 inch thick bondline of Armstrong A-2 between the AGSR and the Speer 9139 gradually degrades during the motor firing, and, thus, at any instant of time, it has a variable stiffness in the radial direction,

After 1.5 seconds into the motor firing, the reaction pressure which acts over the entire surface was calculated to be 57.6 atmospheres. However, for the 30 and 60 second cases, the possibility exists that the combined effect of items 2 and 3 could reduce the effective area over which the reaction pressure is applied. In this event, the effective area is assumed to include the downstream surface area between the inner edge of the groove and the outside radius of the substrate (refer Figure 5-4). For this effective surface area, the average pressure is based on the local static pressure of 26.7 atmospheres being applied to the remainder of the downstream surface which includes the area from the inner edge of the PG coating to the inner edge of the groove. However, because the bondline has significantly degraded at the later times, the AGSR is probably in contact with the Speer 9139 bulk graphite. Hence, the boundary condition over the effective area portion of the downstream surface for the 30 and 60 second cases was chosen as one with no axial displacement but free radial movement. The other boundary condition used for the 30 and 60 second cases was the same as used for the 1.5 sec cases.

## 5.5 DEFINITION OF INSERT INTERNAL LOADING CONDITIONS

The only internal loading on the rocket nozzle insert during a motor firing is that resulting from the two-dimensional temperature distribution. The temperature distribution in the insert as a function of time was determined by the ASTHMA code. However, as discussed in Section 4.3, two different temperature distributions were calculated depending on whether the nozzle insert alone was investigated or whether the entire nozzle assembly was included in the heat transfer analysis. For most cases, the nozzle insert temperature distribution was used for the structural analyses; however, a check case at 30 seconds was performed with the entire nozzle assembly temperature distribution.



## 5.6 PREDICTED STRUCTURAL RESPONSE

Based on the previously described geometry, material properties, loading, and boundary conditions, structural analyses were performed to determine the stress-strain-displacement state of the rocket nozzle insert during both the fabrication process and a 60 second motor firing. As outlined in detail in Table 5-2, calculations were performed for a total of 18 different conditions. In this table, these conditions are defined by case number, solution type (elastic-plastic), the AGSR substrate type (with or without stress relieving grooves), the temperature of the insert, the time elapsed since the start of the motor firing (unless the condition was related to some state during the fabrication process of the insert), the surface boundary conditions which are explained in more detail in Table 5-3, the reference stress free state, and any necessary explanatory remarks. The results of these calculations are subdivided into two categories: those relevant to the fabrication process which are presented in Section 5.6.1 and those relevant to the motor firing which are presented in Section 5.6.2.

### 5.6.1 Fabrication Process

As discussed in Section 5.3, the fabrication of the rocket nozzle insert can be subdivided into several steps. The results of the structural analyses for each of these steps is presented below.

#### 5.6.1.1 Heating to 3634°F

The first step consisted of heating a billet of AGSR from 70°F to 3634°F. Results of the numerical calculations (Cases 1 and 2) indicated that the stresses and strains at 3634°F were negligible although the insert expanded 22 mils radially outward and 14.5 mils axially.

#### 5.6.1.2 Cooling to 70°F with PG added

The second step in the fabrication process, from the structural point of view, consisted of coating the AGSR substrate at 3646°F with the pyrolytic graphite coating then cooling the combination back to 70°F. Due to the differences in the coefficients of thermal expansion of the two materials, the cooling of the coated substrate from 3646°F to 70°F generates internal stresses. Cases 3, 5, and 6 of the numerical calculations define this stress state under three different conditions. Cases 3 and 5 assume the material behavior can be characterized as linear elastic, but Case 3 is for a grooved substrate and Case 5 is for a non-grooved substrate. Case 6 assumes that the insert has stress relieving grooves, but that the material behavior can be characterized as elastic-plastic. Each of these cases are discussed in more detail below.

#### 5.6.1.2.1 Insert with Grooves vs. Insert without Grooves

The basic reason for the use of stress relieving grooves in the insert was to reduce the large interlaminar shear stresses in the insert at the interface between the AGSR and the PG coating. Figure 5-5 illustrates to what extent these shear stresses were reduced by the grooves. The results indicate that the grooves reduce the peak shear stresses on the upstream side of the insert by 30 percent, and on the downstream side by about 27 percent. Further results (Figures 5-6 and 5-7) indicate that the hoop stresses in the PG coating for the grooved substrate are reduced by as much as 21 percent. However, for certain regions in the AGSR, the hoop stresses and strains are larger in the insert with grooves. The results are illustrated in Figures 5-8, 5-9, and 5-10. Furthermore, Figures 5-11 and 5-12 indicate regions in the AGSR where failure of the material would be predicted. This prediction is based on the stress-strain curve for AGSR at 70°F as shown in Figure 3-12 of Section 3.2.2. A given element in the structural grid was assumed to have failed if the level of the hoop strain exceeded  $1.35 \times 10^{-3}$  in/in. This is a good approximation because the principal strains in each element are only slightly larger than the hoop strains. Figures 5-11 and 5-12 indicate that the presence of the groove at the downstream end of the insert causes a localized region of failure.

#### 5.6.1.2.2 Plastic Analysis vs. Elastic Analysis

The elastic-plastic analysis (Case 6) was performed to determine how plastic deformation affected the level of total strain and displacement in the insert as a result of the cooldown process. The material yield properties and tangent moduli were discussed in Section 3.2.2, and the method of plastic analysis was described in Section 5.1. The numerical calculations indicate that plastic deformation reduced the stresses in the insert only slightly; however, the strains and displacements were increased far more significantly. The hoop strains as calculated by the plastic and elastic analyses are plotted as functions of radial position in Figures 5-8, 5-9, and 5-10. The total strain in a plastic analysis is defined as the sum of the elastic and plastic portions. However, note that the elastic portion of a plastic analysis is not the same as the total strain in an elastic analysis. It is seen from these figures that the maximum strains occur in the entrance plane (upstream surface) of the insert, and the lowest strains occur in the throat plane. The important conclusion to be drawn from these figures is that the total strains as determined by

the plastic analysis are significantly higher (as much as 21 percent) than those determined by an elastic analysis.

Although the stresses determined by the plastic analysis are slightly lower than those calculated by an elastic analysis (e.g., see Figures 5-5 and 5-13), it is the strain level that causes material failure not the stress level. Therefore, the fact that an elastic analysis is more conservative in the estimation of stress levels does not mean that an elastic analysis is more conservative in the prediction of failure. Hence a plastic analysis, which is more conservative in the estimation of strain levels than an elastic analysis, is more appropriate for the prediction of a material failure. The importance of the previous statement becomes more apparent if reference is made to Figure 5-14. The results of the elastic analysis indicate that failure occurs in a small region near the ends of the insert and near the AGSR-PG interface. This region is shown in Figure 5-12. The plastic analysis indicates that failure occurs in a larger region. The failure criterion for the substrate was again based on the hoop strain state exceeding  $1.35 \times 10^{-3}$  in/in.

Another difference, although relatively minor, between the plastic and elastic analyses is illustrated by Figure 5-15. This plot depicts the displacement of the outer and inner surfaces of the AGSR as functions of axial position for the heating and cooling portions of the insert fabrication process. Displacements due to the cooling portion were determined by both plastic and elastic analyses. It is seen that the contraction predicted by a plastic analysis is slightly less than that predicted by an elastic analysis.

#### 5.6.1.3 Machining the Ends

The final step in the fabrication process consisted of machining 0.1 inch from the upstream and downstream surfaces of the insert at 70°F. Since a non-zero stress state existed in the insert at 70°F, the effect of machining on this state was considered. This was done by removing elements from the structural grids (with and without grooves) to simulate the machining process and allowing the stresses in the insert to redistribute. The results from this analysis indicated that the machining process caused a negligible redistribution of stresses, strains, and displacements in the insert.

#### 5.6.2 Motor Firing

The structural analysis of the motor firing was performed by calculating the stress state in the insert at various instants in time during the motor burning. The times chosen were 1.5, 3.0, and 60.0 seconds.

The 1.5 second stress state was analyzed because the temperature gradient in the insert is most severe at the beginning of the firing. Hence, the PG coating is at a much higher temperature near the surface than at the AGSR-PG interface. The 30.0 second condition was important because rocket motor experimental tests were conducted for both 30 and 60 second durations; hence, a numerical analysis of the stress state at 30 seconds enabled investigation of an intermediate condition for one firing as well as a burnout condition for another firing. The 60.0 second condition was, of course, important because the temperature of the insert was highest near the end of the firing. This temperature causes the compressure force between the insert and its backside boundaries to be a maximum. In addition, the differential expansion between the PG and AGSR would be expected to cause a high stress level at the interface.

Because the material properties vary with temperature, the reference or initial state of the insert for the stress analysis had to be stress free which meant that the state at 3634°F had to be the reference state. However, the structural results from the plastic analysis showed that significant plastic strains occurred during cooldown of the insert. This means that proper definition of the motor firing strains requires the input of plastic strains into the stress analysis as initial conditions at an insert temperature of 70°F. However, the handling of this initial condition is beyond the capability of the DOASIS code, but it can be handled by the OASIS code (Ref. 26), although at a significant increase in cost which made it impractical for this investigation. As a result the influence of the plastic strains on the motor firing strains were neglected and the state at 3634°F was used as the stress free state.

As mentioned in Section 4.3, two different nozzle insert temperature distributions were generated in the heat transfer analysis. One was determined considering only the nozzle insert and the other was determined considering the entire nozzle assembly. For all but one of the stress calculations (Case 11), the former temperature field was used.

In the following sections, the results of the stress analyses are presented separately for each point in time. Tables 5-2 and 5-3 present a summary of the various conditions for which analyses were performed.

#### 5.6.2.1 Stress State - 1.5 Seconds

Stress analyses were performed at the 1.5 second state for three different conditions. Cases 7 and 8 shared identical boundary conditions; that is, the upstream and downstream surfaces were pressurized, and the outer surface was not allowed to displace radially. However, Case 7 analyzes an insert with grooves, and Case 8 analyzes an insert without grooves. Case 9 was identical to Case 7 except that the reference stress free state was chosen as 70°F. This case, in fact, was the only one in which the reference stress free state was

not chosen as 3634°F. The results of Case 9 were used as a basis for comparing the present solution technique with previous superposition solution techniques. The results of this comparison are discussed in detail in Section 5.6.3. The results for Cases 7 and 8 are shown in Figures 5-16 through 5-21 where the shear stresses at the PG-AGSR interface are plotted as functions of axial position and the hoop stresses in the PG and AGSR are plotted as functions of radial position at the entrance, throat, and exit planes of the insert. The maximum shear stress (Figure 5-16) is smaller in the insert with grooves. However, it appears that the downstream groove is not as effective as the upstream for reducing shear stresses.

The maximum hoop stresses in the PG occur near the nozzle throat plane. Comparing the hoop stresses in the grooved and nongrooved inserts, it is apparent that although the distributions of stress are different, the maximum magnitude of the stresses are not very different. The same conclusion can be drawn about the hoop stress level in the AGSR (Figures 5-20 and 5-21).

#### 5.6.2.2 Stress State - 30.0 Seconds

Numerical calculations were performed at the 30 second state for six different sets of conditions (Cases 10 through 15). Reference to Tables 5-2 and 5-3 provides a summary of these conditions. The temperature field determined by the heat transfer analysis of the nozzle insert was used for all cases except Case 11. The temperature field for Case 11 was the field calculated by considering heat transfer to the entire nozzle assembly. The upstream and downstream surfaces of the insert were always assumed pressurized, except for Case 12 where a mixed boundary condition was placed on the downstream surface. From this case, the portion of the surface between the outer edge and the groove was not allowed to displace axially. This condition was described in detail in Section 5.4.4. The outer surface of the insert was not allowed to displace radially for Cases 10, 11, and 12. However, in Cases 13 and 14, the outer surface was allowed to displace radially outward a distance of 5 mils and 16 mils respectively before encountering a rigid boundary. In Case 15, a 0.2 inch gap filled with grafoil was placed between the outer surface of the insert and the silica phenolic. The silica phenolic was assumed to be rigid with respect to the radial and axial displacements.

The structural finite element grid of the insert for the 30 second state was slightly modified to account for the material recession at the PG surface. A layer of finite elements 10 mils thick was removed from the structural grid to approximate the material recession. Actual calculations of material recession were discussed in Section 4.3.2. Case 10 was considered as the "baseline"



condition for the 30 second state calculations. Case 11 was performed to assess the difference in the stress state using the nozzle assembly temperature distribution. Cases 12, 13, 14, and 15 were performed to determine the effects of various boundary conditions on the stress state in the insert.

The results of all these calculations are shown in Figures 5-17 through 5-23. They indicate that the nozzle assembly temperature distribution produces hoop and radial stresses significantly higher than those produced by the nozzle insert temperature distribution. The increased stresses are principally due to the additional heat flux through the ends of the insert from the rest of the nozzle assembly.

Comparisons of various outer surface boundary conditions (Figure 5-22) indicate that the highest compressive hoop stresses (9300 psi) occur in the AGSR if the outer surface is not allowed to expand radially. The minimum stresses (-450, +100 psi) occur in the AGSR if the outer surface is allowed to expand radially outward 5 mils. The maximum tensile hoop stresses occur in the AGSR if the outer surface is allowed to expand radially outward 16 mils, or if the 0.2 inch thick layer of grafoil is placed in the gap between the outer surface and the silica phenolic. The hoop stresses in the PG (Figure 5-23) were maximized in compression if the outer surface was not allowed to expand radially. The hoop stresses became smaller as the outer surface was allowed to expand further. Comparison of the results from the two cases which considered the variation in the downstream boundary condition showed that this variation had a negligible influence on the stress distribution.

In general, the stress level at the 30 second state is higher than the level at the 1.5 second state. The stresses increase the most at the PG-AGSR interface. The only stresses which decreased below their level at the 1.5 second state were the interlaminar shear stresses in both the PG and AGSR.

#### 5.6.2.3 Stress State - 60.0 Seconds

Numerical calculations were performed at the 60 second state for three different sets of conditions (Cases 16 through 18). Reference to Tables 5-2 and 5-3 provides a summary of these conditions. The only differences between the three conditions were the insert outer surface boundary conditions. For Case 16, the outer surface was not allowed to displace radially. In Cases 17 and 18, the outer surface was allowed to displace outward 5 mils and 16 mils respectively. Another 10 mils were removed from the structural grid for the 60 second state to account for further material ablation. The total amount of material removed since the beginning of the firing was 20 mils.

The stress state for each of the three 60 second conditions is shown in Figures 5-17 through 5-21 and Figures 5-24 and 5-25. The latter two figures provide a comparison of the hoop stress level in the insert for various outer

surface boundary conditions. It is apparent that the stress level is the lowest if the outer surface is allowed to expand radially 16 mils before encountering a rigid boundary, and highest if it is not allowed to expand radially at all.

The hoop stresses at the PG-AGSR interface reach a level at the 60 second state which is higher than at any other time in the motor firing. The peak hoop stress encountered for any boundary condition was -15200 psi.

### 5.6.3 Comparison of Present Technique with Superposition Principle

Some previous stress analyses conducted by other investigators have been performed on the rocket nozzle insert using a superposition principle. These analyses calculated the motor firing stresses by adding the results of two separate calculations. The first calculation generated the stresses resulting from the cooldown process assuming that 3634°F was a stress free state. The second calculation generated stresses resulting from exposing an insert to a motor firing condition assuming that 70°F was a stress free state.

The stress analysis technique used for the calculations in this report assumed that the stress free state of the insert was at 3634°F for both the cooldown and motor firing condition. The validity of this approach is based on two assumptions. The first assumption is that machining of the ends of the insert prior to placing it in the nozzle assembly does not appreciably alter the stress distribution in the insert. The results of Case 4 verify that this assumption is well founded. The second assumption is that the effect of the cooldown plastic strains can be neglected.

If the material properties of the PG and AGSR were not temperature dependent and if the geometry of the insert were not different at the 70°F and 3634°F states, the two techniques would produce identical results. However, this is not the case because the partial differential equation governing the state of stress in the insert is dependent on material properties. Superposition of solutions of this partial differential equation is valid only if the superposed solutions are governed by the same partial differential equation. As shown in Section 3.2.2, the material properties of PG and AGSR vary considerably with temperature. Hence, the partial differential equations governing each step in the superposition technique are different. Therefore, it is not valid to superpose the solution of each step. A secondary reason why superposition is invalid is that the insert contracts in going from 3634°F to 70°F; hence, the region governed by the partial differential equation changes in each step of the superposition technique.

A comparison of the results obtained by each method is shown in Figure 5-26. The hoop stresses in the PG at the 1.5 second state of the motor firing

are plotted as functions of the distance normal to the surface of the PG using both techniques. The results indicate that the superposition principle diverges from the present technique in the critical region of largest temperature gradient. At the PG surface, the results differ by 35 percent.





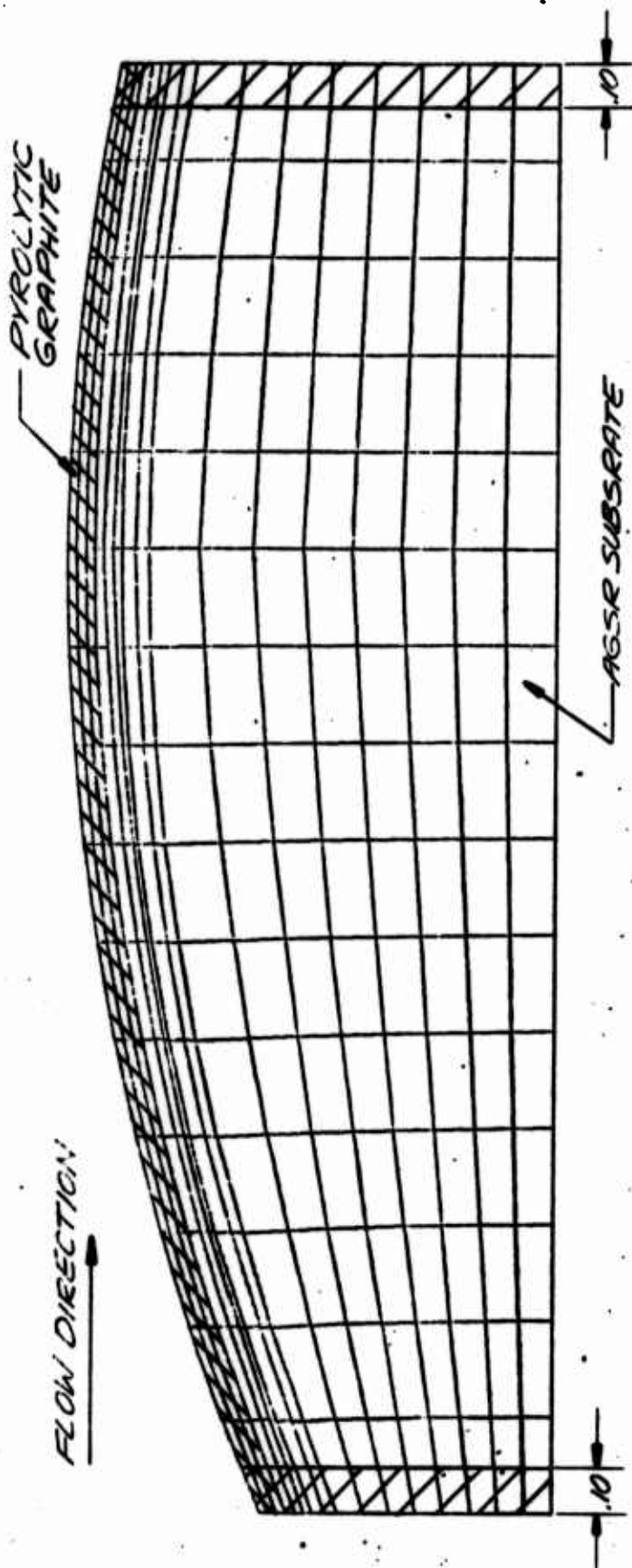
TABLE 5-2  
SUMMARY OF STRUCTURAL ANALYSES  
PERFORMED USING DOASIS COMPUTER PROGRAM

Run No.	Solution Type	Substrate Time	Temperature	Motor Firing Time (sec)	Boundary Conditions (See Table 5-3)	Zero Stress State	Remarks
1	Elastic	Grooved	3634°F	---	Stress Free Boundaries	70°F	Define stresses and thermal expansion for substrate only
2	Elastic	Non-Grooved	3634°F	---	Stress Free Boundaries	70°F	Same as for Run No. 1
3	Elastic	Grooved	70°F	---	Stress Free Boundaries	3634°F	Cooldown following application of PG coating
4	Elastic	Grooved	70°F	---	Stress Free Boundaries	3634°F	Define stress redistribution due to machining ends
5	Elastic	Non-Grooved	70°F	---	Stress Free Boundaries	3634°F	Same as for Run No. 3
6	Plastic	Grooved	70°F	---	Stress Free Boundaries	3634°F	Plastic cooldown analysis
7	Elastic	Grooved	Nozzle Insert	1.5	11, 01, 01, D1	3634°F	Motor firing stress analysis with zero backside disp.
8	Elastic	Non-Grooved	Nozzle Insert	1.5	11, 01, 01, D1	3634°F	Same as for Run No. 7
9	Elastic	Grooved	Nozzle Insert	1.5	11, 01, 01, D1	70°F	Same as for Run No. 7 70°F assumed as stress free state
10	Elastic	Grooved	Nozzle Insert	30	12, 01, 01, D1	3634°F	Determine effect of temperature gradient by comparing
11	Elastic	Grooved	Nozzle Assembly	30	12, 01, 01, D1	3634°F	Runs No. 10 and 11; Determine effect of O.D. Disp. by comparing Runs No. 10, 13, 14, & 15
12	Elastic	Grooved	Nozzle Insert	30	12, 01, 01, D2	3634°F	Determine effect of edge boundary condition by comparison with Run No. 10
13	Elastic	Grooved	Nozzle Insert	30	12, 02, 01, D1	3634°F	} Determine effect of O.D. boundary condition
14	Elastic	Grooved	Nozzle Insert	30	12, 02, 01, D1	3634°F	
15	Elastic	Grooved	Nozzle Insert	30	12, 04, 01, D1	3634°F	
16	Elastic	Grooved	Nozzle Insert	60	13, 01, 01, D1	3634°F	} Determine effect of O.D. boundary condition
17	Elastic	Grooved	Nozzle Insert	60	13, 02, 01, D1	3634°F	
18	Elastic	Grooved	Nozzle Insert	60	13, 03, 01, D1	3634°F	

TABLE 5-3

## ROCKET NOZZLE INSERT SURFACE BOUNDARY CONDITIONS

Surface	Boundary Condition Code	Description of Boundary condition
Inner Surface	I1	Pressure varies linearly from 57.5 atmos. at upstream edge to 26.7 atmos. at downstream edge. No material ablated
	I2	Same as I1 with 10 mils material recession
	I3	Same as I1 with 20 mils material recession
Outer Surface	O1	No radial displacement allowed. Unrestrained axial displacement allowed. No pressure.
	O2	5 mils radial displacement outward allowed before contact with rigid boundary. Unrestrained axial displacement allowed. No pressure.
	O3	16 mils radial displacement outward allowed before contact with rigid boundary. Unrestrained axial displacement allowed. No pressure.
	O4	.2 inch layer of grafoil between insert and silica phenolic. Grafoil assumed to be attached to insert. Grafoil not attached to silica phenolic, but outer surface of grafoil not allowed to displace radially outward. Unrestrained axial displacement allowed for outer surface of grafoil.
Upstream Surface	U1	Pressure of 57.5 atmos.
Downstream Surface	D1	Pressure of 57.6 atmos. required to maintain force equilibrium
	D2	Pressure of 26.7 atmos. in region from inner edge to outer edge of groove. No axial displacement allowed in region from outer edge of groove to outer edge of downstream surface.



MACHINED OFF AFTER  
COOLDOWN

NUMBER OF ELEMENTS: 240 THERMAL COOLDOWN  
240 MOTOR FIRING

FIGURE 5-1 STRUCTURAL GRID FOR NON-GROOVED  
NOZZLE INSERT.

A-4357

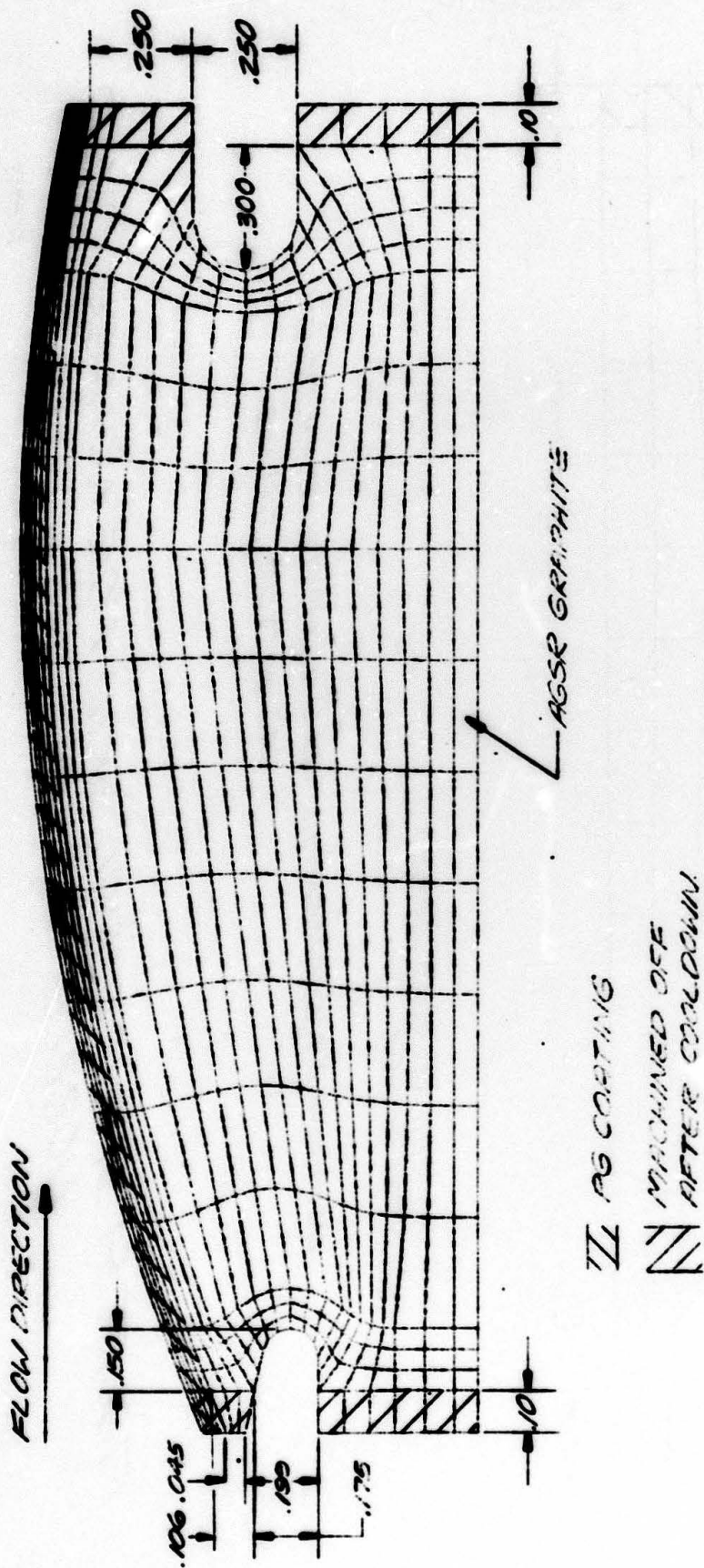


FIGURE 5-2 STRUCTURAL GRID FOR GROOVED  
NOZZLE INSERT.

A-9738



- 1) AGSR BILLET AT 70°F  
MACHINED FOR STRESS  
RELIEVING GROOVES AND  
INNER SURFACE CONTOURS



- 2) AGSR HEATED TO 3634°F
- 3) AGSR COATED WITH PG AT 3634°F
- 4) INSERT COOLED TO 70°F



- 5) INSERT WITH .1 INCHES  
MACHINED FROM EACH  
END AT 70°F

FIGURE 5-3 ROCKET NOZZLE INSERT FABRICATION PROCESS  
MODEL

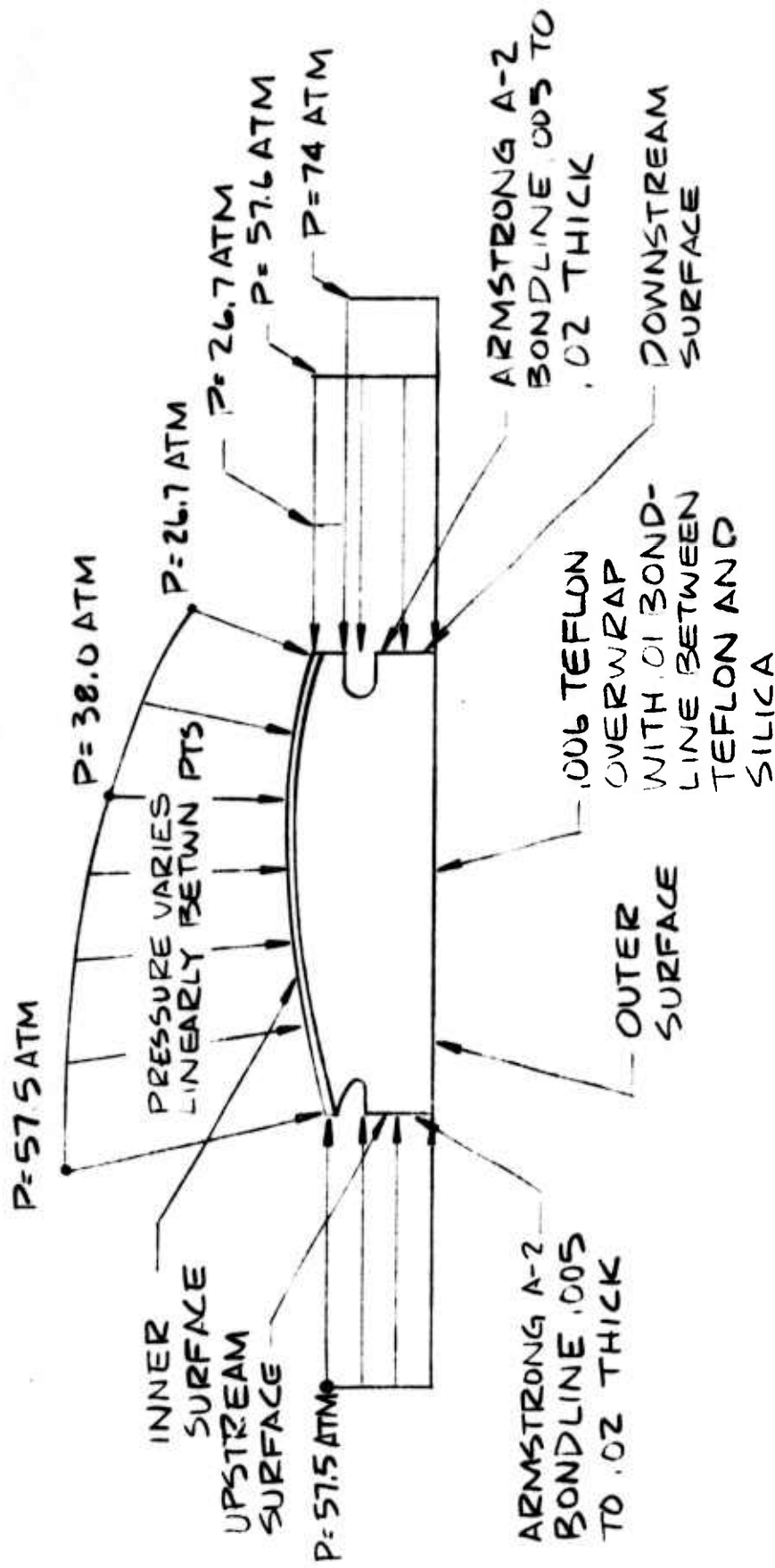


FIGURE 5-4 ROCKET NOZZLE INSERT BOUNDARY CONDITIONS FOR MOTOR FIRING

A-4693

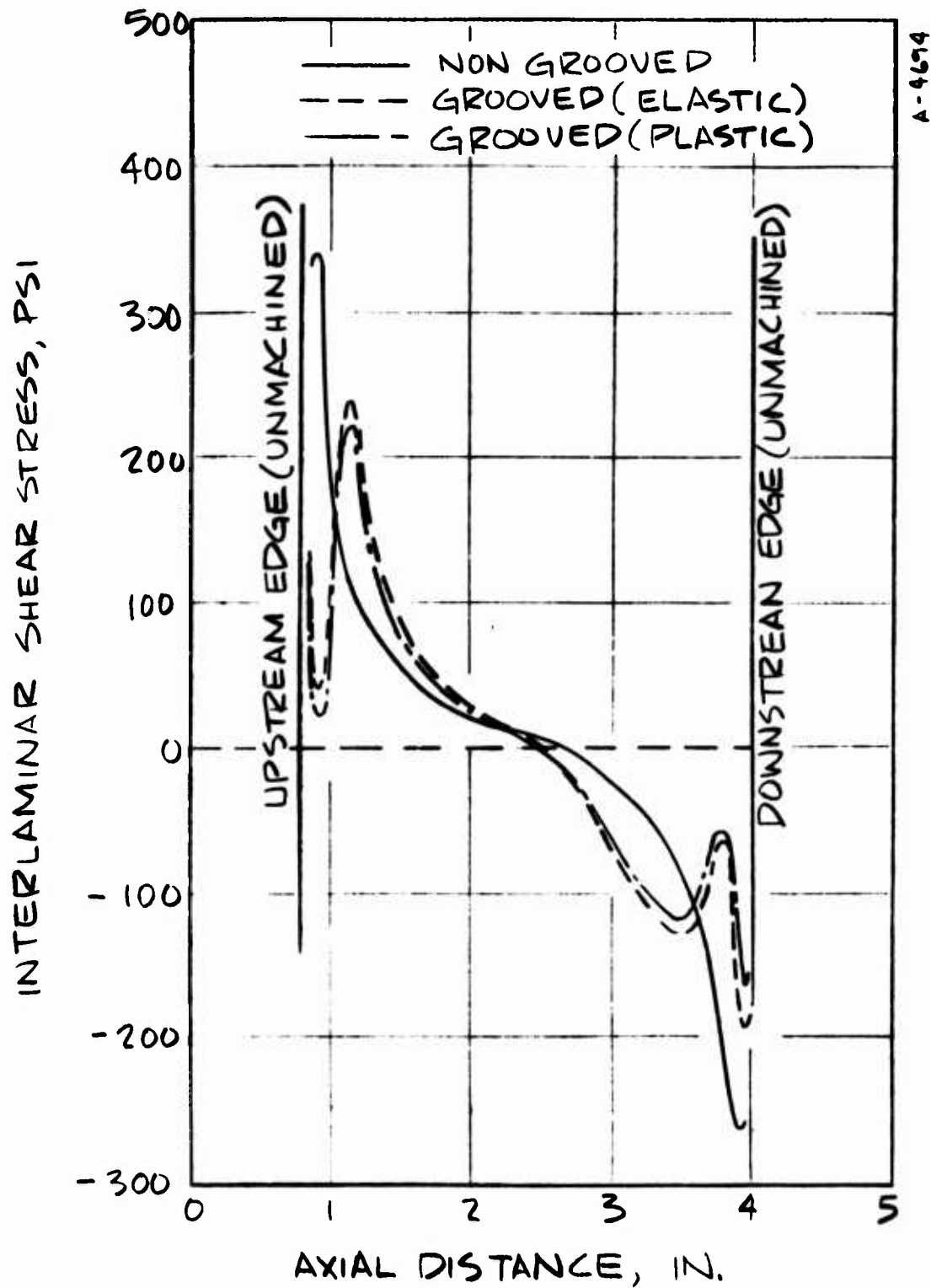


FIGURE 5-5 INTERLAMINAR SHEAR STRESS IN  
PYROLYTIC GRAPHITE COATING NEAR AGSR  
INTERFACE-COOLDOWN



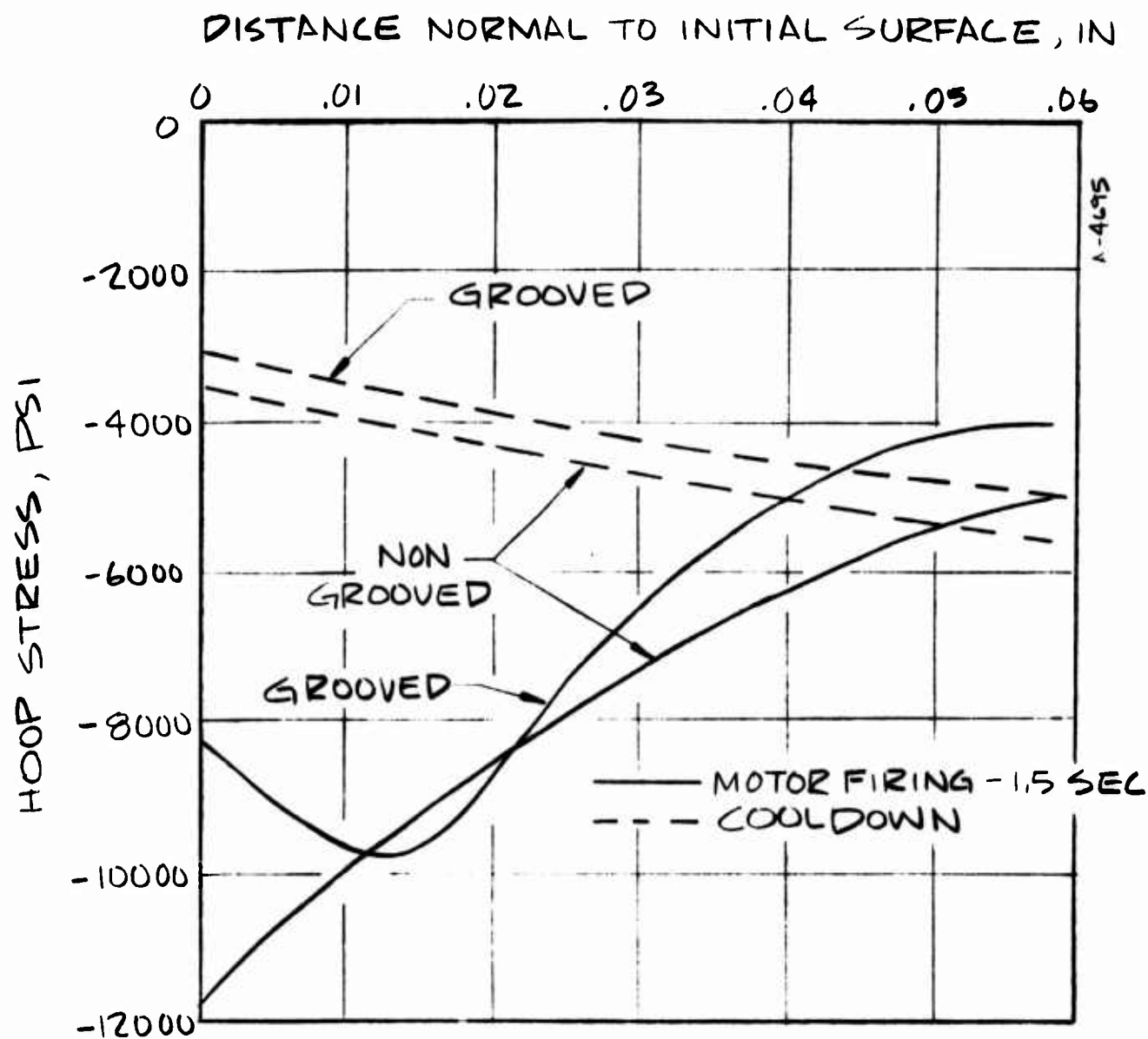


FIGURE 5-6 PYROLYTIC GRAPHITE HOOP STRESS AT NOZZLE ENTRANCE FOR GROOVED AND NON-GROOVED SUBSTRATES - O BACKSIDE DISPLACEMENT

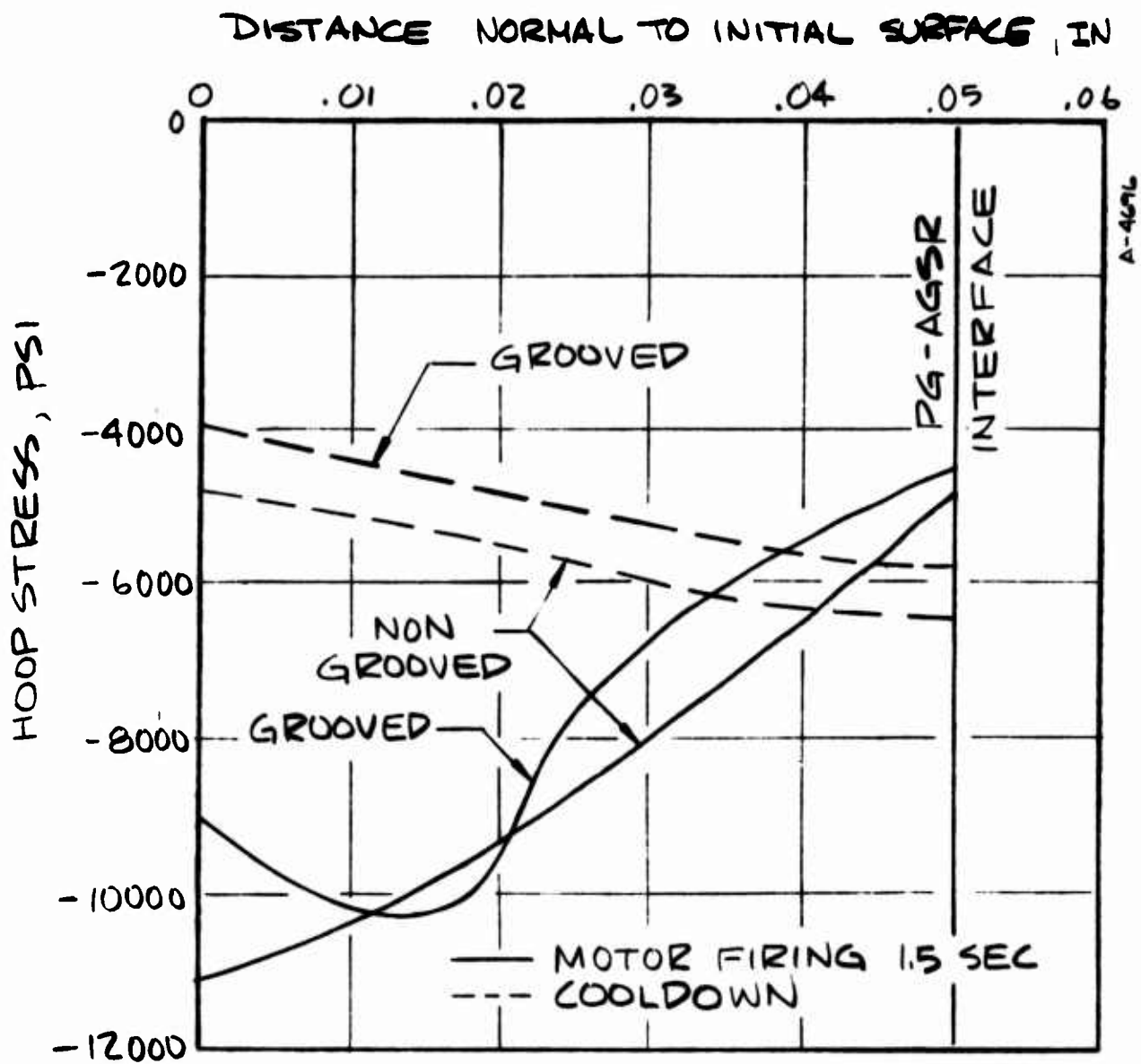


FIGURE 5-7 PYROLYTIC GRAPHITE HOOP STRESS AT NOZZLE EXIT FOR GROOVED AND NON-GROOVED SUBSTRATES - O BACKSIDE DISPLACEMENT

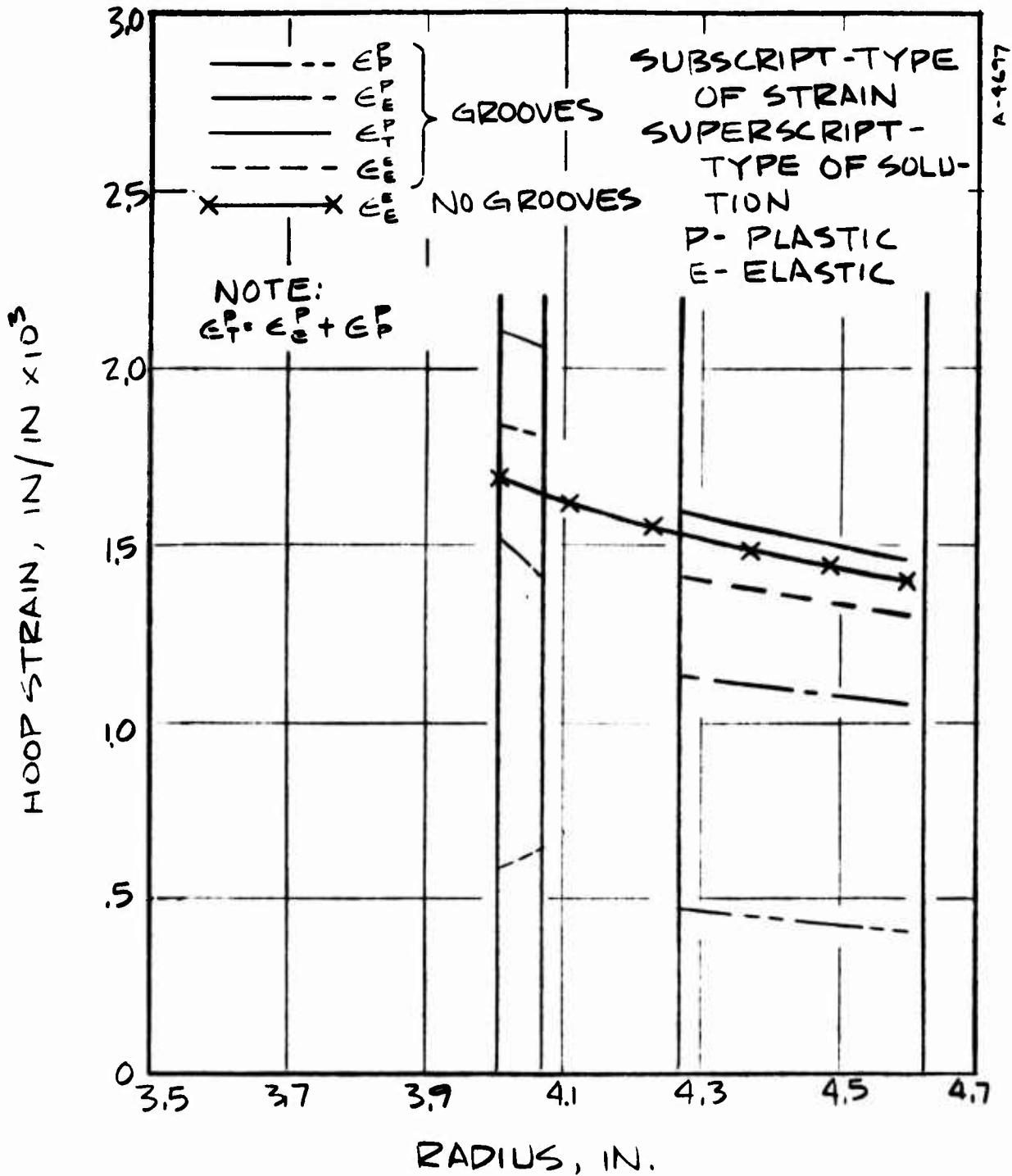


FIGURE 5-8 COMPARISON COOLDOWN HOOP STRAINS FOR THE GROOVED SUBSTRATE AT THE ENTRANCE PLANE BASED ON ELASTIC AND PLASTIC DOASIS ANALYSES

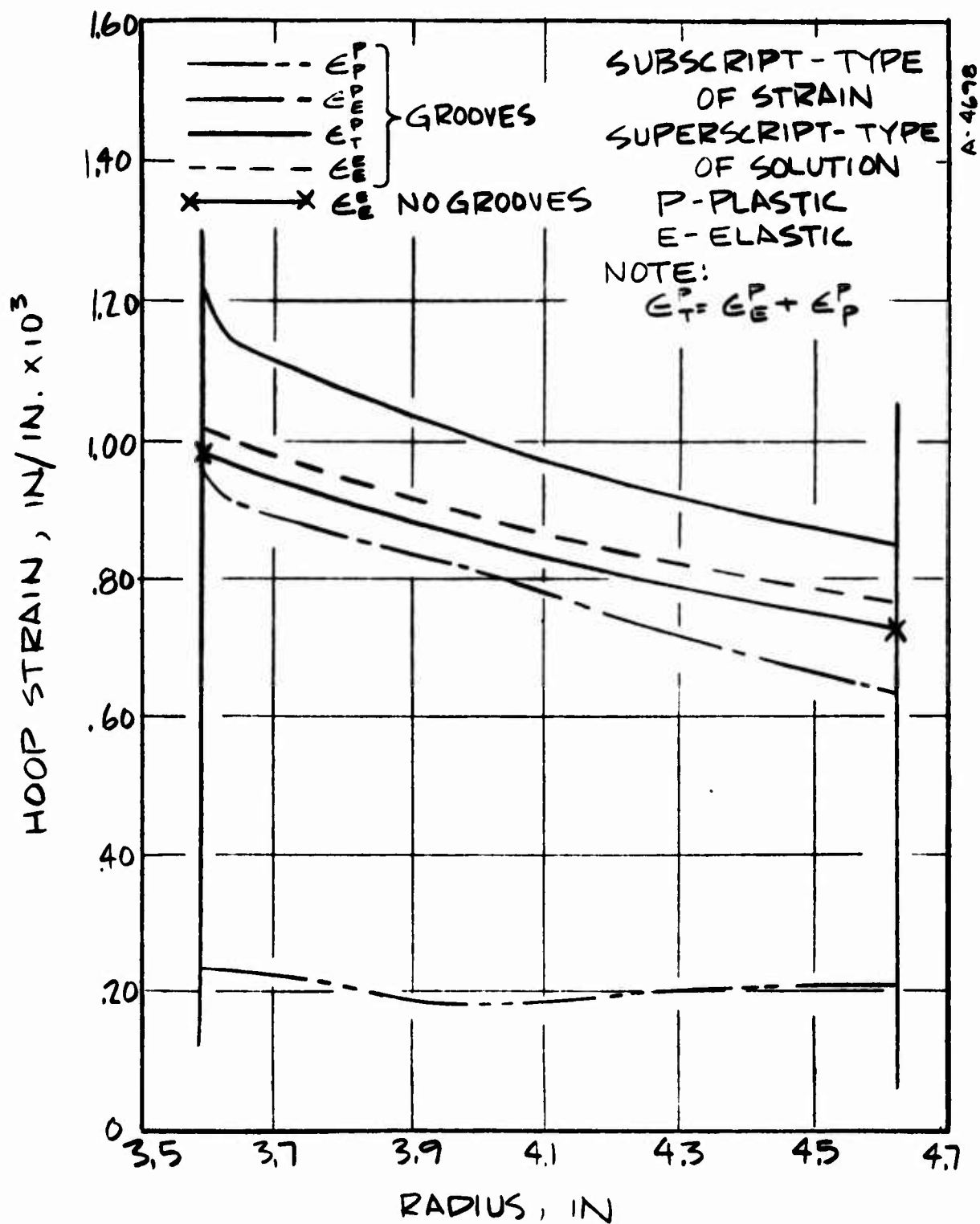


FIGURE 5-9 COMPARISON OF COOLDOWN HOOP STRAINS FOR THE GROOVED SUBSTRATE AT THE NOZZLE THROAT PLANE BASED ON ELASTIC AND PLASTIC DOWSIS ANALYSIS

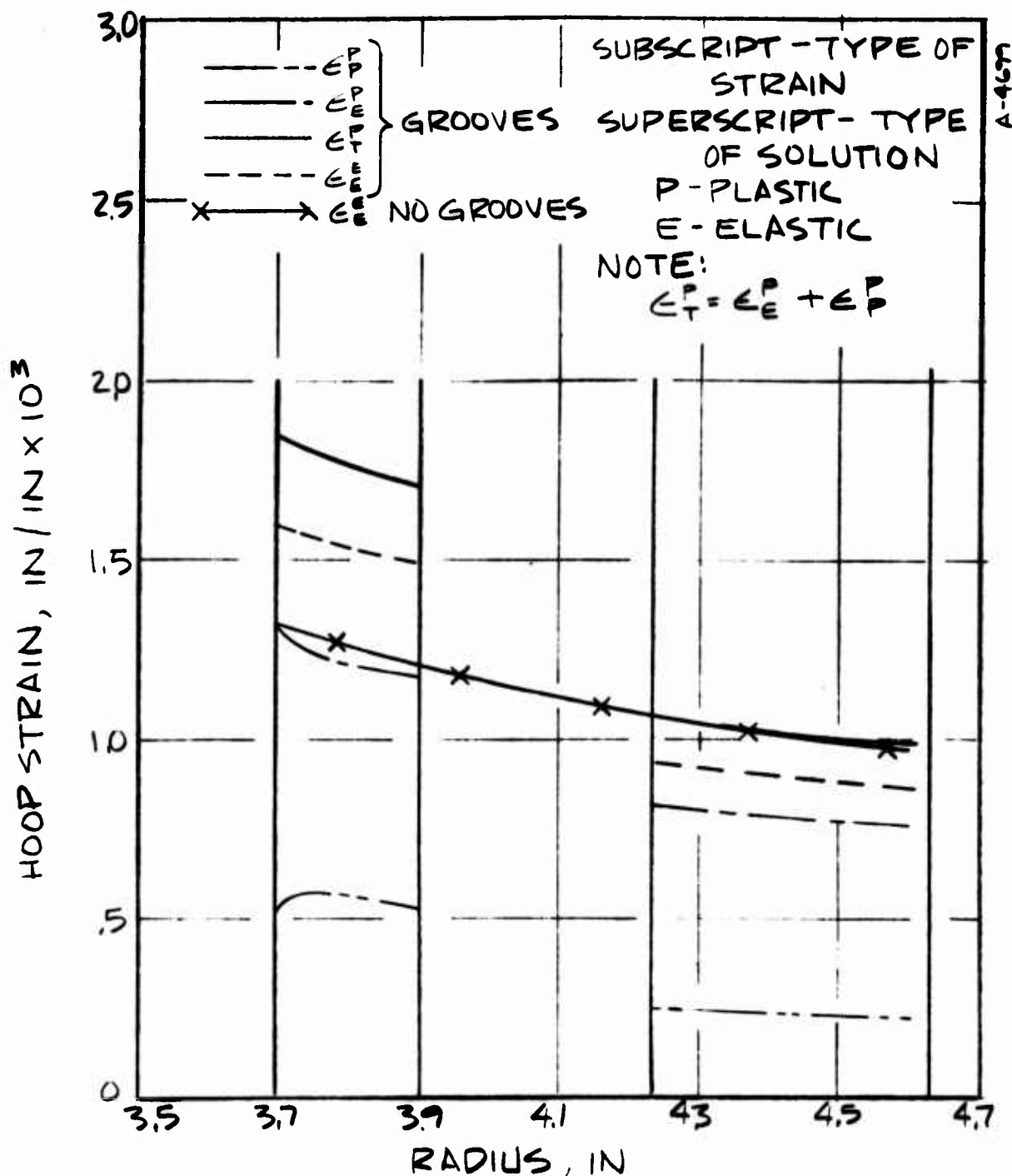


FIGURE 5-10 COMPARISON OF COOLDOWN HOOP STRAINS FOR THE GROOVED SUBSTRATE AT THE EXIT PLANE BASED ON ELASTIC AND PLASTIC DOASIS ANALYSIS

- REGION EXCEEDING FAILURE CRITERIA
- REGION NOT EXCEEDING FAILURE CRITERIA

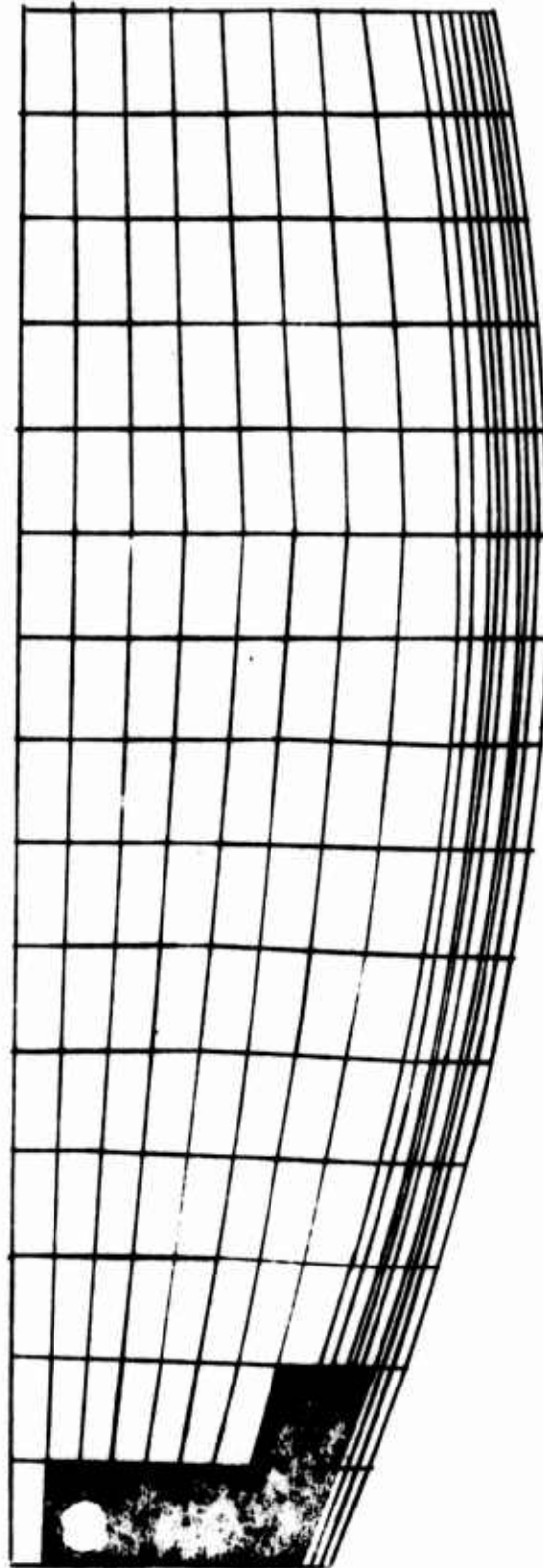


FIGURE 5-11 REGIONS OF FAILURES IN NON-GROOVED INSERT  
DUE TO COOLDOWN ELASTIC ANALYSIS

A-4685

- REGION EXCEEDING FAILURE CRITERIA
- REGION NOT EXCEEDING FAILURE CRITERIA

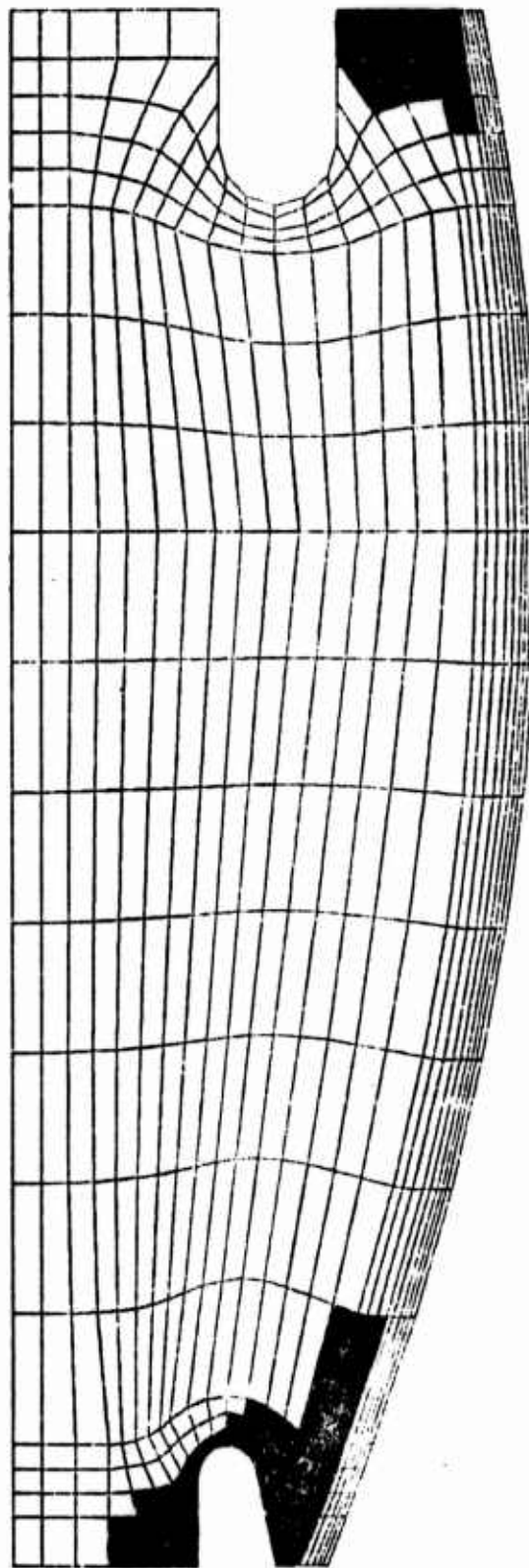


FIGURE 5-12 REGION OF FAILURES IN GROOVED INSERT DUE  
TO COOLDOWN ELASTIC ANALYSIS

10468

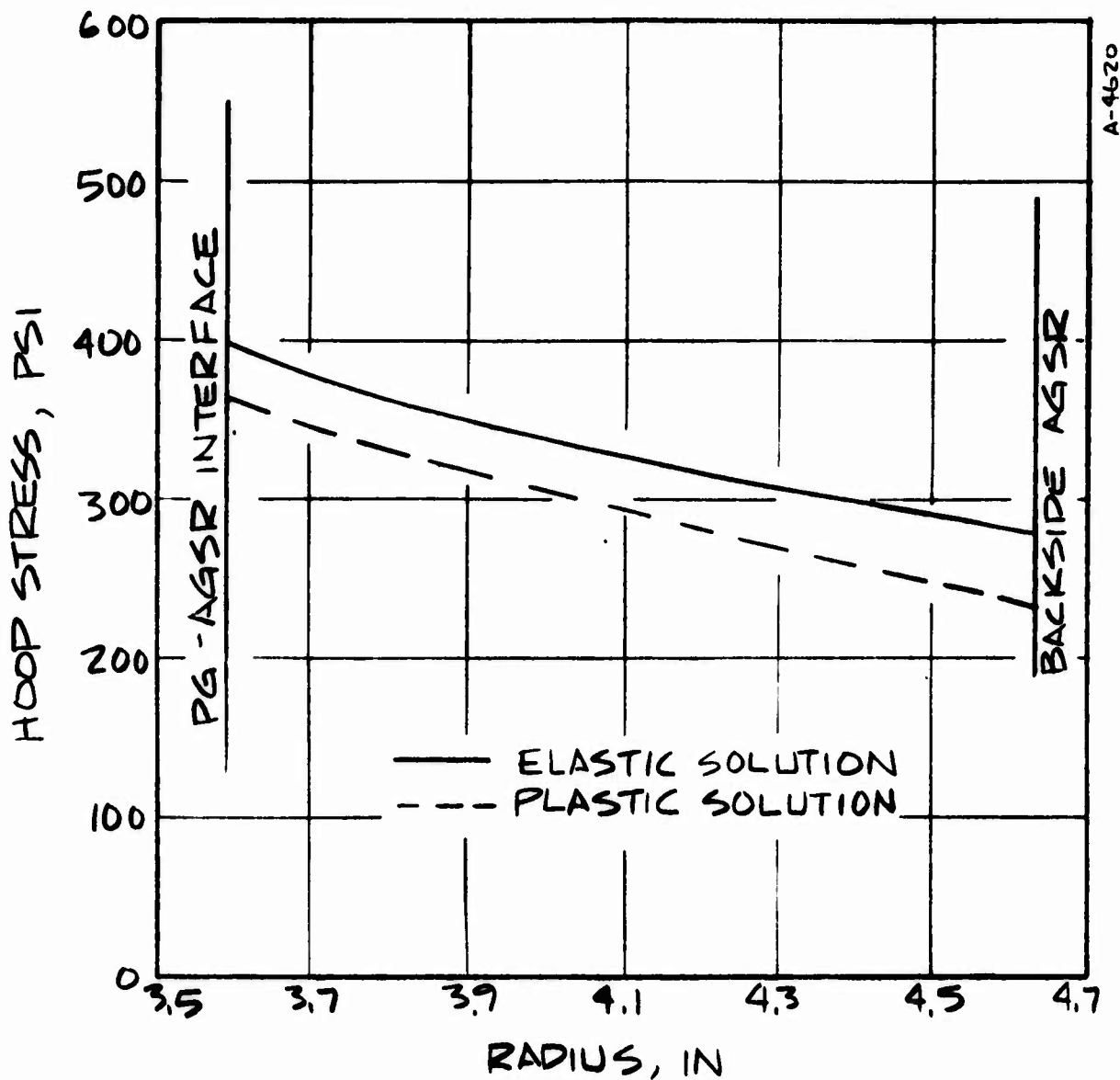


FIGURE 5-13 COMPARISON OF COOLDOWN HOOP STRESS FOR THE GROOVED SUBSTRATE AT THE NOZZLE THROAT PLANE BASED ON PLASTIC AND ELASTIC DOASIS ANALYSIS



■ REGION EXCEEDING FAILURE CRITERIA  
 □ REGION NOT EXCEEDING FAILURE CRITERIA

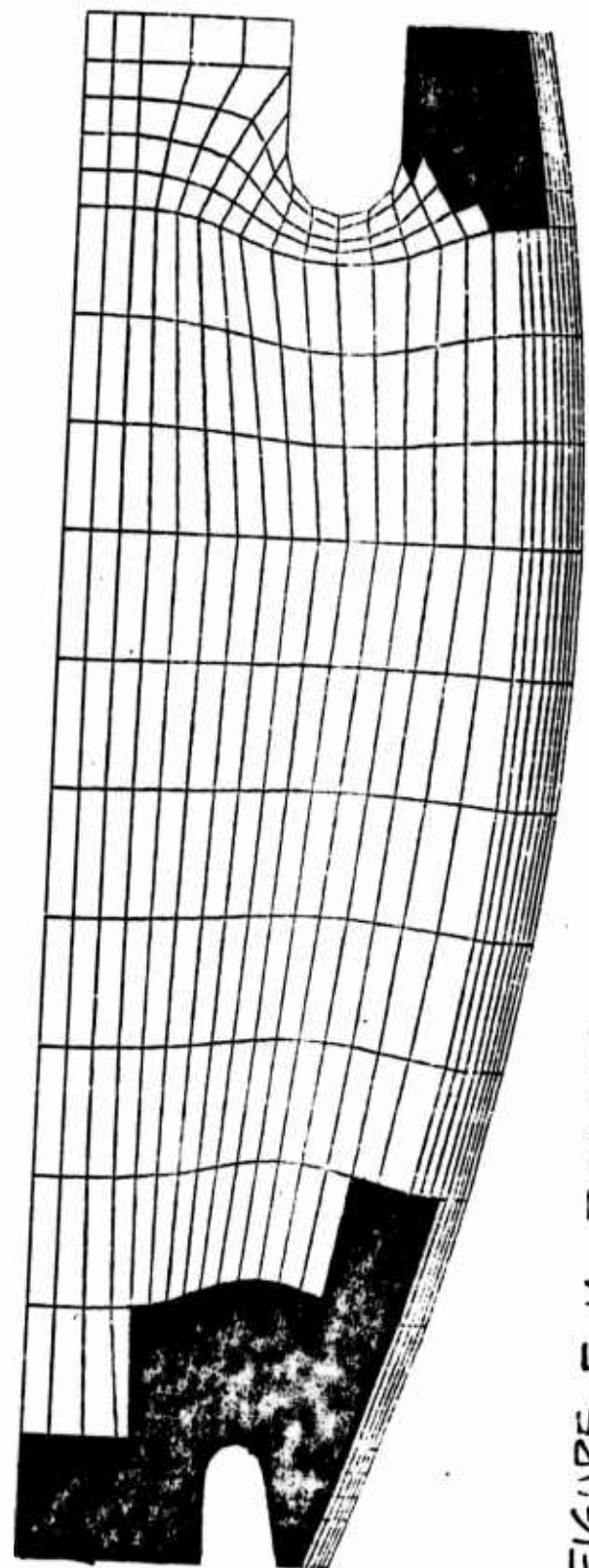
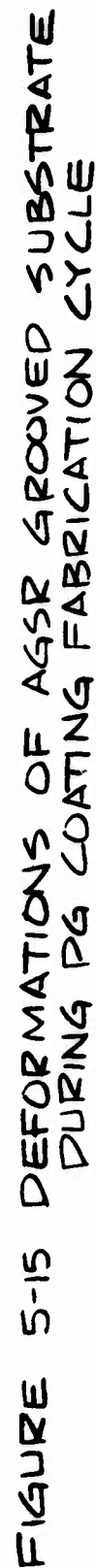


FIGURE 5-14 REGIONS OF FAILURES IN GROOVED INSERT DUE TO COOLDOWN PLASTIC ANALYSIS

A-968c



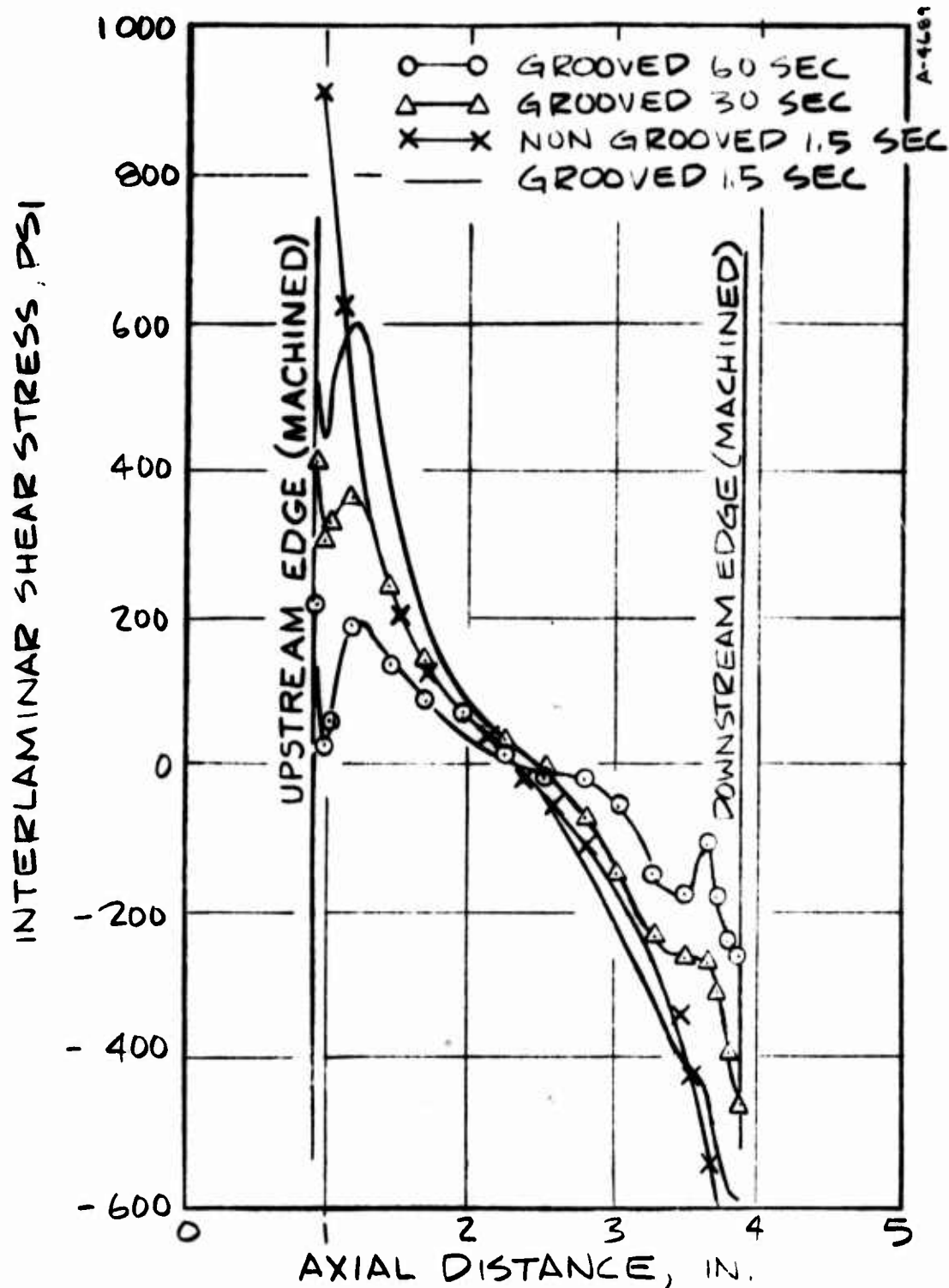


FIGURE 5-16 INTERLAMINAR SHEAR STRESS IN  
PYROLYTIC GRAPHITE COATING NEAR AGSR  
INTERFACE - MOTOR FIRING 0-DISPLACEMENT  
OUTER SURFACE

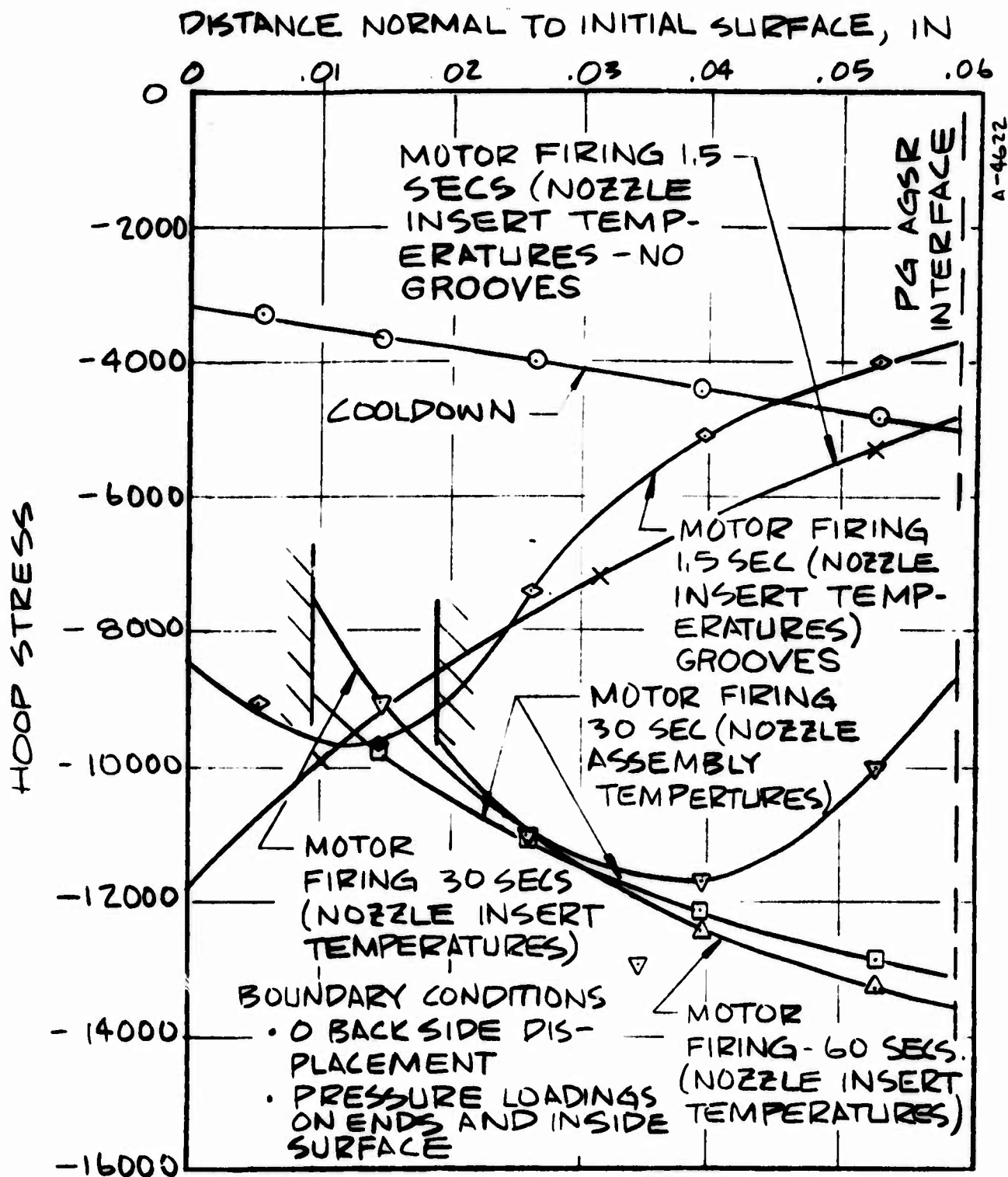


FIGURE 5-17 HOOP STRESS IN PYROLYTIC GRAPHITE COATING AT THE NOZZLE ENTRANCE GROOVED NOZZLE INSERT

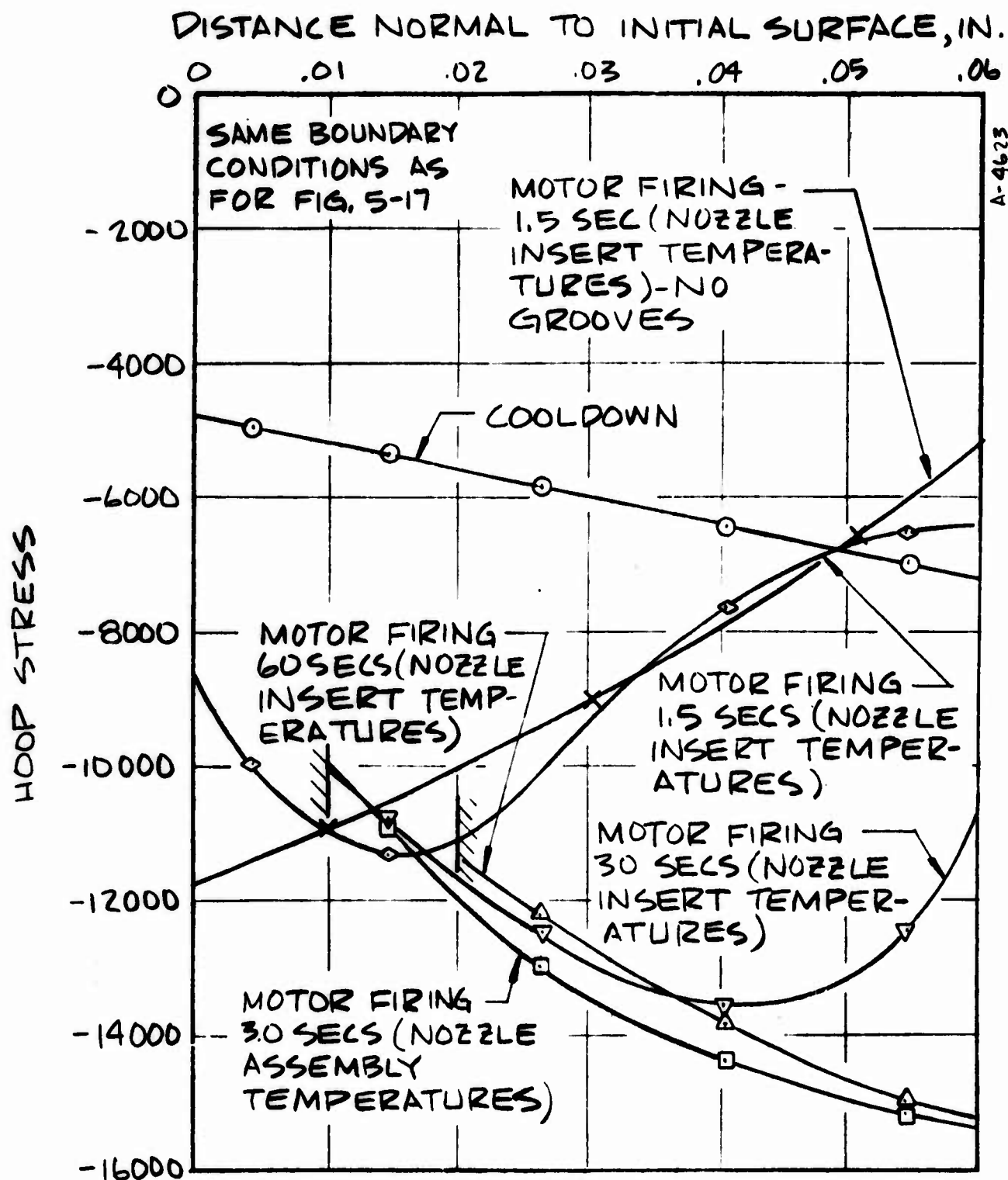


FIGURE 5-18 HOOP STRESS IN PYROLYTIC GRAPHITE COATING AT THE NOZZLE THROAT GROOVED NOZZLE THROAT

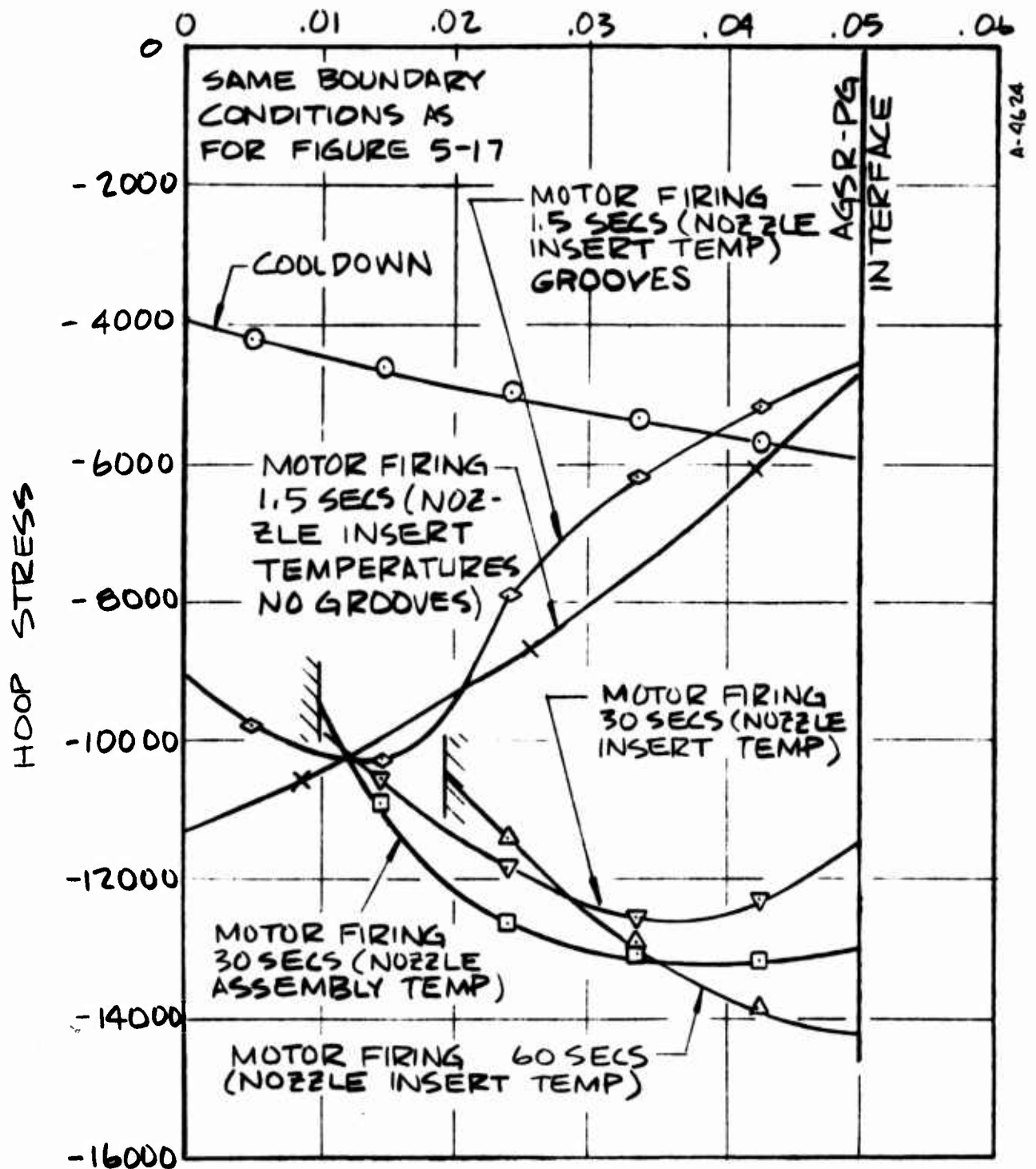


FIGURE 5-19 HOOP STRESS IN PYROLYTIC GRAPHITE COATING AT THE NOZZLE EXIT GROOVED NOZZLE INSERT



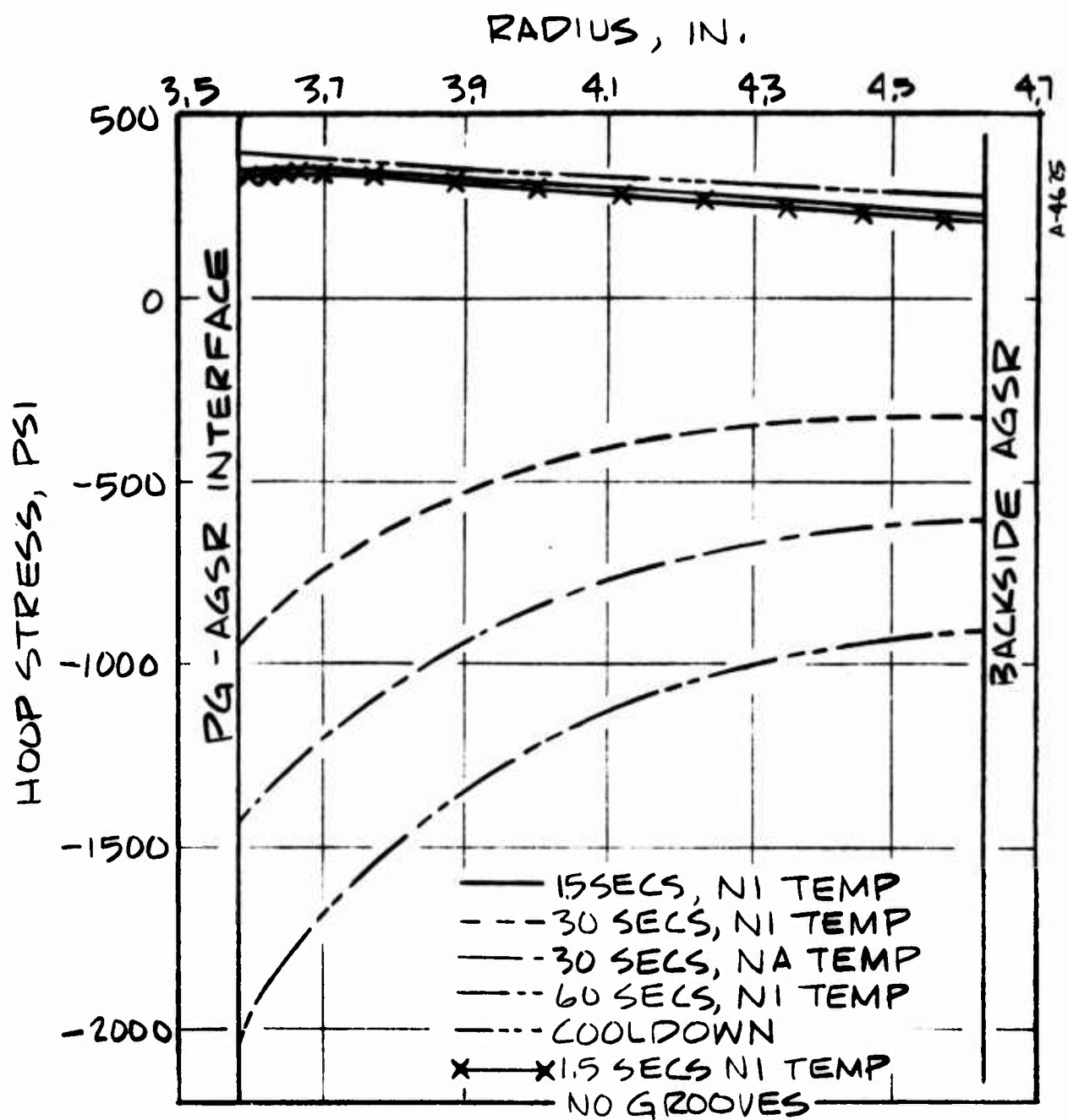


FIGURE 5-21 HOOP STRESS IN GROOVED SUB-  
STRATE AT THE NOZZLE THROAT PLANE-0  
BACKSIDE DISPLACEMENT FOR MOTOR  
FIRING STRESS



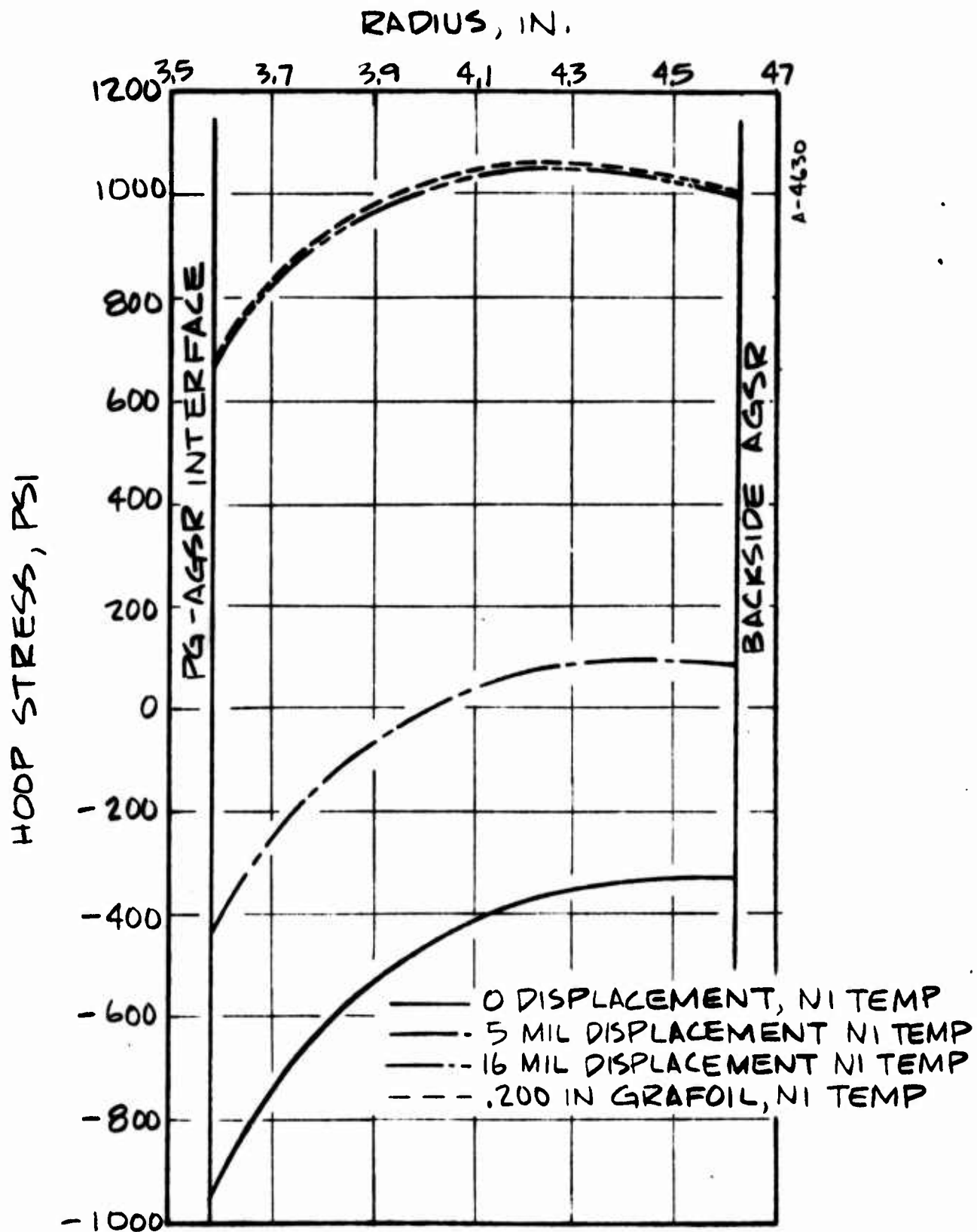


FIGURE 5-22 HOOP STRESS IN GROOVED SUBSTRATE  
AT THE NOZZLE THROAT PLANE FOR VARIOUS  
BACKSIDE GAPS,  $t = 30$  SECS

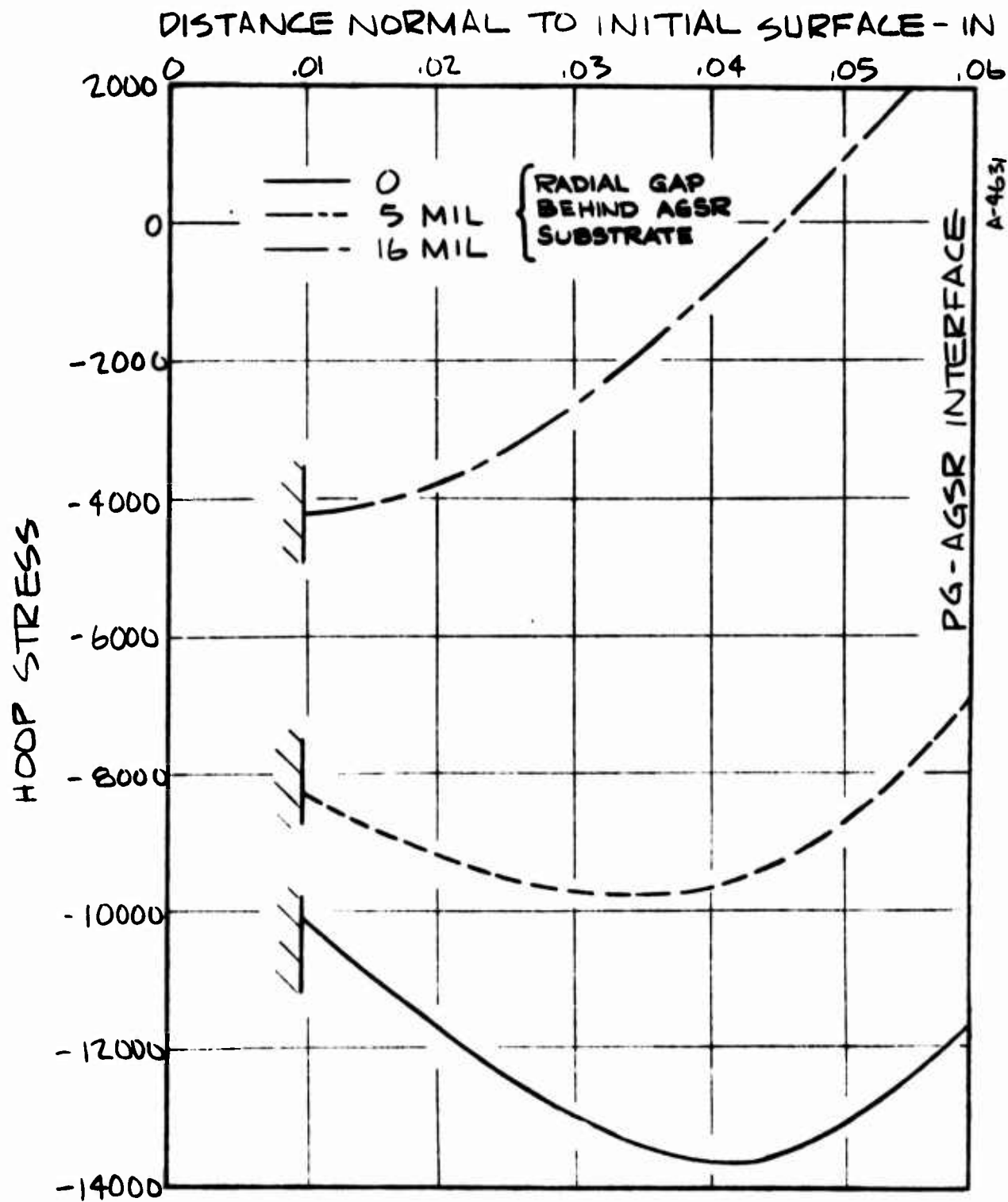


FIGURE 5-23 EFFECT OF GAP ON THE HOOP STRESS  
IN THE PYROLYTIC GRAPHITE COATING AT  
THE NOZZLE THROAT FOR THE GROOVED  
SUBSTRATE -  $t = 30$  SEC

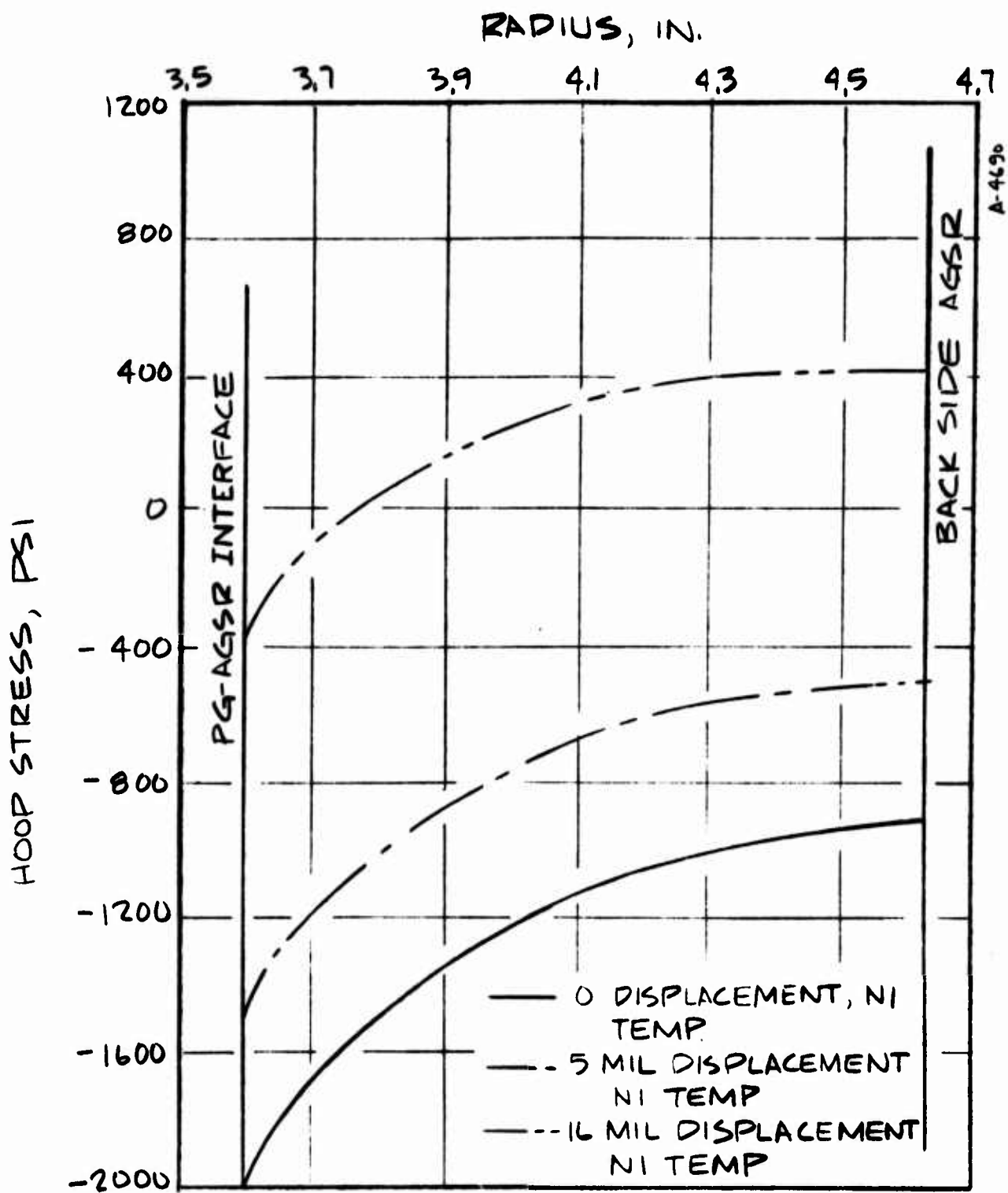


FIGURE 5-24 HOOP STRESS IN GROOVED SUB-  
STRATE AT THE NOZZLE THROAT PLANE FOR  
VARIOUS BACKSIDE CONSTRAINTS -60 SEC

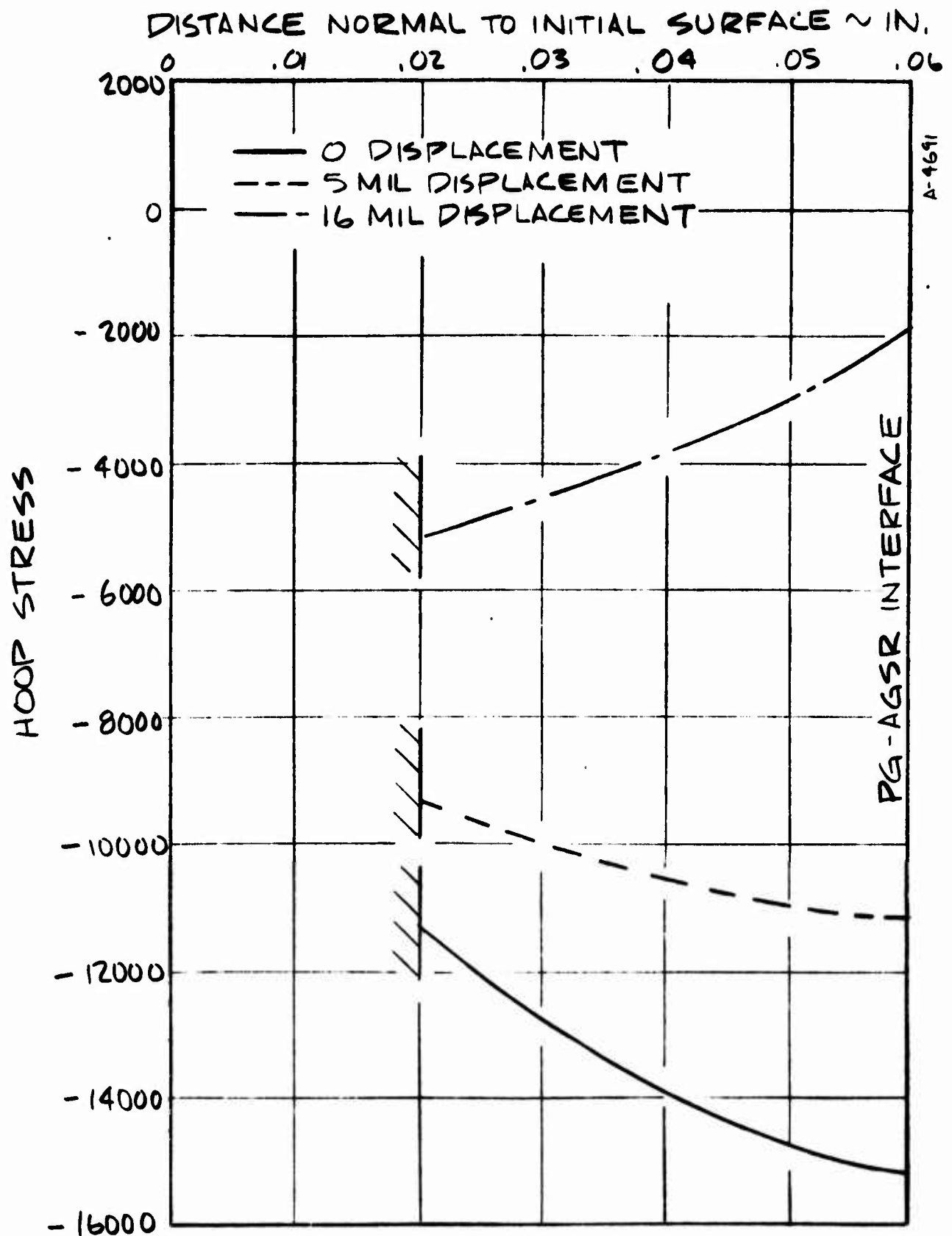


FIGURE 5-25 EFFECT OF GAP ON THE HOOP STRESS IN THE PYROLYTIC GRAPHITE COATING AT THE NOZZLE THROAT FOR THE GROOVED SUBSTRATE - T=60 SEC

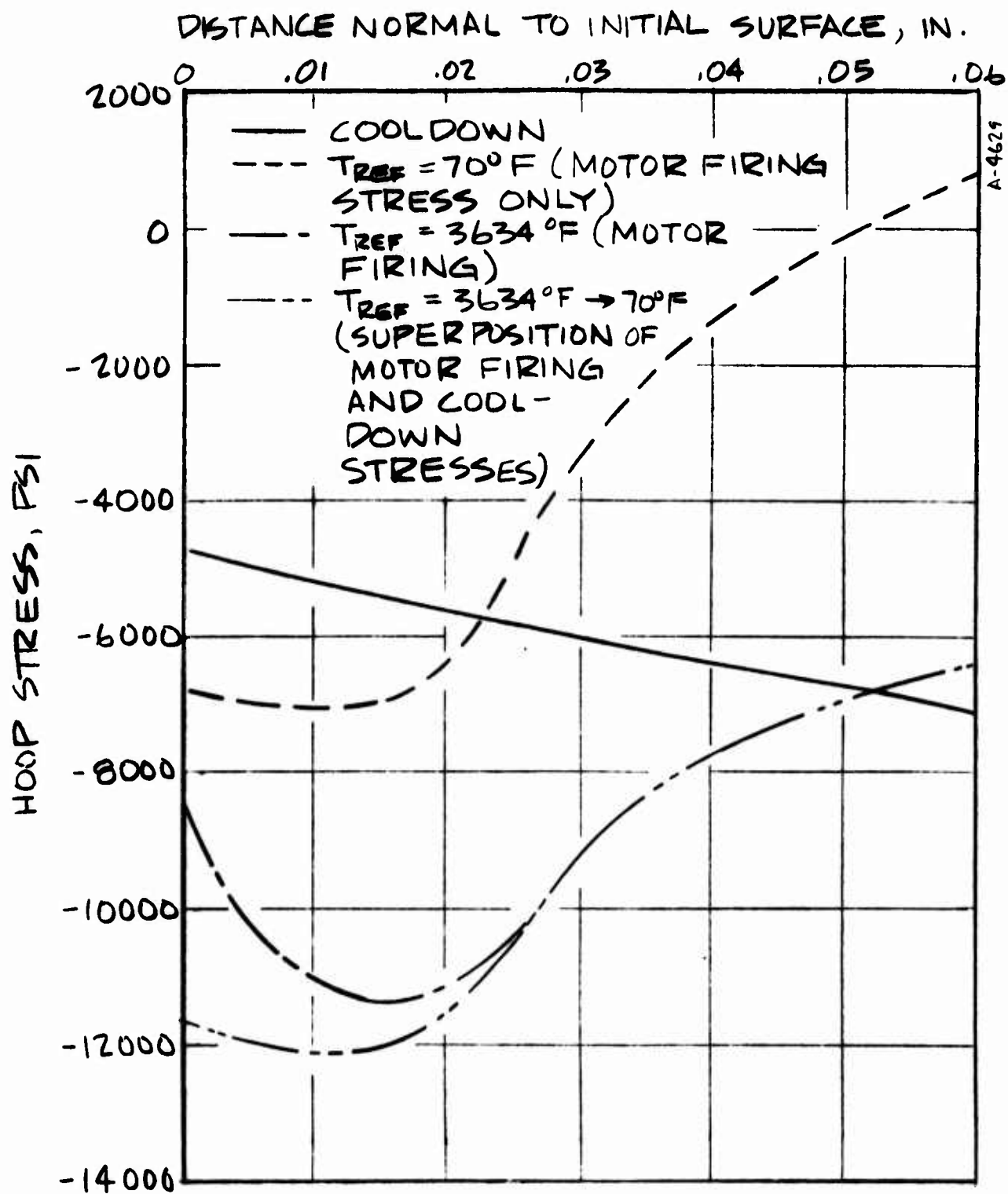


FIGURE 5-26 EVALUATION OF ERROR IN USING SUPERPOSITION PRINCIPLE TO CALCULATE TOTAL MOTOR FIRING STRESSES IN PYROLYTIC GRAPHITE COATING AT THE NOZZLE THROAT -  $t = 1.5$  SEC

## SECTION 6

### EVALUATION OF THERMOSTRUCTURAL RESULTS

The structural results presented in Section 5 show that the primary structural problems are:

- The interlaminar shear stress at the interface between the AGSR substrate and the PG coating during cooldown of the insert during fabrication
- The tensile hoop stress or strain in the AGSR during cooldown of the substrate during fabrication
- The compressive hoop stress or strain in the PG coating during the motor firing
- The definition of the constraint on the outside diameter of the AGSR substrate in order to minimize the hoop stress in the PG coating while at the same time keeping the stresses in the substrate to an acceptable level.

The primary problem in evaluating the structural results is that the structural analytical model used in the DOASIS computer code has not been validated for the PG coated nozzle insert due to the scarcity of meaningful experimental data for comparison. The "pass or fail" type of data which results from the motor firing indicates only whether or not the structural limitations of the insert have been exceeded. Since these data very seldom provide any information concerning the margin of safety of the insert if the test was successful or how severely the insert was overstressed if the test was a failure, the data only provide an end check on the validity of the structural analysis. In addition, since the structural analysis is based both on the material mechanical and thermal properties and on the structural analytical model, the source of analysis error can not be identified solely on the basis of "pass or fail" motor firing data. To identify the source of error, quantitative data at various stages during the fabrication process are required for comparison with analytical predictions. The only data of this type which is currently available for the insert analyzed in Figure 5-2 are outside diameter measurements of the AGSR substrate prior to and after the deposition of PG coating. The experimental net displacements were 40, 20, and 17 mils for the upstream, throat, and downstream insert locations. The trend of these measurements are in agreement with the predicted displacements presented

in Figure 5-15, but the predicted displacements are a factor of approximately four low. However, it should be noted that the high value of net displacement occurs at the upstream end of the insert which is also the region where extensive failure was predicted by the plastic analysis (refer Figure 5-14). A fact of equal significance is that if the measured displacements mentioned above are correct, then the maximum tensile hoop strain at the outside diameter of the substrate is approximately 11.5 mils. This value of strain is a factor of approximately 10 greater than the strain at fracture based on uniaxial measurements (refer Figure 3-12).

The above results become more difficult to interpret based on recent thermal expansion data which were obtained from Reference 27 and presented also in Figures 6-1 and 6-2. The data presented in Reference 27 was obtained by Southern Research Institute on PG samples fabricated by Atlantic Research Corporation and thus should be representative of the PG in the nozzle throat insert. The AGSR data are also based on material samples typical of that used in the nozzle insert. The data shown in Figure 6-1 compare the recent "a" direction PG and AGSR thermal expansion data with that presented previously in Figure 3-19. The recent "c" direction PG thermal expansion data are compared in Figure 6-2 with that presented previously in Figure 3-20. The data presented in Figures 6-1 and 6-2 show that the recent "c" direction PG thermal expansion data are in good agreement with previous data but that the recent "a" direction PG thermal expansion data are in very poor agreement with previous data. If indeed the data on ARC PG presented in Figure 6-1 are representative of the thermal expansion in the PG coated nozzle insert then

- The mismatch of the PG coating and the AGSR substrate thermal expansions is minimal below the deposition temperature of 3654°F and, thus the cooldown stresses should be minimal
- The compressive stresses in the PG coating during the motor firing would be much larger than those presented in Section 5.

The discussion presented in the previous paragraphs does not shed much light on interpreting the results presented in Section 5. However, if the assumption was made that the property data used in the analysis were correct, then the following conclusions can be made

- The predicted cooldown hoop strains in the AGSR indicate structural failure of the substrate.
- The PG coating would be structurally adequate if a 16 mil expansion of the substrate was allowed during the motor firing. However, the predicted hoop stresses in the PG coating indicate structural failure if the allowable expansion is on the order of 5 mils.

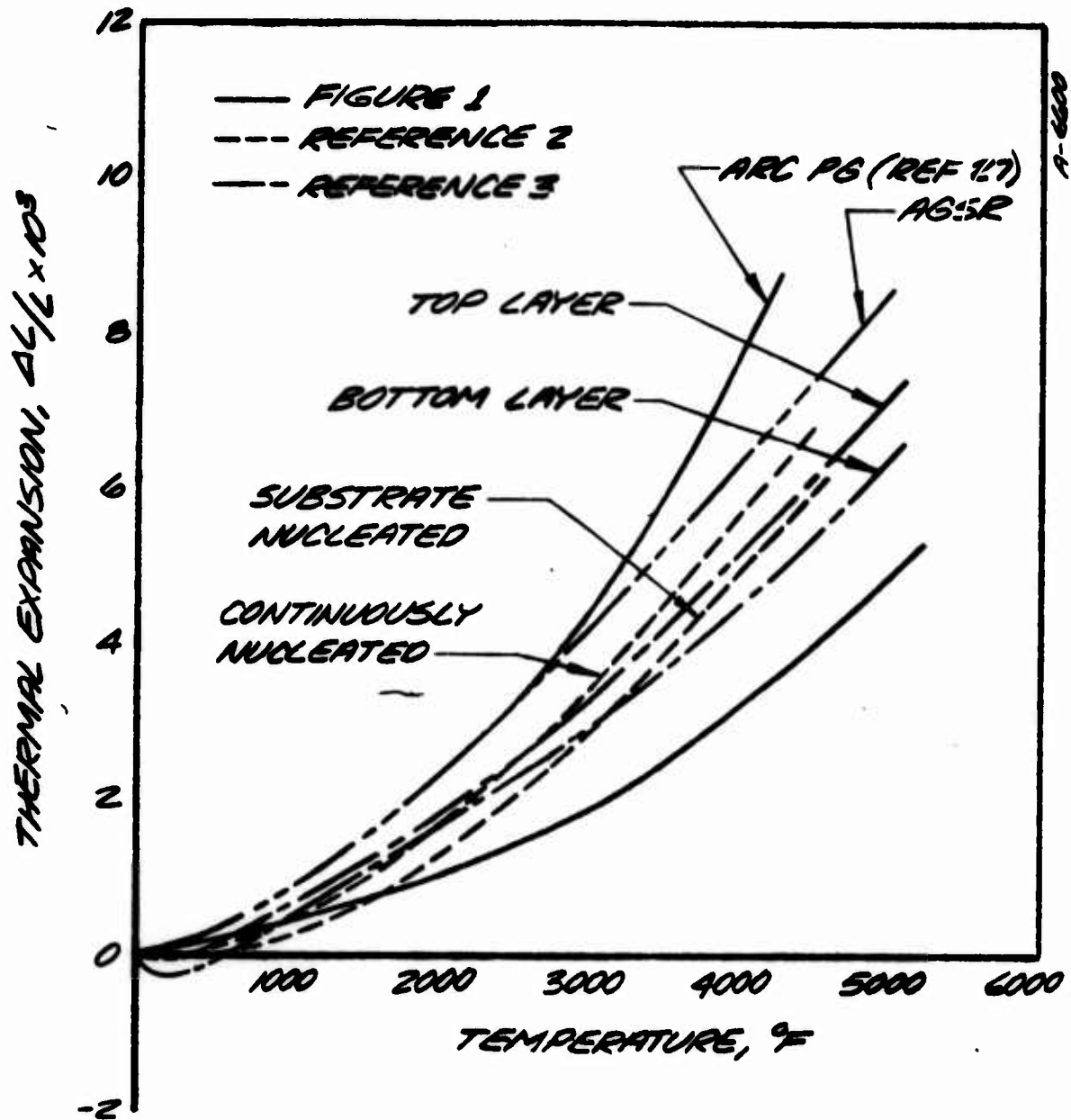


FIGURE 6-1 COMPARISON OF "a" DIRECTION PYROLYTIC GRAPHITE THERMAL EXPANSION.



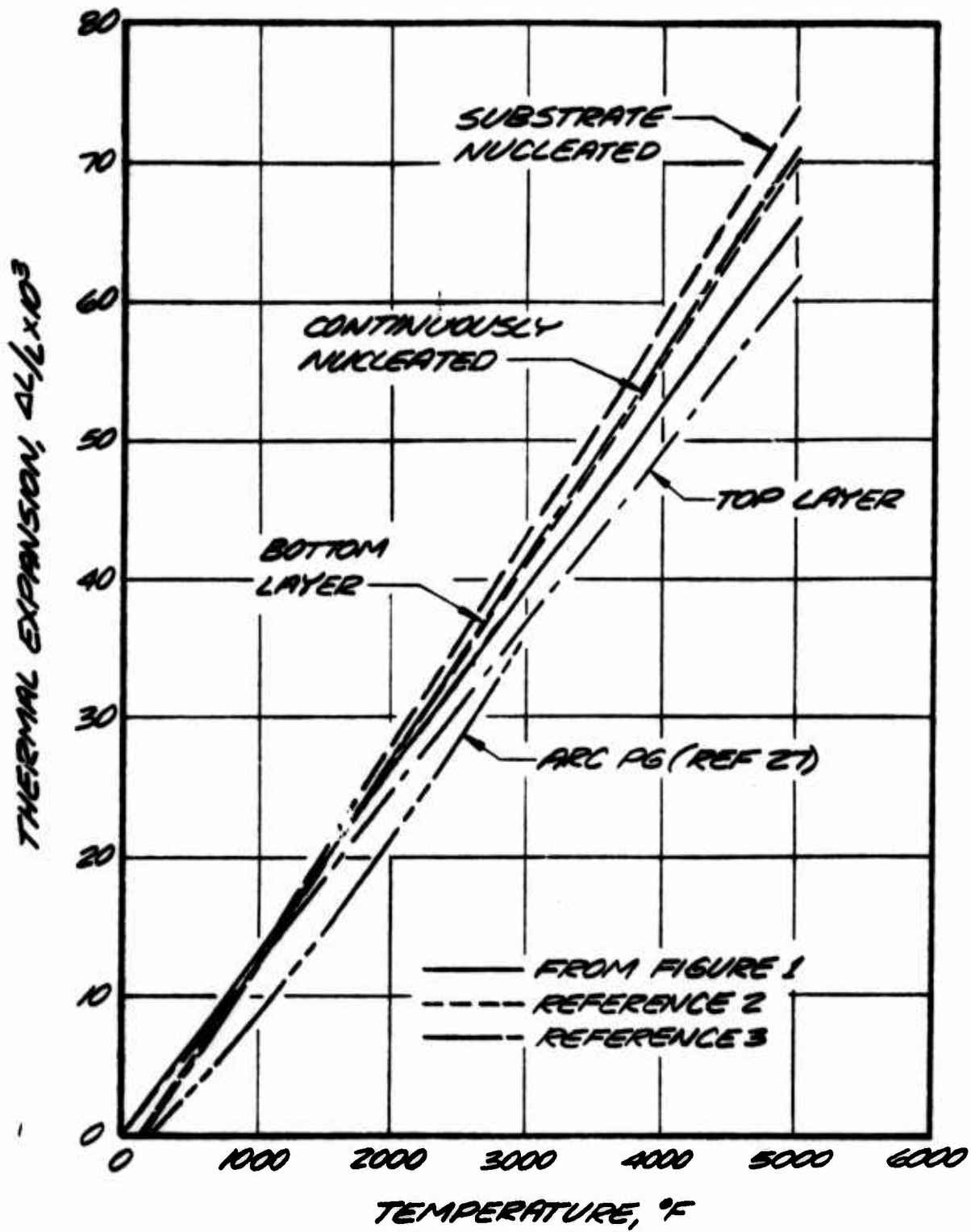


FIGURE 6-2 COMPARISON OF "C" DIRECTION PYROLYTIC GRAPHITE THERMAL EXPANSION.

## REFERENCES

1. Hove, J. E. and Riley, W. C., "Ceramics for Advanced Technologies," Wiley, New York, 1956.
2. Batchelor, J. D., "Improvement of Pyrolytic Graphite Coated Nozzles for Solid Propellant Rocket Motors," AFRPL-TR-67-245, First Interim Technical Report, Contract F04611-67-C-0047, September 5, 1967.
3. Performance Data of AIRCO Speer Carbon Products, Aerospace Grades. Speer Carbon Products, St. Marys, Pennsylvania.
4. Wool, M. R., Baker, D. L., Murphy, A. J., "Material Performance of Carbon Phenolic Ablators and Pyrolytic Graphite Coatings in Nozzles Subjected to Multiple Pulse Duty Cycles," AFRPL-TR-71-130 (Aerotherm Final Report 71-43) October 1971.
5. Baker, D. L., Wool, M. R., Schaefer, J. W., "Development of Total and Radiative Heat Flux Measurement Systems for Rocket Nozzle Applications," AFRPL-TR-70-82 (Aerotherm Final Report 70-11), August 1970.
6. "Pyrolytic Graphite," Engineering Handbook, Super Temp Corporation, Santa Fe Springs, California, 1964.
7. "Pyrolytic Graphite Final Report," LMSC-901-376, Lockheed Missiles and Space Company, June 1962.
8. Campbell, J. G., Haas, M. T., and Coulbert, C. D., "Pyrolytic Graphite Thrust Chambers for Space Orientation and Altitude Control, Phase I; Analysis and Preliminary Design," AFRPL-TR-66-95 (Marquardt Corporation) June 1966.
9. Smith, W. H. and Leeds, D. H., "Pyrolytic Graphite," Modern Materials, Vol. 7, Copyright 1970, Academic Press, Inc.
10. Donadio, R. M. and Pappis, J., "The Mechanical Properties of Pyrolytic Graphite," Report T-574, Raytheon Company, Waltham, Massachusetts.
11. Pears, C.D. and Starrett, H.S., "Polygraphites Subjected to Temperature Stress Loadings," AFML-TR-73-59, March 1973.
12. Union Carbide: The Industrial Engineering Handbook.
13. Feasibility Demonstration of Pyrolytic Graphite Coated Nozzles," AFRPL-TR-65-57 (Atlantic Research Corporation), March 1965.
14. Weiler, F. C. and Rodriguez, D.A., "Advanced Methods of Anisotropic, Elastic-Plastic-Thermal Stress Analysis for Bodies of Revolution," AFML-TR-70-133, Part I, edited by D. M. Forney, Jr., August 1970.
15. User's Manual: Deformation Orthotropic Axisymmetric Solution of Inelastic Solids (DOASIS) Computer Program.
16. Weiler, F. C., "Anisotropic, Elastic-Plastic-Thermal Stress Analysis of Solid Structures," Volume 2-Part D, Proceedings of the First International Conference on Structural Mechanics in Reactor Technology, Berlin, Germany, 20-24 September 1972.

17. Gebhardt, J. J. and Barry, J. M., "Mechanical Properties of Pyrolytic Graphite," AIAA Journal, Vol. 3, No. 2, p. 302.
18. Bradshaw, W. and Armstrong, J. R., "Pyrolytic Graphite, Its High Temperature Properties," ASD-TDR-63-195 (AD 403728), March 1963.
19. Letter from Townsend, H. N. (Union Carbide) to Payne, W. (AFRPL): Stress-Strain Data on Grade AGSR Graphite. February 4, 1972.
20. Schaefer, J. W., Dahm, T. J., Rodriguez, D. A., Reese, Jr., J. J., and Wool, M. R., "Studies of Ablative Material Performance for Solid Rocket Applications," NASA CR-72429 (Aerotherm Reort No. 68-30), March 1968.
21. User's Manual, "Aerotherm Axi-symmetric Transient Heating and Material Ablation Computer Program (ASTHMA3), Volume I - Program Description and Sample Problems," AFRPL-TR-72-24 (Aerotherm Report No. UM-72-26) January 1972.
22. User's Manual, "Aerotherm Real Gas Energy Integral Boundary Layer Program (ARGEIBL)," Aerotherm Report 69-UM-6911, November 1969.
23. Powars, C. A., and Kendall, R. M., "User's Manual - Aerotherm Chemical Equilibrium (ACE) Computer Program," May 1969.
24. User's Manual, "Aerotherm Graphite Surface Kinetics Computer Program, Volume I - Program Description and Sample Problems," AFRPL-TR-72-23 (Aerotherm Report No. UM-72-25), January 1972.
25. Baker, D. L., Schaefer, J. W., and Wool, M. R., "Thermal Property and Ablative Response Characterization of Pyrolyzed Materials," Aerotherm Report 69-47, January 1969.
26. Weiber, F. C., "Anisotropic, Elastic-Plastic-Thermal Stress Analyses of the First International Conference on Structural Mechanics in Reactor Technology, Berlin, Germany, 20-24, September 1972.
27. Data Transmittal from E. Olcott (Atlantic Research Corporation) to D. Baker (Aerotherm).